The multiple ways of recycling Archaean crust: A case study from the ca. 3.1 Ga granitoids from the Barberton Greenstone Belt, South Africa

J.F. Moyen, A. Zeh, M. Cuney, A. Dziggel, S. Carrouée

▶ **To cite this version:**

J.F. Moyen, A. Zeh, M. Cuney, A. Dziggel, S. Carrouée. The multiple ways of recycling Archaean crust: A case study from the ca. 3.1 Ga granitoids from the Barberton Greenstone Belt, South Africa. Precambrian Research, 2021, 353, pp.105998. 10.1016/j.precamres.2020.105998 . hal-03493289

HAL Id: hal-03493289
https://hal.science/hal-03493289

Submitted on 2 Jan 2023

HAL is a multi-disciplinary open access archive for the deposit and dissemination of scientific research documents, whether they are published or not. The documents may come from teaching and research institutions in France or abroad, or from public or private research centers.

L'archive ouverte pluridisciplinaire **HAL**, est destinée au dépôt et à la diffusion de documents scientifiques de niveau recherche, publiés ou non, émanant des établissements d'enseignement et de recherche français ou étrangers, des laboratoires publics ou privés.

Distributed under a Creative Commons Attribution - NonCommercial 4.0 International License

Version of Record: https://www.sciencedirect.com/science/article/pii/S0301926820305878
Manuscript_51b6b358b3bba078ee12f63d68edf027

The multiple ways of recycling Archaean crust: a case study from the ca. 3.1 Ga granitoids from the Barberton Greenstone Belt, South Africa

Moyen, J.-F.[1,2,*]

Zeh, A.[3,4]

Cuney, M.[5]

Dziggel, A.[6]

Carrouée, S.[1]

[1] Université de Lyon, Laboratoire Magmas et Volcans, UJM-UCA-CNRS-IRD, 23 rue Dr. Paul Michelon, 42023 Saint Etienne.

[2] on sabbatical at School of Earth, Environment and Atmosphere Sciences, Monash University, Clayton, VIC 3168, Australia.

[3] Institute for Applied Geosciences - Karlsruhe Institute of Technology (KIT), Campus South, Mineralogy and Petrology, Adenauerring 20b, 50.40, D-76131 Karlsruhe, Germany.

[4] Frankfurt Isotope and Element Research Center (FIERCE), Altenhöferallee 1, D-60438 Frankfurt, Germany.

[5] Université de Lorraine, CNRS, CREGU, GeoRessources, F-54000 Nancy, France.

[6] Institute of Geology, Mineralogy und Geophysics, Ruhr-Universität Bochum Universitätsstraße 150 44801 Bochum, Germany

[*] Corresponding author. jean.francois.moyen@univ-st-etienne.fr

© 2020 published by Elsevier. This manuscript is made available under the CC BY NC user license
https://creativecommons.org/licenses/by-nc/4.0/

1. Introduction

Archaean cratons are stable continental blocks that escaped reworking after their formation (Windley, 1995). They include an Archaean continental crust, underlain by a refractory, rigid lithospheric mantle (Pearson and Wittig, 2014), and they are covered by intracratonic sedimentary successions and possibly cut by dyke swarms (Cawood et al., 2018). The Archaean crust fossilizes early geological evolution, but has typically not been affected by subsequent events: there is a striking contrast between the geological characteristics of the pre-cratonic (Archaean) period and cratonic evolution. Whereas the Archaean regime features soft deformation of a hot crust, a granite-greenstone association, pervasive melting and magmatism, the cratonic stage in contrast records little pervasive deformation or metamorphism. A key issue in Archaean geology is therefore the transition from the Archaean, permobile and hot stage, to the post-Archaean, cold and rigid stage (Capitanio et al., 2019; Chowdhury et al., 2020; Nebel et al., 2018).

In most cratons (Cawood et al., 2018; Laurent et al., 2014a), this transition also corresponds to a change in character of the granitic magmatism, with evolution from pre- to syn-tectonic sodic granitoids of the TTG (tonalite—trondhjemite—granodiorite; Hoffmann et al., 2018; Martin, 1986; Moyen and Martin, 2012) series to a much more diverse assemblage of syn- to post-tectonic, generally potassic granites (Laurent et al., 2014a) formed by a number of processes including differentiation of mantle-derived melts (the “sanukitoid series”) and melting of the crust.

The Kaapvaal Craton of Southern Africa, and in particular the Barberton Granite-Greenstone Terrain in its south-eastern part, offers an excellent example of craton stabilization processes and related changes. Until ca. 3.2 Ga, the geological processes are distinctly “Archaean” in character, with the formation of greenstone belts (Lowe and Byerly, 2007), TTG magmatism (Moyen et al., 2018) and complex – and controversial— deformation and metamorphic patterns (Cutts et al., 2014; Lana et al., 2010; Mühlberg et al., in revision; Schoene and Bowring, 2010; Van Kranendonk et al., 2014; Wang et al., 2019). At ca. 3.07 Ga however, the Dominion Group was deposited over a stable continental basement (Marsh, 2006), forming essentially undeformed sequences unconformably overlying the meso-Archaean basement. The cratonization event in the South-Eastern Kaapvaal craton occurs at ca. 3.1 Ga, and corresponds to a period of emplacement of voluminous granitoids in a relatively low-strain regime (Anhaeusser and Robb, 1983b; Belcher and Kisters, 2006a, b; Westraat et al., 2004). These granitoids formed of granodiorite, monzogranite and syenogranite are collectively referred to as the “GMS” suite (Anhaeusser and Robb, 1983b; Anhaeusser et al., 1983; Anhaeusser et al., 1981). They record the diversity of the craton-stabilizing processes, and are the focus of this work.

In Barberton (as elsewhere), these granitoids are essentially taken as reflecting reworking of the pre-existing TTG-dominated crustal basement (Anhaeusser and Robb, 1983b; Clemens et al., 2010). Their isotopic characteristics (Zeh et al., 2009) as well as those from their counterparts worldwide (Laurent et al., 2014a) are broadly consistent with this model. However, a viable petrological scenario is not as clearly established – partly because of the difficulty to melt large volumes of refractory TTG crust (Clemens et al., 2010; Watkins et al., 2007). Furthermore, the petrological diversity of the GMS suite suggests much more diverse processes.

In this work, we combine a detailed petrological/geochemical interpretation of the composition of the GMS granitoids, with U—Pb and Lu—Hf isotope analyses of samples representative of the different rock types, to propose an integrated model for the formation of the GMS suite and the stabilization of the South-Eastern Kaapvaal Craton at ca. 3.1 Ga. We show that although their petrological diversity requires a range of sources, within and below the crust, and different petrogenetic processes, all the GMS rocks were emplaced in a short period of time at 3110—3105 Ma, and have strikingly similar Hf isotopic characteristics with εHf ca. -2.0 at 3.1 Ga. We discuss the processes permitting this isotopic homogenization, yet preserving petrological diversity. Lastly, we comment on implications for craton stabilizing processes.

2. Geological setting

2.1 The BGGT

The Barberton Granite-Greenstone Terrain (BGGT), and the adjacent Ancient Gneiss Complex of Swaziland, constitute the core of the Kaapvaal craton in Southern Africa, with rocks formed between ca. 3.7 and 3.1 Ga. The Kaapvaal craton is unconformably overlain by several supracrustal sequences mainly formed in intracratonic settings, starting with the Dominion Group (ca. 3.07 Ga), followed by the Witwatersrand (ca. 2.9-2.7 Ga), Ventersdorp (2.73-2.65 Ga), and Transvaal (2.65-2.06 Ga) Supergroups, and further younger sequences. These all attest to the fact that by ca. 3.1 Ga, the Kaapvaal craton had become a stable continental mass, that was intermittently modified by tectono-magmatic processes, leading to the formation of large basins and the Ventersdorp and Bushveld LIP's. The BGGT is made of several units. The Barberton greenstone belt (BGB; review in e.g. Lowe et al., 2012; Lowe and Byerly, 2007) is made up of low-grade supracrustal rocks, starting with mafic/ultramafic sequences of the Onverwacht Group (3530-3260 Ma), followed by the composite Fig Tree Group (3260-3230 Ma) including intermediate to felsic lavas, clastic and chemical (BIF) sediments, and capped by the Moodies Group (3230-3210 Ma) made of a thick sequence of conglomerates and mature sandstones. The Moodies Group unconformably overlies the older units,

and is itself folded in steep, narrow synclines that define today's map pattern (Anhaeusser et al., 1981; Lowe et al., 2012). The change in sedimentation patterns, together with the deformation of the belt, points to a major tectonic event (or events) at Fig Tree to (post) Moodies times, i.e. ca. 3.25-3.20 Ga. This is also the age of amphibolite facies metamorphism, as recorded in the gneiss terrain that surrounds the belt (Cutts et al., 2014; Dziggel et al., 2005; Dziggel et al., 2010; Dziggel et al., 2002; Mühlberg et al., in revision).

The Barberton belt is surrounded by plutonic rocks and orthogneisses. Rocks older than 3.22 Ga are TTGs, and they formed during three main events (review in Moyen et al., 2018) at ca. (i) 3.51 Ga (the Steynsdorp pluton), (ii) 3.45 Ga (the Stolzburg and Theespruit plutons, as well as smaller bodies around them) and (iii) 3.28 Ga (older phases of the Badplaas gneisses) to 3.22 Ga (younger Badplaas gneisses, Nelshoogte and Kaap Valley plutons). The TTG plutons are thus roughly coeval with the formation of parts of the Barberton belt and felsic volcanic units of the same age are recorded in the belt. The felsic schists of the Theespruit Formation emplaced at ca. 3.51-3.53 Ga (Kröner et al., 2016; Kröner et al., 1996; Van Kranendonk et al., 2009), the H6 member of the Hooggenoeg Formation erupted at 3.45 Ga (de Vries et al., 2006; Laurent et al., 2020) and the Fig Tree Group lavas and volcaniclasitic rocks formed at ca. 3.25 Ga (Byerly et al., 1996; Toulkeridis et al., 1999; Zeh et al., 2013).

South of the BGB, the Swaziland Ancient Gneiss Complex (AGC) represents a middle- to lower-crustal domain (Hoffmann and Kröner, 2018; Kröner et al., 2019), presumably exhumed against the BGB at ca. 3.2 Ga along structures now obscured by younger intrusives (Lana et al., 2011; Schoene and Bowring, 2010). The AGC is made of interlayered components including (i) meta-plutonic units, with ages equivalent to the plutonics around the BGB; (ii) meta-sedimentary units with ages corresponding to both the older (Theespruit) components of the BGB (e.g. Kröner et al., 2019; Kröner and Tegtmeyer, 1994; van Schijndel et al., 2017) and the younger (Fig Tree) units (Taylor et al., 2013; Taylor et al., 2016). Collectively, the AGC appears as an equivalent of the BGB and surrounding plutons (or at least of the southern domain of the BGGT, Zeh et al., 2009), buried to mid-crustal depths and deformed, probably during the ca. 3.2 Ga evolution (Kröner et al., 2018; Schoene and Bowring, 2010; Schoene et al., 2008; Taylor et al., 2016).

Plutonic rocks after ca. 3.2 Ga shift to more potassic compositions, ranging from granodiorites, to granites and syenites. They are recorded over a long period of time, from about 3201 Ma for the Dalmein pluton, to less than 2700 Ma for the Mpageni pluton and other 'late granites' of Swaziland (Meyer et al., 1994; Zeh et al., 2009; Zeh et al., 2011). However, they are especially prolific at ca. 3.1

Ga, the emplacement time of the large GMS (granodiorite-monzogranite-syenite) suite that covers large portions of the BGGT (Figure 1).

2.2 The GMS batholiths

The GMS suite consists of four main batholiths (Figure 1): the Nelspruit batholith to the North of the Barberton belt, the Pigg's Peak batholith to the South-East (in Swaziland), the Mpuluzi batholith to the South, and the Heerenveen batholith to the South-West (Anhaeusser and Robb, 1983b; Anhaeusser et al., 1981; Robb et al., 1983). The GMS batholiths form voluminous, sheet-like laccoliths of only a few km thickness, covering large areas, and are composite but dominantly granodioritic to monzogranitic. They are accompanied by smaller bodies of syenite to syenogranite: the Boesmanskop, Weergevonden (also referred as the "Boesmankop tail") and Kees Zyn Doorns intrusions form elongated small bodies emplaced at about the same age as the larger batholiths (Anhaeusser et al., 1983). Existing geochronological constrains (Kamo and Davis, 1994; Westraat et al., 2004; Zeh et al., 2009) point to a short-lived emplacement, between 3110 and 3100 Ma, for the GMS suite.

This study focuses on the Heerenveen batholith, the smallest and best studied of the GMS suite. For comparison, we also include whole-rock data as well as some zircon analyses from the north-eastern margin of the adjacent Mpuluzi batholith.

2.3 The Heerenveen batholith

Located to the southwest of the Barberton Greenstone Belt, the Heerenveen batholith is the smallest of the GMS batholiths, approximately 30×15 km. The Heerenveen batholith has been studied in detail by Belcher and Kisters (2006a, b) who have established the following chronology of emplacement. The Heerenveen batholith is composed of eight different facies emplaced during four main stages of intrusion (Figure 2): (i) Stage I: a first leucogranite (leucogranite I) was emplaced as sheets in the gneissic basement; (ii) Stage II: emplacement of a large homogeneous, weakly deformed, body of porphyritic granite (megacrystic granite), forming the main phase in the Heerenveen (as well as in the Mpuluzi) batholith; (iii) Stage III: a series of smaller, strongly deformed bodies, comprising a second phase of leucogranite (leucogranite II), a quartz-monzonite and a first phase of pink granite (pink granite I), were injected into shear zones developed at the margin of the batholith; and (iv) Stage IV: post-tectonic intrusion of a second phase of undeformed pink granite (pink granite II).

Broadly, this emplacement sequence is also observed in the adjacent portion of the large Mpuluzi batholith [(Moyen et al., in press; Westraat et al., 2004) and unpublished maps and reports by A. Kisters (Stellenbosch University) and students (G. Sonke, C. Campbell, 2006)]]. The Boesmanskop syenite intrusion, now topographically isolated from the Mpuluzi batholith, likely belonged initially to the same intrusive complex. The Heerenveen and Mpuluzi batholiths are separated by a deep valley floored by gneisses, suggesting that the two may have formed an originally continuous carapace (Anhaeusser and Robb, 1983b). On the other hand, the valley separating the two batholiths lies along strike of the Inyoni shear zone, an important feature of the BGGT (Dziggel et al., 2005; Dziggel et al., 2002; Moyen et al., 2006; Van Kranendonk et al., 2014; Wang et al., 2019)(Figure 1). This feature also coincides with an isotopic boundary between two domains, "Barberton North" and "Barberton South" (Zeh et al., 2009), and correlates with a significant geophysical break in the craton (de Wit et al., 1992).

Clemens et al. (2010) gave a detailed account of the diverse facies comprising the Heerenveen batholith, based on the mapping by Belcher et al. (2006a, b) that we also use here (Figure 2). The north-western portion of the Mpuluzi batholith has been described in detail by Westraat et al. (2004) and summarized below (Figure 3). All the facies encountered in the Heerenveen batholith contain quartz, microcline and plagioclase, in various proportions. The porphyritic crystals in the megacrystic granite are mostly euhedral microcline, or in some outcrops quartz. Muscovite has been observed in sheared leucogranites I & II. Biotite, typically chloritized, is the ubiquitous mafic mineral, and the quartz-monzonite also contains hornblende and euhedral titanite.

This work is based on whole rock geochemistry of the Heerenveen (and parts of Mpuluzi) batholiths, as well as U-Pb dating and Hf isotope analyses of zircons from selected samples. Fourteen samples from Heerenveen and four from Mpuluzi have been studied. They cover most of the lithologic and geochemical diversity of the batholiths.

2.4 The Lower Onverwacht Group

Meta-sediments have been suggested as a possible source for the Heerenveen magmas (Clemens et al., 2010), and were consequently investigated in this work.

The lowermost portion of the Onverwacht Group mostly comprises mafic and ultramafic schists and amphibolites, but also contains some layers of felsic schists that are regarded as felsic meta-volcanic or volcaniclastic rocks (Anhaeusser et al., 1981; Kröner et al., 1996; Lowe et al., 2012; Lowe and Byerly, 2007; Van Kranendonk et al., 2009). Felsic schists occur in two formations, the Sandspruit and Theespruit Formations. The Theespruit formation is relatively coherent, whereas most of the Sandspruit Formation occurs as enclaves in the plutons and gneisses of the Stolzburg block South of

the BGB. As formation-level correlations are difficult, and beyond the scope of this work, we do not attempt further subdivision and rather refer to the Lower Onverwacht Group.

The felsic schists were dated in two areas, around the Steynsdorp pluton (Kröner et al., 2016; Kröner et al., 1996) and North of the Theespruit pluton, in the footwall of the Komati fault (e.g. the "Tjakastad water tower" locality; Kröner et al., 2016; Van Kranendonk et al., 2009). In both areas, the age of the protolith is ca. 3530 Ma. The Lower Onverwacht Group also includes rare occurrence (reported in Dziggel et al., 2002) of a coarse-grained quartz-plagioclase-microcline-clinopyroxene clastic meta-sediment with a maximum age of sedimentation of ca. 3520 Ma, and interpreted as a meta-arkose.

In order to further characterize the Lower Onverwacht Group, and explore its suitability as a source for the GMS rocks, we included five samples of it in our study. Four samples are felsic agglomerates from the Tjakastad Schist Belt (Diener et al., 2005), a previously undated portion of the Lower Onverwacht Group. The fifth sample comes from an 'arkose' fragment, sample (BE5), previously studied by Dziggel et al. (2002) and Diener and Dziggel (in press).

3. Analytical methods

3.1 Bulk rock composition

Bulk rock compositions for samples collected in this work were commercially obtained at ALS Global labs Ireland, using their "Complete Characterization Package" (see details at https://www.alsglobal.com/en-au/services-and-products/geochemistry/geochemistry-testing-and-analysis/whole-rock-analysis-and-lithogeochemistry). In addition, we compiled a database of published rock compositions drawing primarily on data by Anhaeusser et al. (1983a), Westraat et al (2004) and Clemens et al. (2010). Existing analyses do not always report trace elements and the final database (Data Repository, Item DR1) includes 88 new analyses, mostly of the Heerenveen batholith, and 289 from the literature. In total, we have 28 analyses from the Boesmanskop, 197 from the Mpuluzi, and 152 from the Heerenveen intrusions. Most of the published data does not include reference to the facies that we describe here and accordingly have been assigned on the basis of (i) the field description, when available; (ii) geochemical properties ; and (iii) the geographic location.

3.2 U-Th-Pb isotope analyses

Uranium, thorium and lead isotopes were analyzed using a ThermoScientific Element 2 sector field ICP-MS coupled to a Resolution M-50 (Resonetics) 193 nm ArF excimer laser (ComPexPro 102F, Coherent) system at Goethe-University Frankfurt (GUF). Data were acquired in time resolved – peak

jumping – pulse counting / analogue mode over 466 mass scans, with a 20 second background measurement followed by 21 second sample ablation. Laser spot-size was 19 µm for unknowns and the standard zircon OG1, 33 µm for the standard zircons GJ1 (primary standard), and 40 µm for the standard zircon 91500. The results of the standard zircon measurements obtained during the different analytical sessions are shown in Data Repository, item DR2. Sample surface was cleaned directly before each analysis by three pulses pre-ablation. Ablations were performed in a 0.6 l min^{-1} He stream, which was mixed directly after the ablation cell with 0.007 l min^{-1} N_2 and 0.83 l min^{-1} Ar prior to introduction into the Ar plasma of the SF-ICP-MS. All gases had a purity of >99.999% and no homogeniser was used while mixing the gases to prevent smoothing of the signal. Signal was tuned for maximum sensitivity for Pb and U while keeping oxide production, monitored as $^{254}UO/^{238}U$, below 0.7-0.3%. The sensitivity achieved was in the range of 9000-14000 cps/µg g^{-1} for ^{238}U with a 26 µm spot size, at 5.5 Hz and about 4 J cm^{-2} laser energy. The typical penetration depth was about 10-20 µm (spot size dependent). The two-volume ablation cell (Laurin Technic, Australia) of the M50 enables detection and sequential sampling of heterogeneous grains (e.g., growth zones) during time resolved data acquisition, due to its quick response time of <1s (time until maximum signal strength was achieved) and wash-out (< 99.9% of previous signal) time of about 2s. With a depth penetration of ~0.7 µm.s^{-1} and a 0.46 s integration time (4 mass scans = 0.46 s = 1 integration) any significant variation of the $^{207}Pb/^{206}Pb$ and $^{238}U/^{206}Pb$ in the µm scale is detectable. Raw data were corrected offline for background signal, common Pb, laser induced elemental fractionation, instrumental mass discrimination, and time-dependent elemental fractionation of Pb/U using an in-house MS Excel© spreadsheet program (Gerdes and Zeh, 2006; Gerdes and Zeh, 2009). A common-Pb correction based on the interference- and background-corrected ^{204}Pb signal and a model Pb composition (Stacey and Kramers, 1975) was carried out. The ^{204}Pb content for each ratio was estimated by subtracting the average mass 204 signal, obtained during the 20 second baseline acquisition, which mostly results from ^{204}Hg in the carrier gas (c. 230-350 cps), from the mass 204 signal of the respective ratio. For the analyzed sample the calculated common ^{206}Pb contents was mostly <0.5% of the total ^{206}Pb but in very rare cases exceeded 4% (Data Repository, item DR2). Laser-induced elemental fractionation and instrumental mass discrimination were corrected by normalization to the reference zircon GJ-1 (Jackson et al., 2004). Prior to this normalization, the inter-elemental fractionation ($^{206}Pb^*/^{238}U$) during the 21s of sample ablation was corrected for each individual analysis. The correction was done by applying a linear regression through all measured, common Pb corrected ratios, excluding the outliers (± 2 standard deviation; 2SD), and using the intercept with the y-axis as the initial ratio. The total offset of the measured drift-corrected $^{206}Pb^*/^{238}U$ ratio from the "true" ID-TIMS value (0.0983 ± 0.0004; ID-TIMS GUF value) of the analyzed GJ-1 grain was between 4 and 14% (during all analytical sessions) and the drift over the day, during the different analytical session between 1 and 8%.

Reported uncertainties (2σ) of the $^{206}Pb/^{238}U$ ratio were propagated by quadratic addition of the external reproducibility (2 SD) obtained from the standard zircon GJ-1 (see Data Repository, item DR2) and the within-run precision of each analysis (2 SE; standard error). In case of the $^{207}Pb/^{206}Pb$ we used a ^{207}Pb signal dependent uncertainty propagation (Gerdes and Zeh, 2009). The $^{207}Pb/^{235}U$ ratio is derived from the normalized and error propagated $^{207}Pb/^{206}Pb^*$ and $^{206}Pb^*/^{238}U$ ratios assuming a $^{238}U/^{235}U$ natural abundance ratio of 137.88 and the uncertainty derived by quadratic addition of the propagated uncertainties of both ratios. The analytical results are presented in data repository. The accuracy of the method was verified during the different sessions by analyses of reference zircon 91500, Plešovice, and OG1, that yielded Concordia ages of 1065.5 ± 6.7 (n=7, MSWD=0.22, Prob.=0.89); 339.1 ± 2.4 Ma (n=32; MSWD=0.98, Prob.=0.32), and 3461.3 ± 6.4 Ma (n=45; MSWD=0.77, Prob.=0.38), respectively (Data Repository, item DR2), identical within error of the quoted TIMS values of 1065.4 ± 0.4 Ma (Wiedenbeck et al., 2004), 337 ± 0.37 Ma (Sláma et al., 2008), and of 3465.4 ± 0.6 Ma (Stern et al., 2009). The data were plotted using ISOPLOT (Ludwig, 2001)

3.3 Lu-Hf isotope analyses

Hafnium isotope measurements were performed with a Thermo-Finnigan NEPTUNE multi collector ICP-MS at GUF coupled to the same laser as described in the U-Pb method (Resolution M-50 193 nm ArF excimer laser). Round or rectangular laser spots with diameters or edge lengths of 33-40 µm were drilled with repetition rate of 5.5 Hz and an energy density of about 6-7 J/cm^2 during 55 s of data acquisition. All data were adjusted relative to the JMC475 of $^{176}Hf/^{177}Hf$ ratio = 0.282160. Quoted uncertainties are quadratic additions of the within run precision of each analysis and the reproducibility of the zircon standard GJ1 which ranged between 0.0048% and 0.0070% (2SD) during the different analytical sessions (Data Repository, item DR3). Accuracy and external reproducibility of the method was verified by repeated analyses of reference zircons GJ-1, 91500, and Plešovice, which yielded $^{176}Hf/^{177}Hf$ of 0.282003 ± 0.000024 (2SD, n=9), 282290 ± 0.000022 (n = 9), and of 0.282465 ± 0.000019 (n=7), respectively (Data Repository, item DR3). These ratios are well within the range of solution mode data (Gerdes and Zeh, 2006; Woodhead and Hergt, 2005).

For calculation of the epsilon Hf [εHf_t] the chondritic uniform reservoir (CHUR) was used as recommended by Bouvier et al. (2008), i.e. $^{176}Lu/^{177}Hf$ and $^{176}Hf/^{177}Hf$ of 0.0336 and 0.282785, respectively, and a decay constant of 1.867 x10^{-11} (Scherer et al., 2001; Söderlund et al., 2004). Initial $^{176}Hf/^{177}Hf_t$ and εHf_t for all analysed zircon domains were calculated using the respective intrusion ages (Data Repository, item DR3). Depleted mantle hafnium model ages (T_{DM}) were calculated using values for the depleted mantle as suggested by Blichert-Toft et al. (2010) , with $^{176}Hf/^{177}Hf$ =

0.283294 and a $^{176}Lu/^{177}Hf$ of 0.03933, corresponding to a straight DM-evolution line with εHf_{today}=+18 and $\varepsilon Hf_{4.558Ga}$=0. T_{DM} ages for all data were calculated by using the measured $^{176}Lu/^{177}Hf$ of each spot for the time since zircon crystallization (= intrusion age), and a mean $^{176}Lu/^{177}Hf$ of 0.0113 for average continental crust (average from Taylor and McLennan, 1985; Wedepohl, 1995).

4. Geochemistry of the Heereveen batholith

From a geochemical perspective, the multiple facies of the GMS rocks in the southern BGGT are divided into three main groups and several sub-groups (Figure 4; Table 1). The first two groups (low-Ca granitoids, and syenites and related rocks) match the descriptions of Clemens et al. (2010), who refer to these as high and low SiO_2 respectively (limit at 71 %). The high-SiO_2 group (our low-Ca granitoids) is the dominant rock type, and only some of the stage III intrusives (monzonites, pink granite I) belong to the low SiO_2 group (our syenites). We identify here, in addition, a group of "dark granitoids" mostly present in the Mpuluzi batholith but also forming rare dykes in the Heerenveen body. They are petrographically similar to the Hebron phase of the Nelspruit Batholith (Cornwright et al., 2008).

4.1 Major elements and granite types

Most chemical classifications of granitoids (Bonin et al., 2020; Debon and Lefort, 1983; Frost et al., 2001; Moyen, 2019; Stussi, 1989) acknowledge that a handful of parameters are required for a full chemical description, and these parameters appear in different forms in commonly used diagrams (Figure 4) : (i) indicators of *differentiation* (e.g., SiO_2, or FeOt + MgO); (ii) proxies for the *plagioclase to K-feldspar* ratio, e.g. molar balance between Ca, Na and K ; (iii) the balance between *Na and K*; (iv) estimates of the *excess or deficit* of *Al* relative to the feldspar stoichiometry (A/CNK, normative corundum, etc.); (v) the balance between *Fe and Mg* (mg#, FeOt/MgO, etc.). The GMS granitoids are here described in these terms.

4.1.1 The dominant low-Ca granitoid types

The term "low Ca" was initially proposed by Champion et al. (1997) to describe large, leucocratic batholiths, generally syn-tectonic and shallowly emplaced, in the Yilgarn craton of Western Australia. The Yilgarn low-Ca granitoids have variable K/Na ratios, and are associated with minor units of more mafic granitoids, emphasizing their similarity with the Barberton GMS suite.

The GMS low Ca granitoids are leucocratic (SiO_2 > 71 %) and are represented by the main megacrystic phases of both the Mpuluzi and Heerenveen batholiths, as well as the leucogranites in the two bodies. They constitute the bulk, perhaps 90 %, of the Heerenveen and Mpuluzi batholiths and collectively represent large volumes of magma. They are weakly peraluminous, although for such

SiO_2 levels this is not a discriminatory feature as most granites converge towards this portion of geochemical space (Bonin et al., 2020). They are calc-alkalic to alkali-calcic and may be magnesian or ferroan, although this too is non-diagnostic. They also range from low to high K_2O (1 to 5 %), and can on this basis be subdivided into three sub-groups (low, medium and high K_2O; Table 1), that correspond to different mappable facies (Table 1; Figure 2). The high-K_2O subgroup tends to be more aluminous than the other subgroups.

In general, the low-Ca granitoids of the Mpuluzi batholith are more potassic than their counterparts in the Heerenveen batholith. The main Mpuluzi megacrystic granite is high-K_2O, and so are the majority of the leucogranites. One facies only has intermediate K_2O contents. In contrast, the main Heerenveen megacrystic granite and the leucogranite I are low in potassium, and only the Heerenveen leucogranite II has intermediate K_2O contents.

4.1.2 The late syenites and related rocks

Syenites, monzonites and pink granites represent a minor (5-10 %) component of the Heerenveen and the Mpuluzi batholiths (Figure 2), as well as the bulk of the Boesmanskop intrusion. They define a magmatic series, ranging from ca. 60 to 70 % SiO_2, and are invariably high- to ultra-high-K_2O (5 – 6 % K_2O even at lower SiO_2 contents). They are mostly metaluminous, ferroan and alkali-calcic to alkalic. At high SiO_2, the composition of the syenites overlaps with the high-K_2O members of the low Ca group, but they belong to distinct mappable units and thus represent different magmas.

4.1.3 Minor dark granites

Dark granites constitute a rather heterogenous, volumetrically small, group of lithologies (perhaps 1-5 %), seldom large enough to be discriminated on a map. They are generally late in the intrusion sequence, forming small dykes in older lithologies. Along the edge of the Mpuluzi batholith (Figure 3g), they occur as the matrix of a spectacular intrusion breccia with clasts of syenogranites wrapped in a dark augen granodiorite. In the core of the Mpuluzi batholith, published databases (unfortunately often lacking facies or outcrop descriptions: Anhaeusser and Robb, 1983a; Murphy, 2015) reveal the presence of scattered occurrences of chemically similar rocks, perhaps corresponding to the “veins” mapped in portions of the Mpuluzi batholith by Anhaeusser et al. (1981). In the Nelspruit Batholith, similar rocks form a discrete intrusion, the Hebron pluton (Anhaeusser et al., 1981; Cornwright et al., 2008). All of this is suggestive of late, syn-plutonic dykes injected into the partially consolidated magma reservoir, and possibly undergoing fragmentation into microgranular mafic enclaves (Barbarin, 2005).

The dark granitoids mostly have 60-65 % SiO_2, and variable characteristics summarized in Table 1. They define several series ranging from a low-K_2O, slightly peraluminous series to a high-K_2O,

metaluminous series, and in most diagrams (Figure 4) the various rock types occupy positions intermediate between the syenites and the other groups. Here too, the most differentiated units overlap in composition with the low-Ca granites, but the field context demonstrates that they belong to different magma batches.

4.2 Trace elements

4.2.1 An improved representation of trace element trends in granitoids

Trace elements are, in general, not particularly good petrogenetic tracers in granitoids (Bonin et al., 2020; Janoušek et al., 2016; Moyen and Laurent, 2018). Distributions are mostly controlled by accessory minerals (e.g. LREE in allanite or monazite, Zr and Hf in zircon, etc.), such that they provide little information on sources and processes. Like all igneous rocks, the composition of granitic melts is a function of the source composition and the melting process. Unlike mantle-derived rocks, however, the magnitude of the differences between different sources is much more important in granitoids than it is in mafic rocks, and therefore the trace element composition of granitoids is (with a few exceptions, such as the HREE fractionation in presence of garnet and amphibole) primarily a reflection of their source (Janoušek et al., 2010; Konopásek et al., 2018).

One may take advantage of this by devising spidergrams that magnify the differences between potential sources, thereby revealing meaningful petrogenetic processes.

In the original construction of spidergrams, elements are normalized against the inferred source, in this case the mantle, and arranged in order of decreasing incompatibility relative to MORB (Coryell et al., 1963; Masuda, 1957, 1962). Any deviation from a smooth pattern (or “anomaly”) can be interpreted as reflecting the effects of specific minerals – for instance Fe-Ti-oxides on the abundances of Nb and Ta. Following the same logic for granites, it is therefore useful to normalize the studied sample against a potential source, here the average Barberton TTGs (Table 2; Moyen et al., 2018), and Figure 5 depicts REE diagrams normalized to the average of Barberton TTG. Chondrite-normalized REE diagrams, for comparison, are in Figure SE1: supplementary online material. To further mimic the MORB approach, elements should be arranged in order of decreasing incompatibility with respect to a crustal melting scenario. In Figure 6 we show spidergrams that are (i) normalized to average TTGs and (ii) arranged by increasing variability: Schiano et al. (1993) suggested that variability within a suite correlates to bulk distribution coefficients, thus increasing variability should correspond to increasing compatibility.

This representation allows to evidence two important features. Firstly, the trace elements patterns within each group (or subgroup) are similar, confirming that each group forms a magmatic series in

which rock compositions are related by simple processes. Secondly, the groups show different patterns. Therefore, they can hardly relate to the evolution of a common parental magma. A key observation is thus the presence of a very large range of petrologically unrelated magmas, as detailed below.

4.2.2 The low-Ca granitoids

The three sub-groups of the low-Ca granitoids are broadly similar, but with consistent differences. The low-K_2O sub-group has trace element patterns that are flat and close to normalized values of 1 and, therefore, do not differ much from an average Barberton TTG. The high-K_2O sub-group is up to 10 times enriched, and shows prominent anomalies for Eu, Sr and Ti. The medium K_2O sub-group exhibits intermediate characteristics.

The overall flat shape of the patterns is consistent with melting of a source with TTG-like trace elements composition. Other Archaean felsic rocks may however have similar trace element signatures, for instance clastic sediments derived from TTG erosion or composite Grey Gneisses containing a significant (meta-)TTG component. Sr, Eu and Ti anomalies suggest that the (high-K) melts coexisted with plagioclase and Ti-oxides at some point of the magma's evolution – either as a residual phase during melting, or a fractionated phase during crystallization.

In either case, the 10-fold enrichment observed in the high-K_2O sub-group suggests melt fractions of ca 0.1. With decreasing concentration of incompatible elements, and thus higher melt fractions, the anomalies are less pronounced, consistent with the progressive separation of melt and solid during melting or crystallization..

4.2.3 The syenites and dark granites

Both types of dark granitoids, as well as the syenites, have normalized REE patterns that are steeper than those of the low-Ca rocks. They have a small or insignificant Eu anomaly, and the typical REE pattern is S-shaped. Such a shape seems at odds with an origin from a TTG-like source (as suggested for the low-Ca granitoids), as this would require unprecedented decoupling of the REEs. Similarly, for the extended trace element patterns of Figure 6, the increase towards more compatible elements would imply, for rocks with a TTG-like source, a reversed order of incompatibility which is unlikely.

It is therefore much more likely that these rocks originated from a different source (see later for a more detailed discussion). Compared to TTGs, this source would have had negatively-sloped TTG normalized REE patterns. In a more conventional mantle- or chondrite-normalized diagram, the corresponding patterns would be steeper than TTGs. In terms of other trace elements, the source was TTG-like and more enriched in HFSE and HREE than in LILE and LREE. Negative anomalies in Sr or

Ti may either correspond to residual minerals (as was the case for the low Ca granitoids), or reflect such anomalies already in the source.

5. U—Pb—dating and Lu-Hf isotope results

5.1. The GMS samples

All 18 samples of the GMS suite yield magmatic zircon populations. Grains are euhedral and range from elongate, needle-like crystal habits (aspect ratios up to 9), to stubby morphologies (aspect ratios 2 to 3), even within individual samples (Figure 7). Zircons in the samples from the Mpuluzi batholith are commonly much larger and more equant (average length = 195 µm, width = 82 µm, aspect ratio = 2.5, n=185) compared to those from the Heerenveen samples (average length = 162 µm, width =52 µm, aspect ratio =3.4, n=506). In all samples zircons show an oscillatory zoning, but many grains also reveal altered domains (recrystallized and porous), or are highly fractured. Optically distinct cores are rare, and mainly were found in sample 11-15B, where CL-bright cores are commonly surrounded by CL-dark, strongly altered rims (Figure 7). Th/U ratios of all measured zircons ranges from 0.5 to 2, consistent with what is commonly observed in igneous zircons.

Example Concordia diagrams for the studied samples are presented in Figure 8, with the other diagrams in Figure SE2: supplementary online material. Zircons of most samples yielded similar Concordia ages at around 3105 Ma, with the most reliable dates (comprising at least 3 concordant analyses per samples) ranging from 3096 ± 19 to 3114 ± 12 Ma. These ages are in agreement with upper intercept ages obtained from the same samples, and with U-Pb ages previously obtained by ID-TIMS dating (Kamo and Davis, 1994; Westraat et al., 2004; for comparison see Table 3). Significantly older $^{207}Pb/^{206}Pb$ ages at about 3200 Ga were only found in 4 samples from the Heerenveen batholith, where eight analyses of zircon cores of sample HE 11-15B (in Figure 1: supplementary online material) yielded a Concordia age of 3201 ± 9 Ma. This age is slightly younger than that of the youngest TTG's observed in the Barberton Greenstone belt, which were emplaced at 3230-3210 Ma (see compilation in Moyen et al., 2018).

Hafnium isotope analyses obtained from zircon populations of all GMS samples, independent of composition and location are all similar (mostly identical within error) as shown in Table 4. Initial $^{176}Hf/^{177}Hf$ ratios range between 0.28071 ± 0.00003 and 0.28076 ± 0.00002 (2 sigma standard deviations), corresponding to εHf_t values between -0.9 ± 0.7 and -2.5 ± 1.7, and Hf model ages between 3.48 ± 0.02 Ga and 3.57 ± 0.05 Ga, respectively. Identical initial $^{176}Hf/^{177}Hf$ ratios of concordant and discordant zircons in individual samples suggest that all these grains/domains crystallised from the same isotopically homogeneous magma, but that certain domains underwent

445 significant Pb loss due to alteration, that nevertheless left the Hf isotope composition unchanged (Figure 2: supplementary online material; for more explanations see Gerdes and Zeh, 2009). Identical initial $^{176}Hf/^{177}Hf$ ratios of inherited zircons in sample HE 11-15B and magmatic zircons in the GMS indicate that magmas forming at c. 3.2 Ga and c. 3.1 Ga in the BGB all had similar Hf isotopic compositions. The Hf isotopic compositions of the GMS zircons overlap with those of the 3.23 Ga
450 TTG's of the Barberton North domain (Kaap Valley and Nelshooghte), showing $^{176}Hf/^{177}Hf$ ratios between 0.28073 ± 0.00002 and 0.28076 ± 0.00002, respectively (Zeh et al., 2009).

5.2. The Lower Onverwacht metasediments

Five samples from the Lower Onverwacht Group have been analysed. Four samples are meta-volcanic or volcaniclastic 'agglomerates' from the Tjakastad Schist Belt (Diener et al., 2005). The
455 other is a clastic meta-sediment ('arkose') from a greenstone remnant in the southern portion of the Stolzburg terrane (Dziggel et al., 2002).

Zircon grains of the four agglomerate samples are angular, have oscillatory and/or sector zoning, and contain recrystallized melt inclusions and apatite. Many grains show signs of alteration, re-crystallization and intense fracturing (Figure 7). Zircon analyses yield concordant and discordant ages,
460 with the oldest domains in all four samples plotting on Discordia lines with upper intercept ages around 3530 Ma. The most pristine zircon domains yield Concordia ages between 3524 ± 7 Ma and 3531 ± 7 Ma (Table 3; Figure 8e; Figure SE2: supplementary material). These ages overlap with those for Theespruit Formation meta-volcanics in the nearby Tjakastad area (ca. 3530 Ma; Kröner et al., 2016; Van Kranendonk et al., 2009). Younger ages, perhaps result from subsequent Pb-loss, either
465 related to emplacement of the adjacent Theespruit and Stolzburg Plutons at 3450 Ma, or later tectono-metamorphic-magmatic events which affected the BGGT at 3.23 Ga (Cutts et al., 2014; Diener et al., 2005; Diener and Dziggel, in press; Heubeck et al., 2013; Schoene and Bowring, 2010). Hafnium isotope analyses of zircon populations from the four agglomerates yielded similar initial $^{176}Hf/^{177}Hf$ ratios. These range between 0.28046 ± 0.00006 and 0.28048 ± 0.00007 (2 S.D.),
470 corresponding to εHf_t values between -1.4 ± 2.2 and -0.6 ± 2.4, and Hf model ages between 3.80 ± 0.13 Ga and 3.83 ± 0.12 Ga, respectively. The relatively wide scatter in εHf_t values (more than 4 epsilon units) of individual samples, suggests that the Theespruit meta-volcanics were sourced from magmas of variable composition, perhaps resulting from different crust and mantle contributions. The meta-agglomerate data overlap with those obtained by Kröner et al. (2016) from Theespruit
475 Formation felsic tuffs of the nearby Tjakastad area, that show an even wider range in εHf_t values from – 6.2 to +0.5.

Forty-five zircon grains with magmatic oscillatory zoning, and minor signs of alteration were analysed from the meta-arkose. Eighteen grains yielded concordant ages between 3510 and 3450 Ma, of which nine analyses yielded a Concordia age of 3510 ± 8 Ma [MSWD(c.+e.)=0.70, Probability(c.+e.)=0.80, c.+e. = concordance and equivalence] and 4 analyses 3464 ± 8 Ma [MSWD(c.+e.)=0.30, Probability(c.+e.)=0.95]. Two analyses gave concordant ages at about 3200 Ma (Figure 8f). The concordant age at 3510 Ma is slightly younger than the deposition age of 3520 Ma proposed by Dziggel et al. (2005), and also younger than the emplacement ages of ca. 3530 Ma for the agglomerates of the Tjakastad Schist belt (this study), and of 3534.4 ± 1.5 Ma, reported by Kröner et al. (2016) for the felsic tuffs from the same locality. The concordant age at c. 3465 Ma is slightly older than the emplacement age of the enclosing Stolzburg trondhjemites. Ages of ca. 3.2 Ga overlap with those reported by Wang et al. (2019) from zircons found in the immediate vicinity (samples 14SA36, 15SA36), suggesting some resetting of the ages during younger tectono-metamorphic events. Initial $^{176}Hf/^{177}Hf$ ratios of the detrital zircons in Theespruit arkoses (n=33) are generally higher than those obtained from the agglomerates, and reveal two clusters: (1) at $^{176}Hf/^{177}Hf$ = 0.280572 ± 0.000024 (n=18), corresponding to $\varepsilon Hf_{3.45\text{-}3.51Ga}$ =2.0 ± 0.7, and T_{DM}=3.66 ± 0.05 (4 zircons with ages between 3.45-3.51Ga), and (2) at $^{176}Hf/^{177}Hf$ = 0.280635 ± 0.000031 (n=14), corresponding to $\varepsilon Hf_{3.45\text{-}3.51Ga}$ = 4.2 ± 1.3, T_{DM}=3.51 ± 0.05Ga (8 zircons with ages between 3.45-3.51Ga).

6. Discussion

6.1 The Lower Onverwacht Group clastic meta-sediments

In this work, we report on the Hf isotopic composition of an uncommon occurrence of K-feldspar-rich meta-sediments from the Lower Onverwacht Group. This rock is petrologically similar to what Clemens et al. (2010) propose as the source of the Heerenveen batholith magmas, and we use it in the following discussion. However, the combined U-Pb-Hf isotopic compositions obtained from the detrital zircons of this rock deserve some comments in themselves.

Two populations of zircons are found in these arkoses, characterised by distinct $^{176}Hf/^{177}Hf$ values, plotting on two subparallel horizontal arrays between 3510 and 3300 Ma in the $^{176}Hf/^{177}Hf$ versus $^{206}Pb/^{207}Pb$ age diagram (Figure 3: supplementary online material). These arrays have two important implications, (1) they reveal that the detrital zircons were derived from two distinct sources within the crust and deposited from about 3510 Ma, and (2) that all ages <3510 Ma are likely, therefore to result from concordia-parallel Pb-loss (partial or complete). Pb-loss is commonly seen in Archean gneiss terranes, and is caused by multiple structural-metamorphic-magmatic overprints over a protracted period of time (for examples see Gerdes and Zeh, 2009; Zeh et al., 2009; Zeh et al., 2013;

Zeh et al., 2014). It is, therefore, probable that the clastic meta-sediments were deposited immediately after 3510 Ma, in general agreement with the interpretation of Dziggel et al. (2002), but that many grains underwent partial or complete Pb-loss during intrusion of the nearby Stolzburg and Theespruit plutons at ca. 3450 Ma and/or during subsequent structural metamorphic-magmatic events, which affected the BGS at c. 3.33 Ga, 3.25-3.20 Ga and c. 2.6-2.7 Ga (Details in Cutts et al., 2014; Heubeck et al., 2013; Schoene and Bowring, 2010). The grains with $^{207}Pb/^{206}Pb$ ages >3500 Ma always show lower U+Th contents (<250 ppm) compared to the younger grains (up to 600 ppm; see Data Item DR3). Thus it is possible that the younger grains accumulated more radiation damage compared to the older ones, and consequently were more metamict and sensitive to post-growth alteration. Nevertheless, a somewhat younger deposition age for the clastic meta-sediments, between 3510 and 3450 Ma, cannot completely be excluded. The only field constrain is that the Lower Onverwacht Group is intruded by the ca. 3450 Ma plutons of the southern BGGT (Anhaeusser et al., 1981; Moyen et al., 2018).

Questions remain regarding the source(s) of the two zircon populations in the Lower Onverwacht arkoses. As shown in Figure 9, the Hf isotope composition of both populations overlaps with data obtained from detrital zircons in Paleoarchean clastic sedimentary rocks (greywackes, quartzites and metapelites) of Swaziland in the Luboya-Kubuta river area (Taylor et al., 2016), and from the Dwalile Greenstone Belt (van Schijndel et al., 2017). This suggests that all these sediments originated from similar sources such as felsic rocks of juvenile character that occurred relatively widespread during the Paleoarchean. Nevertheless, their source(s) remain enigmatic. The hafnium-age signatures exclude coeval juvenile mafic rocks of the BGB, but also more felsic rocks of the Ancient Gneiss Complex, and the Lower Onverwacht volcanics. The mafic rocks, in particular the fine grained basalts as exposed in the Overwacht group, would supply no or few zircon grains, and most felsic rocks have lower εHf_t values (see Figure 9a). The very radiogenic composition ($\varepsilon Hf = +4$) of some of the zircon grains points to the existence of an early depleted mantle reservoir in the southeastern Kaapvaal craton, a feature also evident in mafic rocks from the area (Hoffmann and Wilson, 2017; Nebel et al., 2014; Schneider et al., 2019; Wilson et al., 2003). In addition, it requires that juvenile mafic rocks were transformed into felsic rocks immediately after their extraction from the mantle, either by fractional crystallisation within oceanic plateaus (similar to processes in the Rooiwater Complex of the Murchison Greenstone Belt further North: Laurent et al., 2019) or by melting of hydrated mafic crust.

6.2 The sources of the GMS suite

Compared to the TTG granitoids, the GMS suite has been less well studied. Early studies do not describe the range of rocks found in the batholiths, but are rather concerned with the dominant,

« core » phases of both Mpuluzi and Heerenveen batholiths, a justifiable choice given the relative volumes but nonetheless one that misses part of the story. Early work (Anhaeusser and Robb, 1983b; Robb et al., 1983), reiterated by Cornwright et al.(2008) and Robb et al. (2007), proposed that the GMS granitoids formed by melting of the TTG basement at crustal depths. This model is the underlying concept in more recent studies (Zeh et al., 2009) who described the post-3.2 Ga granitoids in Barberton area as resulting from « recycling » of older crust, but without detailing the petrogenetic process involved.

Clemens et al. (2010) offered a dissenting view. Based on experimental results (Watkins et al., 2007), they concluded that melting of TTGs cannot generate melts as potassic as the GMS suite, and that a more potassic source is required. They also noted the various rock types in the Heerenveen batholith and proposed that they reflect the implication of sources ranging from mafic to felsic, potassic igneous rocks or volcaniclastic rocks derived from such lavas (i.e. analog to modern subduction-related basalt-andesite-dacite-rhyolite series, similar to some components of the Fig Tree Group, and themselves formed by melting of a metasomatized mantle), all melting to produce the granitoids.

Here we revisit these findings in the light of our new isotopic constrains.

6.2.1 Different magmatic series

The GMS suite is characterized by a wide range of compositions, which correspond to different types of granitoids – possibly reflecting different magmas and sources.

Granitoids are not necessarily chilled melts but may represent the product of more complex magma chamber processes such as melt extraction from a solidifying mush (Bachmann and Bergantz, 2004).The texture of some of the GMS rocks, that of the syenites in particular (Figure 3d, I, j) certainly suggests that they might be the products of feldspar accumulation. Nonetheless, it seems difficult to use this as an explanation for the whole range of compositions featured in the GMS suite. In this case, one should observe an array trending towards the composition of K-feldspar, which is clearly not the case. The different trace element patterns between rock types also do not support such a model. It seems difficult, therefore, to propose that all the diverse GMS rock types reflect differentiation from a common parent, and we propose that the different rock types correspond to different magmas. Despite this feature, it is also apparent that the GMS suite exhibits homogeneous initial Hf isotope compositions, and petrogenetic models therefore need to accommodate a process that can explain this paradox.

6.2.2 The origin of the low-Ca granitoids

With weakly peraluminous composition, no clear differentiation trend (and an overall high-SiO_2 nature), as well as generally high levels in incompatible elements and negative εHf_t values, there is little that can relate the low-Ca granitoids to differentiation of mantle-derived mafic magmas (as proposed for instance by Kleinhanns et al., 2003). Rather, models involving melting of crustal lithologies from the BGGT are considered.

Figure 10 includes only samples from a geochemically homogeneous group (the low-Ca granitoids), thus reducing the impact of different source compositions; and uses tracers that are likely not controlled by accessory minerals. A first observation is the scatter of compositions in all the diagrams. This effectively rules out a single process forming a unique magmatic series. The origin of the low-Ca granites is thus composite.

From the laws of trace elements behaviour, the shapes of the trends generated by partial melting and fractional crystallization are expected to differ (Janoušek et al., 2016, chapter 21). In *log(compatible)* vs *log(incompatible)* diagrams (Figure 10a), partial melting generates shallow trends and fractional crystallization steeper ones (e.g. Robb, 1983). Both are evident for different sub-groups of the low-Ca granitoids. In *X/Y* vs. *X* diagrams, where *X* and *Y* are both incompatible (Figure 10b), fractional crystallization generates flat trends and melting forms sloped trends (Minster and Allègre, 1978). Again, both are evident in the low-Ca granitoids. In particular, the high-K_2O leucogranites and megacrystic granites from the Mpuluzi batholith depict rather clear fractionation trends whereas the low- and medium-K_2O granitoids seem to be governed by partial melting processes.

Th—U and K—Th diagrams (Figure 10c and d) do not allow such a clear discrimination of processes, but are nevertheless good tracers of the sources or the initial magmas (Cuney et al., 1989; Friedrich et al., 1987). Here it is clear that the low-Ca granitoids do not generate a single trend, but rather require parallel evolution from a range of primitive magmas, themselves originating from diverse sources.

Collectively, the low-Ca granitoids therefore appear to result from (i) melting of compositionally varied (although broadly similar, as they have similar major element properties) sources and (ii) fractionation of some of the magma batches. This is, of course, a rather common scenario for the formation of crustally-derived granites/leucogranites (Clemens et al., 2009; Cuney et al., 1989; Stussi, 1989; Turpin et al., 1990). The feasibility of various lithologies in the BGGT as sources for these rocks is now considered:

Mafic rocks. From a purely isotopic point of view (Figure 9a), mafic rocks may be possible sources for the GMS granitoids. However, ample petrological evidence in particular from experimental petrology (reviews in e.g. Hoffmann et al., 2018; Moyen and Stevens, 2006) demonstrates that melting of mafic rocks does yield potassic liquids but rather sodic (TTG) magmas. TTGs are indeed found in the BGGT and in Swaziland at 3.33 – 3.22 Ga and their isotopic characteristics perfectly fit the crust evolutionary trend defined by the $^{176}Lu/^{177}Hf$ ratios of the mafic rocks (Figure 9a). Thus, we rule out common mafic rocks of the BGB as a possible source for the low-Ca granitoids.

Intermediate supracrustal rocks. Clemens et al. (2010) propose that the dominant rock types of the Heerenveen batholith form by melting of volcanic or volcaniclastic rocks rather than the commonly assumed TTGs. Such rocks are more potassic and more hydrous than typical TTGs, and are thus a better source to form large volumes of potassic magmas. Several sedimentary or volcano-sedimentary units are known in and around the BGB, although generally in small volumes: (i) components of the ca. 3530 Ma Lower Onverwacht Group; (ii) large parts of the ca. 3250 – 3300 Ma Fig Tree Group; (iii) the ca. 3210 Ma Moodies Group.

The Lower Onverwacht Group occurs as fragments in the amphibolite-facies terrane south of the BGB (the Stolzburg block), where it occupies a very minor area. It is dominated by amphibolites with subordinate felsic schists, interpreted as former volcanic and volcaniclastic rocks, with very minor clastic metasediments. The protoliths of the felsic schists of the Theespruit Formation erupted ca. 3530 Ma ago, and have εHf_t between -3 and +1. Evolution from these values, with the appropriate bulk rock composition ($^{176}Lu/^{177}Hf$ = 0.005 to 0.009) projects to εHf_t of -4 to -10 at 3100 Ma, below the compositions of the GMS suite. Zircon from the Theespruit clastic meta-sediments reveal two clusters, both with suprachondritic εHf_t between +2 and +4 at ca. 3510 Ma. Using an average $^{176}Lu/^{177}Hf$ ratio for continental rocks of 0.0113, they project to -2 to -4 at 3100 Ma, i.e. on the lower end of the GMS granitoids.

A higher $^{176}Lu/^{177}Hf$ ratio would allow an evolution to εHf values of ca. -1 at 3100 Ma, overlapping with the GMS magmas. This requires $^{176}Lu/^{177}Hf$ ratios higher than those observed in Barberton felsic rocks (0.015), which is possible assuming that some of the detrital zircon grains survived partial melting, consequently increasing the apparent $^{176}Lu/^{177}Hf$ ratio of the extracted melt. However, this seems at odds with the lack of inherited grains with ages >3200 Ma in the GMS rocks, and with relatively elevated Zr contents (and thus zircon saturation temperatures in excess of 800 °C). At more than 800 °C, clastic meta-sediments would melt 30-40 % (Vielzeuf and Montel, 1994), rendering zircon preservation unlikely. Thus, arkoses of the Lower Onverwacht Group may represent a source for the GMS magmas but only if one assumes the superposition of a variety of favourable

circumstances. Such arkoses are also limited in extent making it difficult to account for the widespread melting that must have taken place to accommodate the high volumes of melt required for GMS emplacement.

The Fig Tree Group contains felsic volcanic and volcaniclastic rocks as well as immature sandstones (Toulkeridis et al., 1999). Available Hf isotope data shows that zircons from the Fig Tree Group plot in a wide range, bound by the clastic meta-sediment evolution line. Felsic volcanic and volcaniclastic rocks represent a petrologically favourable lithology, very appropriate to generate GMS magmas (Clemens et al. 2010), and they are more abundant volumetrically than the Lower Onverwacht arkoses, but they still represent low volumes regionally. Furthermore only the combination of the most favourable circumstances (both $^{176}Lu/^{177}Hf$ ratio and original εHf_t values at the outer end of the observed range) could produce GMS-like compositions.

The same isotopic reasoning applies to the ca. 3210 Ma Moodies Group. Although the Moodies Group forms large volumes of rocks, only a small portion is made up of greywackes, volcaniclastic or volcanic rocks: the bulk of the Group is made of non-fertile quartz-rich sandstones.

In summary, from (isotope) geochemical points of view it is permissible but unlikely to generate the GMS magmas by melting of regional metasediments or metavolcanics. Furthermore, no know geological unit includes sufficient volumes of such rock types to generate the large volume of GMS granitoids that are preserved.

Meta-plutonic rocks. The conventional view on the formation of Archaean potassic granites is by melting of the volumetrically dominant TTG granitoids or meta-TTG gneisses that dominated the crust pre-3.1 Ga. The composition of the TTG basement around the BGB and Swaziland is well established. Using reasonable $^{176}Lu/^{177}Hf$ values, the older (ca. 3.53 Ga and ca. 3.45 Ga) generations of TTGs are not radiogenic enough to represent a potential source for the GMS magmas. On the other hand, the 3.28 – 3.23 Ga TTGs area better match. They span a very large range of εHf values (-2 to +3), that projects to about -4 to +1 at 3100 Ma, overlapping the range of GMS magmas. This source is also supported by the finding of zircon xenocrysts with ages of about 3200 Ma in some GMS samples. From a purely zircon isotopic perspective, they represent, therefore, the most likely source.

To some degree, this is in contradiction with the findings of Clemens et al. (2010), who found that TTGs are not an appropriate source for the GMS magmas. However, their argument is chiefly based on the low abundance of biotite in ordinary tonalites to trondhjemites of the TTG suite compared to more fertile rocks, therefore preventing the formation of large volumes of magmas at reasonable temperatures, and the formation of sufficiently K-rich melts (Watkins et al., 2007). However,

amongst the ca. 3.2 Ga TTGs, large volumes (in particular the Kaap Valley Pluton, the largest around the BGB; and portions of the Nelshoogte Pluton) are made of a relatively mafic (SiO_2 ≈ 60-65 %) tonalite to leucodiorite (Moyen et al., 2018), a rock that is mafic enough to contain large volumes of hydrous silicates such as biotite and amphibole. In fact, a mafic tonalite such as the Kaap Valley has a composition very close to a greywacke or an andesite, and thus would work just as well as a petrological source for the GMS rocks. Tonalites are also readily available in the BGGT, where they form large volumes of exposed rocks in the NW Barberton terrane, and occur more sporadically e.g. in Swaziland (part of the Usutu suite).

Combination of the above. An obvious problem with the GMS suite is the volume of source required. Assuming a conservative 20% melting of the source to form granitoids, a volume of source 5 times bigger than the granitoids is required. The present day Lower Onverwacht and Fig Tree Groups represent only small relicts at the surface. It is unlikely that they once formed effectively the bulk of the present day 100 x 200 km domain where the GMS granites occur. In fact, proposing any lithology to be homogeneous on that scale is not very realistic, which is in good agreement from our observations on the geochemistry of the low-Ca granitoids that require multiple continental sources (Figure 10).

The middle and lower Archaean continental crust is made up of Grey Gneisses, a complex lithological assemblage made of many tectonically transposed and interleaved types of rocks, dominated (but not restricted to) TTGs. Grey Gneisses however also include other components. To take one example, the nearby Ancient Gneiss Complex of Swaziland includes components that cover a range of composition much wider than simple TTGs (Hofmann et al., 2019; Hunter et al., 1978). Mid-crustal composite Grey Gneiss therefore forms a suitable source for the low-Ca portion of the GMS batholiths. It supplies a range of isotopically related (or similar) rocks with varying chemical compositions. Depending on the exact proportions of various components in the source rock, the resulting magmas could cover a range of compositions, all more potassic than the protolith. The sediments interleaved in the orthogneisses would of course derive from the TTG component in which they now occur and thus have the same isotopic (and trace elements, largely) properties, and amphibolite enclaves could be a further source of water stored in amphibole or biotite.

6.2.3 The origin of the syenites and related rocks

The origin of syenites is, generally, a controversial topic. A first issue is that many could be K-feldspar cumulates rather than chilled liquids, and indeed the textures of GMS syenites (Figure 3i, j) is consistent with this hypothesis. Even so, the formation of K-feldspar, quartz-free cumulates requires a liquid of an unusual, potassic and low silica, composition.

Like other syenites in the world (Harris et al., 1983; Tchameni et al., 2001; Woolley and Jones, 1987; Zanvilevich et al., 1995), the parental magma of the GMS syenites has been related to deep crustal melting (Anhaeusser and Robb, 1983b). However, in order to generate a low-silica, high-potassium liquid (rather than an A-type granite: Creaser et al., 1991; Skjerlie and Johnston, 1992), an already mafic and potassic crustal source is required, for instance a K-rich arc-like basalt (Clemens et al., 2010). Compared to experimental compositions, the syenitic component indeed plots in the field of melts formed by melting of high-K mafic compositions (Figure 11a; Laurent et al., 2014a). An issue with this model is the complete lack of such a component in the stratigraphy of the Barberton Greenstone Belt. However, from a geochemical point of view, most of the supporting evidence can also be interpreted in favour of differentiation of a similar K-rich basalt. This model is similar to what is generally offered for Phanerozoic high-K calc-alkaline granitoids (Couzinié et al., 2016; Fowler et al., 2008; Fowler and Rollinson, 2012) and Archaean sanukitoids (Laurent et al., 2014a; Laurent et al., 2014b; Martin et al., 2010). In these examples, the parental mafic component occurred as small volumes only and is seldom preserved in itself, but is invariably hybridized and differentiated, and is preserved only as small enclaves, dykes, etc. in the granitoids. Similar hybridization processes may account for the absence of a pristine high-K mafic component in the BGGT.

The syenitic component of the GMS suite offers similarities with the late-Archaean sanukitoids, in particular its K-rich nature for low silica contents, and the high Sr+Ba amounts. This is well expressed in the "FSMB" (= [FeOt + MgO] * [Sr + Ba]) component in the diagram of Laurent et al. (2014a) (Figure 11b). Sanukitoids are commonly associated temporally and spatially with syenites (Bibikova et al., 2006; Fayol and Jébrak, 2017; Heilimo et al., 2012; Lobach-Zhuchenko et al., 2008; Sutcliffe et al., 1993).

Sanukitoids (and related rocks) are potassic as a result of enrichment of the mantle source by small volumes of crustal components such as sediments, during lithosphere recycling previous to the melting. Given the imbalance of Hf (and also Sr or Nd) concentrations between sediments and the mantle, a small amount of contaminant (5-10 %) will effectively fully control the isotopic composition of the hybrid source (Couzinié et al., 2016). Since the sediments ultimately are derived from the local crust, the isotope composition of the resulting magmas is effectively undistinguishable from that of pure crustal reworking (Laurent and Zeh, 2015).

In the case of the GMS suite, the syenitic component would thus be related to burial of small portions of the local crust (with the characteristics we described previously) into the mantle, presumably during the ca. 3.2 Ga "orogenic" event (Moyen et al., 2006; Moyen et al., 2018; Schoene and Bowring, 2010). This would form a suitable mantle source for high K mafic magmas at ca. 3.1 Ga.

These magmas would subsequently inject the partially molten Grey Gneiss crust, differentiate and interact there, locally forming K-feldspar-rich cumulates representing the present-day syenites.

6.2.4 The origin of the dark granitoids

The dark granitoids are less common and less well constrained than the other two groups. They are relatively low silica, and are diverse in composition. Tentatively, we propose that they are also related to melts from the enriched mantle (much in the same way as the mafic components of the syenite group). In the case of crust-mantle hybrids such as envisioned here, the main control on the trace element composition of the liquid is the *F/a* ratio, namely the balance between the degree of melting (*F*) and the proportion of contaminant (*a*) (Moyen, 2009; Moyen, 2019). In this view, the smaller degree of incompatible element enrichment of the dark granitoids could be ascribed to a higher *F/a* ratio corresponding either to a lesser amount of mantle contamination or to a higher degree of melting. Since the crustal contaminant was the same material, the hybrid mantle source also inherited crustal characteristics.

The diversity within the dark granitoids also reflects partial melting of a heterogeneous mantle, with more or less enriched portions, related to input by crustal material with varying composition (sediments, igneous felsic rocks, etc.) during >3.1 Ga orogenic events. .

6.3 On the isotopic homogeneity of the GMS granitoids

The large size of the GMS batholiths, in addition to the petrological evidence presented above, strongly suggests a composite source for these rocks with different rock types melting. The low-Ca granitoids, that form the bulk of the Suite, are interpreted as melting of (felsic) crustal lithologies. In contrast, the dark granitoids and, probably, the syenites formed by melting of mantle (metasomatized by crustal additions). The isotopic evidence is apparently at odds with this conclusion. Thus, a process generating a range of petrologically distinct, but isotopically identical sources is required. The problem is actually slightly different at the crust, or lithosphere scale (Figure 12).

At the scale of the lithosphere, we have a range of magmas, from different sources (crust or mantle) that nevertheless have a similar isotopic signature. A similar situation has been described in several post-orogenic settings (Couzinié et al., 2016; Laurent and Zeh, 2015; Payne et al., 2016). The key point of these settings is that the mantle that melts and contributes to the granitic magmatism has been enriched by material buried from the local crust. Thus, the Hf in both the crust and mantle-derived magmas ultimately has the same source and the same characteristics.

At the scale of the crust, the problem is less severe. In fact, it is geologically unrealistic to imagine that rocks with the exact same isotopic features existed over several tens or hundreds of square kilometres. Thus, some process of intracrustal isotopic homogenization must take place. This interpretation is supported by the facts that all GMS granites (a) have the same isotopic composition; (b) were emplaced over the same, relatively short time interval, and (c) fit on the same crust evolutionary trend as TTGs and granites of the BGGT and Swaziland younger than 3400 Ma, as well as sediments from the Fig-Tree and Moodies Groups (but not pre-3400 Ma rocks)(Figure 9). The last point suggests that Hf isotope homogenization occurred within the deep to middle crust either prior to, or during GMS granitoid formation at ca. 3100 Ma. Lower- to mid-crust homogenization is further supported by similar Hf isotopic compositions of granitoids with ages of ca. 2700 Ma, which fall on the same crustal evolutionary trend as the GMS granites (Figure 9a). Hafnium isotope homogenization perhaps was achieved by percolation of melts and hydrous fluids in the deep hot crust (Kröner et al., 2018). Fluid and melt circulation allows the dissolution of the original zircon populations (magmatic or detrital), followed by Zr-Hf-transport, and Hf isotope homogenization, prior to new zircon precipitation (Zeh et al., 2015; Zeh et al., 2020). Evidence for Hf isotope homogenization during amphibolite-facies metamorphism in the middle/lower crust of the AGC is reflected by the metamorphic zircon grains found in rocks of the Dwalile GSB (van Schijndel et al., 2017).

The homogenization process in the middle crust provides insight into a poorly understood aspect of Archaean geology, namely the incorporation of igneous rocks of the TTG suite into complex Grey Gneisses.

Here, we emphasize the difference between “TTGs” and “Grey Gneisses”. TTGs are igneous plutonic rocks. Grey Gneisses, on the other hand, are complex units that have long been identified as forming the bulk of the Archaean crust (Hunter, 1970; Salop and Scheinmann, 1969). Grey Gneisses commonly include (meta-)TTG components, possibly formed during several plutonic phases – in some cases hundreds of million years apart (Kröner et al., 1999; Laurent et al., 2019). They also include a range of other lithologies such as amphibolites or occasionally metasediments. All these rocks have been tectonically interleaved, deformed, transposed, metamorphosed and often partially molten in the middle or lower crust (Kröner et al., 2019; Kröner et al., 2014; Kröner et al., 2018; Laurent et al., 2019; Taylor et al., 2013; Taylor et al., 2020). In the Kaapvaal Craton, Grey Gneisses correspond e.g. to the Ancient Gneiss Complex of Swaziland (Hunter, 1970; Kröner et al., 2019), or the dominant rock type in the Northern Kaapvaal (Laurent et al., 2019). The processes by which TTG plutons are incorporated in Grey Gneiss complexes are not elucidated, but at least require deformation and burial.

Returning to the GMS suite, it is proposed that these granitoids are the product of melting of Grey Gneisses – but not of TTGs.

6.4 Crustal stabilization in the Archaean

The GMS granitoids were emplaced at a key period in the evolution of the central portion of the Kaapvaal craton (i.e. south the the Thabazimbi-Murchsion Lineament, TML: de Wit et al., 1992). They immediately follow (and conclude) a period of "permobile" regime, with the formation of classical granite-greenstone terrain, important (TTG) magmatism, metamorphism and deformation of the crust. Ca. 3.1 Ga ages actually occur throughout the craton (e.g. Poujol et al., 2003), evidencing a craton-wide process.

After the emplacement of the GMS suite, however, the geological activity in the Kaapvaal craton in general and in Barberton in particular changes radically. The first, large intracratonic sediment accumulations (Pongola supergroup at ca. 2.95 Ga; Wilson and Zeh, 2018) cover the craton shortly after this episode, and further geological evolution in the Central Kaapvaal craton has a different character – localized, brittle intrusions of mafic rocks (Klausen et al., 2010) and "late" granitoids (Meyer et al., 1994; Robb et al., 2006). The now rigid proto-Kaapvaal Craton acts as a rigid nucleus against which late-Archaean mobile belts in the North (Laurent et al., 2019; Vézinet et al., 2018) and West (Schmitz et al., 2004) are accreted.

The geochemistry of the GMS suite shows that the process of craton stabilization involved the lithosphere as whole (mantle as well as crust), and that this lithosphere had to be primed by a pre-existing history, evident in the study area by events at ca. 3.2 Ga (Schoene et al., 2008; Schoene et al., 2009). The purpose of this paper is not to comment on the controversy relating to the ca. 3.2 Ga geodynamics of the BGGT. From a purely petrological point of view the subsequent formation of the ca. 3.1 Ga GMS suite requires (i) the formation of an enriched lithospheric mantle, and (ii) the formation of composite Grey Gneisses in which diverse components are juxtaposed and partially equilibrated and homogenized. The melting of this lithosphere permits the formation of the GMS suite as a whole. In a sense, this is reminiscent of post-orogenic granite-forming environments (Bonin, 2004; Moyen et al., 2017), although this should not necessarily be taken as evidence for a modern-looking plate tectonic environment (Moyen and Laurent, 2018), as the requirements are merely the existence of a composite crust, and burial of crustal material in the mantle.

A key difference with modern settings is the timespan between the ca 3.2 Ga events and the formation of the GMS suite at 3.11 Ga. Whereas in modern orogenic belts collision and post-collision are separated by a few millions to tens of million years, with the two stages blurring into each other, here the two events are 100 Ma apart and very few ages are recorded between the two peaks: some

minor felsic dykes as well as the Dalmein pluton (Kamo and Davis, 1994; Lana et al., 2010; Zeh et al., 2009). In the GMS suite, rare zircon xenocrysts also record magmatic activity pre-3110 Ma. Unpublished data by Murphy (2015)(Figure 13) also suggest that a moderate igneous activity may have taken place from ca. 3.2 to ca. 3.1 Ga (Figure 13). Finally, there are some hints (Lana et al., 2011) that the Pigg's Peak Batholith in Swaziland also accreted over a long period of time between 3.2 and 3.1 Ga. If confirmed, this information would put the GMS suite in a new light, as the culmination of a long-lived history, itself the aftermath of the major ca. 3.2 Ga crustal accretion event. Thus, it appears that the BGGT crust was primed by the ca. 3.2 Ga evolution, then slowly matured until ca. 3.1 Ga, at which point massive amounts of melt were generated in, or extracted from the mid- to lower crust, likely triggered by processes in the mantle. This succession of events resulted in the formation of a very stiff, stable lithosphere that became the core of the Kaapvaal craton proper.

We further speculate that this process is a common occurrence in Archaean cratons. In several Grey Gneiss units, long-lived magmatic activity has been reported (Laurent et al., 2019; Taylor et al., 2020). This continuous or near continuous activity in deep crustal levels seems to contrast with the sharp peaks observed in granitoids emplaced in the upper crust. However, the latter age distribution corresponds to crystallization of granitic magmas in large batholiths, whereas the former reflects formation of small melt volumes. Integrated over the whole crust, the process may then be one of slow formation and accumulation of melt in the source regions, followed by brutal extraction and quick emplacement at upper crustal levels (Bons et al., 2004; Vanderhaeghe and Teyssier, 2001).

7. Conclusion

This study investigates the way the Archean lithosphere stabilizes and forms cratons, and sheds light on the evolution from early TTG-greenstone crust to more stable cratonic crust. The Archean protocrust consists of lavas and minor sediments in greenstone belts, intruded by TTG plutons. Whereas the petrological processes to form it have been studied and are reasonably well understood, this protocrust is not strong enough to permit the deposition of large clastic units and the injection of dense dyke swarms (Cawood et al., 2018).

Here, we uncover some of the processes that mature the protocrust into cratonic crust. The formation of a stable continental mass requires firstly the formation of meso-crustal Grey Gneiss complexes. Grey Gneisses are composite units. They include a significant portion of meta-TTG, but they also include meta-sediments, mafic rocks, melts, etc. Furthermore, they underwent a degree of homogenization through both mechanical (tectonic interlayering) and chemical (fluid percolation,

dissolution/crystallisation, diffusion) processes. Another necessary ingredient appears to be the burial of some of the crustal material into the mantle, to form an enriched mantle source (although one sharing its isotopic characteristics with the overlying crust). In the BGGT, this is the result of the ca. 3.2 Ga geological processes.

Subsequently, all portions of this lithosphere or proto-lithosphere melt, resulting in the formation of large, composite plutonic units with a diversity of compositions, in a situation reminiscent to what is observed in present-day post-orogenic domains. Crucially, this also permits scavenging of incompatible heat producing elements, which are carried closer to the surface, leaving behind a refractory, cold residue that has little potential for future reworking and forms the lower crustal nucleus of the stable cratonic lithosphere.

Acknowledgments

This publication has been long overdue, as it is based on data acquired many years ago. It would have been an honour and a pleasure to discuss our findings with Alfred Kröner, who in addition of being a great geochronologist, was also extremely knowledgeable on the geology of the BGGT – a place very close to his heart, and where he conducted field work until his last days. Unfortunately we left the opportunity slip, and the best we can do now is to offer our contribution to this Special Issue commemorating his achievements. We thank L. Robb and J. Payne for helpful and constructive reviews.

This work has been financially supported by several CNRS/INSU grants (PNP and CESSUR). JFM's stay at Monash is supported by the Australian Research Council grant FL160100168. This is IRP BuCoMo contribution A6 (2020).

Data Availability

Datasets related to this article can be found at http://dx.doi.org/this/article, an open-source online data repository hosted at Mendeley Data (Moyen et al, 202X).

Item DR1: Whole rock analyses of granitoids from the GMS suite, compiled from this work as well as from the literature.

Item DR2: U-Pb analyses in zircon grains from the GMS suite and the Theespruit formation.

Item DR3: Lu-Hf analyses in zircon grains from the GMS suite and the Theespruit formation.

References

Anhaeusser, C.R., Robb, L.J., 1983a. Chemical analyses of granitoid rocks from the Barberton Mountain Land. Geological Society of South Africa Special Publication 9, 189-219.

Anhaeusser, C.R., Robb, L.J., 1983b. Geological and geochemical characteristics of the Heeenveen and Mpuluzi batholiths south of the Barberton greenstone belt, and premliminary thoughts on their petrogenesis, Contributions to the geology of the Barberton Mountain land. Geological Society of South Africa, pp. 131-151.

Anhaeusser, C.R., Robb, L.J., Barton, J.M., Jr, 1983. Mineralogy, petrology and origin of the Boesmanskop syeno-granite complex, Barberton mountain land, South Africa, Geological Society of South Africa Special Publication, pp. 169-183.

Anhaeusser, C.R., Robb, L.J., Viljoen, M.J., 1981. Provisonnal geological map of the Barberton greenstone belt and surrounding granitic terrane, eastern Transvaal and Swaziland (1:250 000), Geological Society of South Africa Special Publication. Geological Society of South Africa.

Bachmann, O., Bergantz, G.W., 2004. On the origin of crystal-poor rhyolites: extracted from batholithic crystal mushes. J. Petrol. 45, 1565.

Barbarin, B., 2005. Mafic magmatic enclaves and mafic rocks associated with some granitoids of the central Sierra Nevada batholith, California: nature, origin, and relations with the hosts. Lithos 80, 155-177.

Belcher, R.W., Kisters, A.F.M., 2006a. Progressive adjustments of ascent and emplacement controls during incremental construction of the 3.1 Ga Heerenveen batholith, South Africa. J. Struct. Geol. 28, 1406-1421.

Belcher, R.W., Kisters, A.F.M., 2006b. Syntectonic emplacement and deformation of the Heerenveen batholith: conjectures on the structural setting of the 3.1 Ga granite magmatism in the Barberton granite-greenstone terrain, South Africa. Geological society of America special Publication 405, 211-231.

Bibikova, E., Arestova, N., Ivanikov, V., Claesson, S., Petrova, A.Y., Levchenkov, O., 2006. Isotopic geochronology of the archean posttectonic association of sanukitoids, syenites, and granitoids in central Karelia. Petrology 14, 39-49.

Blichert-Toft, J., Puchtel, I.S., 2010. Depleted mantle sources through time: evidence from Lu–Hf and Sm–Nd isotope systematics of Archean komatiites. Earth Planet. Sci. Lett. 297, 598-606.

Bonin, B., 2004. Do coeval mafic and felsic magmas in post-collisional to within-plate regimes necessarily imply two contrasting, mantle and crustal, sources? A review. Lithos 78.

Bonin, B., Janousek, V., Moyen, J.F., 2020. Chemical variation, modal composition and classification of granitoids, in: Janousek, V., Bonin, B., Collins, W.J., Farina, F., Bowden, P. (Eds.), Post-Archean Granitic Rocks: Petrogenetic Processes and Tectonic Environments. Geological Society of London, pp. 9-51.

Bons, P., Arnold, J., Elburg, M., Kalda, J., Soesoo, A., van Miligen, B.P., 2004. Melt extraction and accumulation from partially molten rocks. Lithos 78, 25-42.

Bouvier, A., Vervoort, J.D., Patchett, P.J., 2008. The Lu-Hf and Sm-Nd isotopic composition of CHUR: Constraints from unequilibrated chondrites and implications for the bulk composition of terrestrial planets. Earth Planet. Sci. Lett. 273, 48-57.

Byerly, G.R., Kroner, A., Lowe, D.R., Todt, W., Walsh, M.M., 1996. Prolonged magmatism and time constraints for sediment deposition in the early Archean Barberton greenstone belt: Evidence from the Upper Onverwacht and Fig Tree groups. Precambr Res. 78, 125-138.

Capitanio, F., Nebel, O., Cawood, P., Weinberg, R., Clos, F., 2019. Lithosphere differentiation in the early Earth controls Archean tectonics. Earth Planet. Sci. Lett. 525, 115755.

Cawood, P.A., Hawkesworth, C.J., Pisarevsky, S.A., Dhuime, B., Capitanio, F.A., Nebel, O., 2018. Geological archive of the onset of plate tectonics. Philosophical Transactions of the Royal Society A: Mathematical, Physical and Engineering Sciences 376, 20170405.

Champion, D.C., Sheraton, J.W., 1997. Geochemistry and Nd isotope systematics of Archaean of the Eastern Goldfields, Yilgarn Craton, Australia: implications for crustal growth processes. Precambr Res. 83.

Chowdhury, P., Chakraborty, S., Gerya, T.V., Cawood, P.A., Capitanio, F.A., 2020. Peel-back controlled lithospheric convergence explains the secular transitions in Archean metamorphism and magmatism. Earth Planet. Sci. Lett. 538, 116224.

Clemens, J.D., Belcher, R.W., Kisters, A.F.M., 2010. The Heerenveen Batholith, Barberton Mountain Land, South Africa: Mesoarchaean, Potassic, Felsic Magmas Formed by Melting of an Ancient Subduction Complex. J. Petrol. 51, 1099.

Clemens, J.D., Helps, P.A., Stevens, G., 2009. Chemical structure in granitic magmas - a signal from the source? Transactions of the Royal Society of Edinburgh-Earth Sciences 100, 159-172.

Cornwright, M.S., Robb, L.J., Bosch, P.J.A., 2008. The Geology of Witriver area, 1/50 000 Geological maps. Council for Geosciences, South Africa, Pretoria.

Coryell, C.D., Chase, J.W., Winchester, J.W., 1963. A procedure for geochemical interpretation of terrestrial rare-earth abundance patterns. J. Geophys. Res. 68, 559-566.
Couzinié, S., Moyen, J.F., Laurent, O., Zeh, A., Bouilhol, P., Villaros, A., Gardien, V., 2016. Post-collisional magmatism: Crustal growth not identified by zircon Hf–O isotopes. Earth Planet. Sci. Lett. 456, 182-195.
Creaser, R.A., Price, R.C., Wormald, R.J., 1991. A-type granites revisited: assessment of a residual-source model. Geology 19, 163-166.
Cuney, M., Friedrich, M., Blumenfield, P., Bourguignon, A., Boiron, M., Vigneresse, J.L., Poty, B., 1989. Metallogenesis in the French part of the Variscan orogen. Part I: U-preconcentrations in the pre-Variscan and Variscan formations:A comparison with Sn, W and Au. Tectonophysics 177, 39-57.
Cutts, K.A., Stevens, G., Hoffmann, J.E., Buick, I.S., Frei, D., Münker, C., 2014. Paleo- to Mesoarchean polymetamorphism in the Barberton Granite-Greenstone Belt, South Africa: Constraints from U-Pb monazite and Lu-Hf garnet geochronology on the tectonic processes that shaped the belt. Geol. Soc. Am. Bull., online 13/12/2013.
de Vries, S.T., Nijman, W., Armstrong, R.A., 2006. Growth-fault structure and stratigraphic architecture of the Buck Ridge volcano-sedimentary complex, upper Hooggenoeg formation, Barberton Greenstone Belt, South Africa. Precambr Res. 149, 77-98.
de Wit, M.J., Roering, C., Hart, R.J., Armstrong, R.A., de Ronde, C.E.J., Green, R.W.E., Tredoux, M., Peberdy, E., Hart, R.A., 1992. Formation of an Archaean continent. Nature 357, 553-562.
Debon, F., Lefort, P., 1983. A chemical–mineralogical classification of common plutonic rocks and associations. Transactions of the Royal Society of Edinburgh: Earth Sciences 73.
Diener, J., Stevens, G., Kisters, A.F.M., Poujol, M., 2005. Metamorphism and exhumation of the basal parts of the Barberton greenstone belt, South Africa: Constraining the rates of mid-Archaean tectonism. Precambr Res. 143, 87-112.
Diener, J.F.A., Dziggel, A., in press. Can mineral equilibria modelling provide additional details on metamorphism of the Barberton garnet amphibolites? South African Journal of Geology.
Dziggel, A., Armstrong, R.A., Stevens, G., Nasdala, L., 2005. Growth of zircon and titanite during metamorphism in the granitoid-gneiss terrain south of the Barberton greenstone belt, South Africa. Mineral. Mag. 69, 1021-1038.
Dziggel, A., Poujol, M., Otto, A., Kisters, A.F.M., Trieloff, M., Schwarz, W.H., Meyer, F.M., 2010. New U-Pb and 40Ar/39Ar ages from the northern margin of the Barberton greenstone belt, South Africa: Implications for the formation of Mesoarchaean gold deposits. Precambr Res. 179, 206-220.
Dziggel, A., Stevens, G., Poujol, M., Anhaeusser, C.R., Armstrong, R.A., 2002. Metamorphism of the granite-greenstone terrane South of the Barberton greenstone belt, South Africa: an insight into the tectono-thermal evolution of the 'lower' portions of the Onverwacht group. Precambr Res. 114, 221-247.
Fayol, N., Jébrak, M., 2017. Archean sanukitoid gold porphyry deposits: A new understanding and genetic model from the Lac Bachelor gold deposit, Abitibi, Canada. Econ. Geol. 112, 1913-1936.
Friedrich, M., Cuney, M., Poty, B., 1987. Uranium geochemistry in peraluminous leucogranites. Uranium 3.
Frost, B.R., Barnes, C.G., Collins, W.J., Arculus, R.J., Ellis, D.J., Frost, C.D., 2001. A geochemical classification for granitic rocks. J. Petrol. 42, 2033-2048.
Gerdes, A., Zeh, A., 2006. Combined U–Pb and Hf isotope LA-(MC-)ICP-MS analyses of detrital zircons: Comparison with SHRIMP and new constraints for the provenance and age of an Armorican metasediment in Central Germany. Earth Planet. Sci. Lett. 249, 47-61.
Gerdes, A., Zeh, A., 2009. Zircon formation versus zircon alteration—new insights from combined U–Pb and Lu–Hf in-situ LA-ICP-MS analyses, and consequences for the interpretation of Archean zircon from the Central Zone of the Limpopo Belt. Chem. Geol. 261, 230-243.
Harris, N., Duyverman, H., Almond, D., 1983. The trace element and isotope geochemistry of the Sabaloka igneous complex, Sudan. J. Geol. Soc. 140, 245-256.
Heilimo, E., Halla, J., Mikkola, P., 2012. Overview of Neoarchaean sanukitoid series in the Karelia Province, eastern Finland. Geological Survey of Finland, Special Papers 54, 214-225.

Heubeck, C., Engelhardt, J., Byerly, G.R., Zeh, A., Sell, B., Luber, T., Lowe, D.R., 2013. Timing of deposition and deformation of the Moodies Group (Barberton Greenstone Belt, South Africa): Very-high-resolution of Archaean surface processes. Precambr Res. 231, 236-262.

Hoffmann, J., Kröner, A., 2018. Early Archaean crustal evolution in southern Africa—an updated record of the Ancient Gneiss Complex of Swaziland. Earth's oldest rocks, 2nd edn. Elsevier, Amsterdam, 553-567.

Hoffmann, J.E., Wilson, A.H., 2017. The origin of highly radiogenic Hf isotope compositions in 3.33 Ga Commondale komatiite lavas (South Africa). Chem. Geol. 455, 6-21.

Hoffmann, J.E., Zhang, C., Moyen, J.-F., Nagel, T.J., 2018. The formation of tonalites-trondjhemites-granodiorites and of the early continental crust in: Van Kranendonk, M., Bennett, V., Hoffmann, J.E. (Eds.), Earth Oldest Rocks, 2nd ed. Elsevier, pp. 133-168.

Hofmann, A., Anhaeusser, C.R., Dixon, J., Kröner, A., Saha, L., Wilson, A., Xie, H., 2019. Archaean Granitoid–Greenstone Geology of the Southeastern Part of the Kaapvaal Craton, The Archaean Geology of the Kaapvaal Craton, Southern Africa. Springer, pp. 33-54.

Hunter, D.R., 1970. The Ancient gneiss complex in Swaziland. Trans. Geol. Soc. S. Afr. 73, 107-150.

Hunter, D.R., Barker, F., Millard, H.T., 1978. The geochemical nature of the Archaean Ancient Gneiss Complex and Granodiorite Suite, Swaziland: a preliminary study. Precambr Res. 7, 105-127.

Jackson, S.E., Pearson, N.J., Griffin, W.L., Belousova, E.A., 2004. The application of laser ablation-inductively coupled plasma-mass spectrometry to in situ U–Pb zircon geochronology. Chem. Geol. 211, 47-69.

Janoušek, V., Konopásek, J., Ulrich, S., Erban, V., Taj manová, L., Jerabek, P., 2010. Geochemical character and petrogenesis of Pan-African Amspoort suite of the Boundary Igneous Complex in the Kaoko Belt (NW Namibia). Gondwana Res. 18, 688-707.

Janoušek, V., Moyen, J.F., Martin, H., Erban, V., Farrow, C.M., 2016. Geochemical Modelling of Igneous Processes—Principles and Recipes in the R Language. Springer Verlag, Berlin.

Kamo, S.L., Davis, D.W., 1994. Reassessment of Archean Crustal Development in the Barberton Mountain Land, South-Africa, Based on U-Pb Dating. Tectonics 13, 167-192.

Klausen, M., Söderlund, U., Olsson, J., Ernst, R., Armoogam, M., Mkhize, S., Petzer, G., 2010. Petrological discrimination among Precambrian dyke swarms: eastern Kaapvaal craton (South Africa). Precambr Res. 183, 501-522.

Kleinhanns, I.C., Kramers, J.D., Kamber, B.S., 2003. Importance of water for Archaean granitoid petrology: a comparative study of TTG and potassic granitoids from Barberton Mountain Land, South Africa. Contribution to Mineralogy and Petrology 145, 377-389.

Konopásek, J., Janoušek, V., Oyhantçabal, P., Sláma, J., Ulrich, S., 2018. Did the circum-Rodinia subduction trigger the Neoproterozoic rifting along the Congo–Kalahari Craton margin? Int. J. Earth Sci. 107, 1859-1894.

Kröner, A., Anhaeusser, C., Hoffmann, J., Wong, J., Geng, H., Hegner, E., Xie, H., Yang, J., Liu, D., 2016. Chronology of the oldest supracrustal sequences in the Palaeoarchaean Barberton Greenstone Belt, South Africa and Swaziland. Precambr Res. 279, 123-143.

Kröner, A., Hegner, E., Wendt, J.I., Byerly, G.R., 1996. The oldest part of the Barberton granitoid-greenstone terrain, South Africa: evidence for crust formation between 3.5 and 3.7 Ga. Precambr Res. 78, 105-124.

Kröner, A., Hoffmann, J.E., Wong, J.M., Geng, H.-Y., Schneider, K.P., Xie, H., Yang, J.-H., Nhleko, N., 2019. Archaean crystalline rocks of the Eastern Kaapvaal Craton, The Archaean Geology of the Kaapvaal Craton, Southern Africa. Springer, pp. 1-32.

Kröner, A., Hoffmann, J.E., Xie, H., Münker, C., Hegner, E., Wan, Y., Hofmann, A., Liu, D., Yang, J., 2014. Generation of early Archaean grey gneisses through melting of older crust in the eastern Kaapvaal craton, southern Africa. Precambr Res. 255, 823-846.

Kröner, A., Jaeckel, P., Brandl, G., Nemchin, A., Pidgeon, R., 1999. Single zircon ages for granitoid gneisses in the Central Zone of the Limpopo belt, Souther Africa and geodynamic significance. Precambr Res. 93, 299-337.

Kröner, A., Nagel, T.J., Hoffmann, J.E., Liu, X., Wong, J., Hegner, E., Xie, H., Kasper, U., Hofmann, A., Liu, D., 2018. High-temperature metamorphism and crustal melting at ca. 3.2 Ga in the eastern Kaapvaal craton, southern Africa. Precambr Res. 317, 101-116.

Kröner, A., Tegtmeyer, A.R., 1994. Gneiss-greenstone relationships in the Ancient Gneiss Complex of Southwestern Swaziland, southern Africa, and implications for early crustal evolution. Precambr Res. 67, 109-139.

Lana, C., Buick, I., Stevens, G., Rossouw, R., De Wet, W., 2011. 3230–3200 Ma post-orogenic extension and mid-crustal magmatism along the southeastern margin of the Barberton Greenstone Belt, South Africa. J. Struct. Geol. 33, 844-858.

Lana, C., Tohver, E., Cawood, P., 2010. Quantifying rates of dome-and-keel formation in the Barberton granitoid-greenstone belt, South Africa. Precambr Res. 177, 199-211.

Laurent, O., Björnsen, J., Wotzlaw, J.-F., Bretscher, S., Pimenta Silva, M., Moyen, J.F., Ulmer, P., Bachmann, O., 2020. Earth's earliest granitoids are crystal-rich magma reservoirs tapped by silicic eruptions. Nat. Geosci.

Laurent, O., Martin, H., Moyen, J.-F., Doucelance, R., 2014a. The diversity and evolution of late-Archaean granitoids: evidence for the onset of "modern-style" plate tectonics between 3.0 and 2.5 Ga. Lithos 205, 208-235.

Laurent, O., Rapopo, M., Stevens, G., Moyen, J.-F., Martin, H., Doucelance, R., Bosq, C., 2014b. Contrasting petrogenesis of Mg-K and Fe-K granitoids and implications for postcollisional magmatism: case study from the late-Archaean Matok pluton (Pietersburg block, South Africa). Lithos 196-197, 131-149.

Laurent, O., Zeh, A., 2015. A linear Hf isotope-age array despite different granitoid sources and complex Archean geodynamics: Example from the Pietersburg block (South Africa). Earth Planet. Sci. Lett. 430, 326-338.

Laurent, O., Zeh, A., Brandl, G., Vézinet, A., Wilson, A., 2019. Granitoids and Greenstone Belts of the Pietersburg Block—Witnesses of an Archaean Accretionary Orogen Along the Northern Edge of the Kaapvaal Craton, in: A., K., A., H. (Eds.), The Archaean Geology of the Kaapvaal Craton, Southern Africa. Springer.

Lobach-Zhuchenko, S.B., Rollinson, H.R., Chekulaev, V.P., Savatenkov, V., Kovalenko, A., Martin, H., Guseva, N.S., Arestova, N.A., 2008. Petrology of a Late Archaean, Highly Potassic, Sanukitoid Pluton from the Baltic Shield: Insights into Late Archaean Mantle Metasomatism. J. Petrol. 49, 393-420.

Lowe, D., Byerly, G., Heubeck, C., 2012. Geologic Map of the west-central Barberton Greenstone Belt, South Africa, Scale 1: 25,000. Geological Society of America Map and Chart Series.

Lowe, D.R., Byerly, G.R., 2007. An overview of the geology of the Barberton greenstone belt and vicinity: implications for early crustal development, in: Van Kranendonk, M.J., Smithies, R.H., Bennett, V. (Eds.), Earth's Oldest Rocks. Elsevier, pp. 481-526.

Ludwig, K., 2001. Isoplot/Ex: a geochronological toolkit for Microsoft Excel. Berkeley Geochronological Center Special Publication, 43.

Marsh, J.S., 2006. The Dominion group, The Geology of South Africa. Council for Geoscience, Pretoria, pp. 149-154.

Martin, H., 1986. Effect of steeper Archean geothermal gradient on geochemistry of subduction-zone magmas. Geology 14, 753-756.

Martin, H., Moyen, J.-F., Rapp, R., 2010. Sanukitoids and the Archaean-Proterozoic boundary. Transactions of the Royal Society of Edinburgh-Earth Sciences 100, 15-33.

Masuda, A., 1957. Simple regularity in the variation of relative abundances of rare earth elements. Journal of Earth Sciences Nagoya University 5, 125-134.

Masuda, A., 1962. Regularities in variation of relative abundances of lanthanide elements and an attempt to analyse separation-index patterns of some materials. Journal of Earth Sciences Nagoya University 10, 173-187.

Meyer, F.M., Robb, L.J., Reimold, W.U., de Bruiyn, H., 1994. Contrasting low and high-Ca plutons in the Barberton Mountain Land, southern Africa. Lithos 32, 63-76.

Minster, J., Allègre, C., 1978. Systematic use of trace elements in igneous processes. Part III: Inverse problem of batch partial melting in volcanic suites. Contrib. Mineral. Petrol. 68, 37-52.
Moyen, J.-F., 2009. High Sr/Y and La/Yb ratios: The meaning of the "adakitic signature". Lithos 112, 556-574.
Moyen, J.-F., Carrouée, S., Cuney, M., Baratoux, D., Sardini, P., in press. Multi-scale spatial distribution of elements in an Archaean potassic granite: a case study from the Heerenveen batholith, Barberton granite-greenstone terrain. S. Afr. J. Geol.
Moyen, J.-F., Laurent, O., 2018. Archaean tectonic systems: a view from igneous rocks. Lithos 302-303, 99-125.
Moyen, J.-F., Stevens, G., 2006. Experimental constraints on TTG petrogenesis: implications for Archean geodynamics, in: Benn, K., Mareschal, J.-C., Condie, K.C. (Eds.), Archean geodynamics and environments. AGU, pp. 149-178.
Moyen, J.-F., Stevens, G., Kisters, A.F.M., 2006. Record of mid-Archaean subduction from metamorphism in the Barberton terrain, South Africa. Nature 443, 559-562.
Moyen, J.-F., Stevens, G., Kisters, A.F.M., Belcher, R.W., Lemirre, B., 2018. TTG plutons of the Barberton granitoid-greenstone terrain, South Africa, in: Van Kranendonk, M., Bennett, V., Hoffmann, J.E. (Eds.), Earth Oldest Rocks, 2nd ed. Elsevier, pp. 615-654.
Moyen, J.F., 2019. Archaean granitoids: classification, petrology, geochemistry and origin, in: Dey, S., Moyen, J.F. (Eds.), Archean Granitoids of India: Windows into Early Earth Tectonics. Geological Society of London.
Moyen, J.F., Laurent, O., Chelle-Michou, C., Couzinié, S., Vanderhaeghe, O., Zeh, A., Villaros, A., Gardien, V., 2017. Collision vs. subduction-related magmatism: two contrasting ways of granite formation and implications for crustal growth. Lithos 277, 154-177.
Moyen, J.F., Martin, H., 2012. Forty years of TTG research. Lithos 148, 312-336.
Mühlberg, M., Stevens, G., Moyen, J.-F., Kisters, A.F.M., Lana, C., in revision. Thermal evolution of the Stolzburg Block, Barberton granitoid-greenstone terrain, South Africa: Implications for Paleoarchean tectonic processes. Precambr Res.
Murphy, R., 2015. Stabilising a Craton: The Origin and Emplacement of the 3.1 Ga Mpuluzi Batholith. Maquarie University,, Sydney, p. 489.
Nebel, O., Campbell, I.H., Sossi, P.A., Van Kranendonk, M.J., 2014. Hafnium and iron isotopes in early Archean komatiites record a plume-driven convection cycle in the Hadean Earth. Earth Planet. Sci. Lett. 397, 111-120.
Nebel, O., Capitanio, F., Moyen, J.F., Weinberg, R., Clos, F., Nebel-Jacobsen, Y., Cawood, P.A., 2018. When crust comes of age: on the chemical evolution of Archaean, felsic continental crust by crustal drip tectonics. Phil. Trans. R. Soc. London 376, 20180103.
Payne, J.L., McInerney, D.J., Barovich, K.M., Kirkland, C.L., Pearson, N.J., Hand, M., 2016. Strengths and limitations of zircon Lu-Hf and O isotopes in modelling crustal growth. Lithos 248, 175-192.
Pearson, D., Wittig, N., 2014. The formation and evolution of cratonic mantle lithosphere: Evidence from mantle xenoliths. Treatise on Geochemistry 2, 255-292.
Poujol, M., Robb, L.J., Anhaeusser, C.R., Gericke, B., 2003. A review of the geochronological constraints on the evolution of the Kaapvaal craton, South Africa. Precambr Res. 127, 181-213.
Robb, L., Brandl, G., Anhaeusser, C., Poujol, M., 2006. Archaean granitoid intrusions. The Geology of South Africa, 57-94.
Robb, L.J., 1983. Trace element trends in granites and the distinction between partial melting and crystal fractionation processes: case studies from two granites in southern Africa., in: Augustithis, S.S. (Ed.), The significance of trace elements in solving petrogenetic problems. Theophrastus Publications, pp. 279-294.
Robb, L.J., Anhaeusser, C.R., Van Nierop, D.A., 1983. The recognition of the Nelspruit batholith north of the Barberton greenstone belt and its significance in terms of Archaean crustal evolution, pp. 117-130.
Salop, L.I., Scheinmann, Y.M., 1969. Tectonic history and structure of plateforms and shields. Tectonophysics 7, 565-597.

Scherer, E., Münker, C., Mezger, K., 2001. Calibration of the lutetium-hafnium clock. Science 293, 683-687.
Schiano, P., Allègre, C.J., Dupré, B., Lewin, E., Joron, J.-L., 1993. Variability of trace elements in basaltic suites. Earth Planet. Sci. Lett. 119, 37-51.
Schmitz, M.D., Bowring, S.A., de Wit, M.J., Gartz, V., 2004. Subduction and terrane collision stabilize the western Kaapvaal craton tectosphere 2.9 billion years ago. Earth Planet. Sci. Lett. 222, 363-376.
Schneider, K., Hoffmann, J., Münker, C., Patyniak, M., Sprung, P., Roerdink, D., Garbe-Schönberg, D., Kröner, A., 2019. Petrogenetic evolution of metabasalts and metakomatiites of the lower Onverwacht Group, Barberton Greenstone Belt (South Africa). Chem. Geol. 511, 152-177.
Schoene, B., Bowring, S.A., 2010. Rates and mechanisms of Mesoarchean magmatic arc construction, eastern Kaapvaal craton, Swaziland. Geol. Soc. Am. Bull. 122, 408-429.
Schoene, B., De Wit, M., Bowring, S.A., 2008. Mesoarchean assembly and stabilization of the eastern Kaapvaal craton: A structural-thermochronological perspective. Tectonics 27, TC5010.
Schoene, B., Dudas, F.O.L., Bowring, S.A., De Wit, M., 2009. Sm-Nd isotopic mappig of lithospheric growth and stabilization in the eastern Kaapvaal craton. Terra Nova 21, 219-228.
Skjerlie, K.P., Johnston, A.D., 1992. Vapor-absent melting at 10 kbar of a biotite-and amphibole-bearing tonalitic gneiss: implications for the generation of A-type granites. Geology 20, 263-266.
Söderlund, U., Patchett, P.J., Vervoort, J.D., Isachsen, C.E., 2004. The 176 Lu decay constant determined by Lu–Hf and U–Pb isotope systematics of Precambrian mafic intrusions. Earth Planet. Sci. Lett. 219, 311-324.
Stacey, J.t., Kramers, J., 1975. Approximation of terrestrial lead isotope evolution by a two-stage model. Earth Planet. Sci. Lett. 26, 207-221.
Stern, R.A., Bodorkos, S., Kamo, S.L., Hickman, A.H., Corfu, F., 2009. Measurement of SIMS instrumental mass fractionation of Pb isotopes during zircon dating. Geostand. Geoanal. Res. 33, 145-168.
Stussi, J.-M., 1989. Granitoid chemistry and associated mineralization in the French Variscan. Econ. Geol. 84, 1363-1381.
Sutcliffe, R., Barrie, C.T., Burrows, D., Beakhouse, G., 1993. Plutonism in the southern Abitibi Subprovince; a tectonic and petrogenetic framework. Econ. Geol. 88, 1359-1375.
Taylor, J., Gerdes, A., Zeh, A., 2013. U-Pb, Lu-Hf and Sm-Nd Isotope Systematics during Polymetamorphism in the Ancient Gneiss Complex, Swaziland. Mineral. Mag. 77, 2316.
Taylor, J., Zeh, A., Gerdes, A., 2016. U–Pb–Hf isotope systematics of detrital zircons in high-grade paragneisses of the Ancient Gneiss Complex, Swaziland: Evidence for two periods of juvenile crust formation, Paleo-and Mesoarchaean sediment deposition, and 3.23 Ga terrane accretion. Precambr Res. 280, 205-220.
Taylor, R.J., Johnson, T.E., Clark, C., Harrison, R.J., 2020. Persistence of melt-bearing Archean lower crust for> 200 my—an example from the Lewisian Complex, northwest Scotland. Geology 48, 221-225.
Taylor, S.R., McLennan, S.M., 1985. The continental crust: its composition and evolution. Blackwell, Oxford.
Tchameni, R., Mezger, K., Nsifa, N., Pouclet, A., 2001. Crustal origin of Early Proterozoic syenites in the Congo craton (Ntem complex), South Cameroon. Lithos 57, 23-42.
Toulkeridis, T., Clauer, N., Kroner, A., Reimer, T., Todt, W., 1999. Characterization, provenance, and tectonic setting of Fig Tree greywackes from the archaean Barberton Greenstone Belt, South Africa. Sediment. Geol. 124, 113-129.
Turpin, L., Cuney, M., Friedrich, M., Bouchez, J.L., Aubertin, M., 1990. Meta-Igneous Origin of Hercynian Peraluminous Granites in Nw French Massif Central - Implications for Crustal History Reconstructions. Contrib. Mineral. Petrol. 104, 163-172.
Van Kranendonk, M., Kröner, A., Hegner, E., Connelly, J., 2009. Age, lithology and structural evolution of the c. 3.53 Ga Theespruit Formation in the Tjakastad area, southwestern Barberton Greenstone Belt, South Africa, with implications for Archaean tectonics. Chem. Geol. 261, 115-139.

Van Kranendonk, M.J., Kröner, A., Hoffmann, J.E., Nagel, T., Anhaeusser, C.R., 2014. Just another drip: Re-analysis of a proposed Mesoarchean suture from the Barberton Mountain Land, South Africa. Precambr Res. 254, 19-35.

van Schijndel, V., Stevens, G., Zeh, A., Frei, D., Lana, C., 2017. Zircon geochronology and Hf isotopes of the Dwalile Supracrustal Suite, Ancient Gneiss Complex, Swaziland: Insights into the diversity of Palaeoarchaean source rocks, depositional and metamorphic ages. Precambr Res. 295, 48-66.

Vanderhaeghe, O., Teyssier, C., 2001. Crustal-scale rheological transitions during late-orogenic collapse. Tectonophysics 335, 211-228.

Vézinet, A., Moyen, J.F., Stevens, G., Nicoli, G., Couzinié, S., 2018. A record of 0.5 Ga of evolution of the continental crust along the northern edge of the Kaapvaal craton, South Africa: consequences for the understanding of Archaean geodynamic processes. Precambr Res. 305, 310-326.

Vielzeuf, D., Montel, J.M., 1994. Partial melting of metagreyackes. Part I. Fluid-absent experiments and phase relationships. Contribution to Mineralogy and Petrology 117, 375-393.

Wang, H., Yang, J.H., Kröner, A., Zhu, Y.S., Li, R., 2019. Non-subduction origin for 3.2 Ga high-pressure metamorphic rocks in the Barberton granitoid-greenstone terrane, South Africa. Terra Nova 31, 373-380.

Watkins, J.M., Clemens, J.D., Treloar, P.J., 2007. Archaean TTGs as sources of younger granitic magmas: melting of sodic metatonalites at 0.6-1.2 GPa. Contribution to Mineralogy and Petrology 154, 91-110.

Wedepohl, K.H., 1995. The composition of the continental crust. Geochim. Cosmochim. Acta 59, 1217-1232.

Westraat, J.D., Kisters, A.F.M., Poujol, M., Stevens, G., 2004. Transcurrent shearing, granite sheeting and the incremental construction of the tabular 3.1 Ga Mpuluzi batholith, Barberton granite-greenstone terrane, South Africa. J. Geol. Soc. London 161, 1-16.

Wiedenbeck, M., Hanchar, J.M., Peck, W.H., Sylvester, P., Valley, J., Whitehouse, M., Kronz, A., Morishita, Y., Nasdala, L., Fiebig, J., 2004. Further characterisation of the 91500 zircon crystal. Geostand. Geoanal. Res. 28, 9-39.

Wilson, A., Shirey, S., Carlson, R., 2003. Archaean ultra-depleted komatiites formed by hydrous melting of cratonic mantle. Nature 423, 858-861.

Wilson, A., Zeh, A., 2018. U-Pb and Hf isotopes of detrital zircons from the Pongola Supergroup: Constraints on deposition ages, provenance and Archean evolution of the Kaapvaal craton. Precambr Res. 305, 177-196.

Windley, B.F., 1995. The Evolving continents, 3rd ed. John Wiley and sons, Chester.

Woodhead, J.D., Hergt, J.M., 2005. A preliminary appraisal of seven natural zircon reference materials for in situ Hf isotope determination. Geostand. Geoanal. Res. 29, 183-195.

Woolley, A., Jones, G., 1987. The petrochemistry of the northern part of the Chilwa alkaline province, Malawi. Geological Society, London, Special Publications 30, 335-355.

Zanvilevich, A.N., Litvinovsky, B.A., Wickham, S.M., Bea, F., 1995. Genesis of alkaline and peralkaline syenite-granite series: the Kharitonovo pluton (Transbaikalia, Russia). The Journal of Geology 103, 127-145.

Zeh, A., Gerdes, A., Barton, J.M., 2009. Archean accretion and crustal evolution of the Kalahari Craton—the zircon age and Hf isotope record of granitic rocks from Barberton/Swaziland to the Francistown Arc. J. Petrol. 50, 933.

Zeh, A., Gerdes, A., Heubeck, C., 2013. U–Pb and Hf isotope data of detrital zircons from the Barberton Greenstone Belt: constraints on provenance and Archaean crustal evolution. J. Geol. Soc. 170, 215-223.

Zeh, A., Gerdes, A., Millonig, L., 2011. Hafnium isotope record of the Ancient Gneiss Complex, Swaziland, southern Africa: evidence for Archaean crust–mantle formation and crust reworking between 3.66 and 2.73 Ga. J. Geol. Soc. 168, 953-964.

Zeh, A., Ovtcharova, M., Wilson, A.H., Schaltegger, U., 2015. The Bushveld Complex was emplaced and cooled in less than one million years–results of zirconology, and geotectonic implications. Earth Planet. Sci. Lett. 418, 103-114.

Zeh, A., Stern, R.A., Gerdes, A., 2014. The oldest zircons of Africa—Their U–Pb–Hf–O isotope and trace element systematics, and implications for Hadean to Archean crust–mantle evolution. Precambr Res. 241, 203-230.

Zeh, A., Wilson, A.H., Gudelius, D., Gerdes, A., 2020. Hafnium Isotopic Composition of the Bushveld Complex requires Mantle Melt - Upper Crust Mixing: New Evidence from Zirconology of Mafic, Felsic and Metasedimentary Rocks. J. Petrol. in press.

Figure 1. Schematic map of the BGGT, highlighting the GMS batholiths. GMS syenites: Bk: Boesmanskop; KZD: Kees Zyn Doorns. TTG units: Bpl.: Badplaas Complex; Stz.: Stolzburg Pluton.

Figure 2. Geological map of the Heerenveen batholith and adjacent portions of the Mpuluzi batholith. See Figure 1 for location. After Moyen et al. (in press). The location of the samples out of which zircons were analysed in this study is reported with coloured symbols (colour code as in Figure 4). Samples from the literature are in white symbols. W05 : (Westraat et al., 2004), samples « phon » (Boesmanskop phonolite dyke) and 586 (Mpuluzi granite). K94 : (Kamo and Davis, 1994), sample S (Mpuluzi granite) and T (Boesmanskop syenite).

Figure 3. Field photographs of the main rock types in the Southern GMS batholiths. Coloured symbols next to the photos correspond to the caption of Fig. 4. (a—d) : Heerenveen : (a). Homogeneous megacrystic granite of the core portion of the batholith, here with sub-euhedral centimeter sized grains of quartz. (b) Leucogranite II, associated with pegmatites, in the South-Eastern Shear Zone (scale bar is about 10 cm). (c). Lit par lit injection of leucogranite I into gneissic remnants (near sample HE-11-4A) in Western shear zone. (d). Pink quartz monzonite (near sample HE-11-8). (e—i) : Mpuluzi : (e). Main homogeneous megacrystic granite of the Heerenveen batholith, here with a small microgranular mafic enclave. (f). Leucogranite II (scale bar is about 1 cm). (g). Intrusive breccia of a dark Augen granodiorite (Aug) brecciating a syenogranite (SG) with early pegmatites (Peg). Scale bar is about 1 m. (h). Augen granodiorite. (i). Syenogranite. Photos f—i come from a large outcrop (the Eagle High locality) mapped in details by Sonke (2006), C. Campbell and A. Kisters (unpub), further described in Moyen et al. in press, and from which samples MP-11-2 (syenogranite), MP-11-3 (Augen granodiorite) and MP-12-01 (pegmatite) were taken. (j—k) : Boesmanskop : (j). Coarse grained syenite. (k). Hypovolcanic dyke (equivalent to sample phon of Westraat et al. 2004).

Figure 4. Major-elements geochemical features of the GMS batholiths of the Southern BGGT. Colours reflect the different chemical types (and field-based facies), and symbols the different intrusions. Samples studied for U—Pb—Hf in zircon are shown as larger symbols. (a) P—Q (cationic) diagram of (Debon and Lefort, 1983). (b) SiO_2 – MALI (weight) diagram of (Frost et al., 2001). (c) A/CNK vs. A/NK diagram of (Shand, 1943). A/CNK = molecular Al/ 2Ca + Na + K and A/NK = molecular Al/Na+K (or equivalent oxide-based formulations). (d) B—A (cationic) diagram of Debon and Lefort (1983). (e) B – mg# diagram of Debon an Lefort (1983), mg# = (cationic) Mg/(Mg+Fe). (f). SiO_2 – K_2O (weight) diagram, with lines corresponding to the series defined by Peccerillo and Taylor (1976).

Figure 5. TTG normalized spidergrams (comments in text). Tm is omitted, as it is not reliably analysed in our dataset, and Lu and Yb are swapped to obtain smoother patters; this reflects the hook-shaped REE pattern of TTGs, with LuN > YbN. Colours as in Figure 4, samples dated in this work appear as thicker lines. The grey fields show the whole range of our data, for orientation.

Figure 6. TTG normalized spidergrams for various trace elements, arranged by increasing variablity. Comments in text, same caption as Figure 5.

Figure 7. Zoning patterns of zircons from the Heerenveen and Mpuluzi batholiths, and from Lower Onverwacht volcanics and meta arkose. Circles mark laser spots drilled for U-Pb dating; sample number and respective $^{207}Pb/^{206}Pb$ ages are presented as well. Most images are back-scattered electron images, cathodoluminescence images are marked with CL.

Figure 8. Representative concordia diagrams showing results of U-Pb dating of magmatic zircon in different samples of the (a-c) Heerenveen batholith, (f) Mpuluzi batholith, and in (e) Theespruit meta-volcanics, as well as of (f) detrital zircons in Lower Onverwacht meta-arkose. (Concordia diagrams of all investigated samples are shown in Figure 2 : supplementary online material).

Figure 9. Age-εHf diagram summarizing the results of U-Pb-Hf isotope analyses of (a) felsic and (ultra)mafic igneous rocks, and (b) clastic metasedimentary rocks from the Barberton Greenstone Belt (GSB), Swaziland, and Commondale GSB. Data source: (1) Zeh et al. (2009), (2) Zeh et al. (2011), (3) Zeh et al. (2013), (4) Kröner et al. (2013), (5) Kröner et al. (2014) (6) Kröner et al. (2016) (7) Kröner et al. (2018), (8) Hoffmann et al. (2017), (9) Hoffmann et al. (2016) (10) Taylor et al. (2016), (11) van Schijndel et al. (2017), (12) Schneider et al. (2019). M-Mpageni granite, SMN- Sincunusa - Mbabane-Ngwempisi-granites, S-Sinceni granite, C-Cunningmore tonalite, MNP-Mpuluzi-Nelspruit-Piggs Peak batholithe (i.e. GMS suite), KNS-Kaap Valley-Nelshoogte-Stentor-tonalites, D-Dalmein granite, AGC-Ancient Gneiss Complex-granite dikes. CHUR-chondric uniform reservoir, DM-depleted mantle evolution based on $^{176}Hf/^{177}Hf$(today)=0.283250, and $^{176}Lu/^{177}Hf$=0.0384 (Chauvel and Blichert-Toft, 2001); Arrows mark crust evolutionary trends [$^{176}Lu/^{177}Hf$=0.0113, average continental crust; average (Taylor and McLennan, 1985) and (Wedepohl, 1995); $^{176}Lu/^{177}Hf$=0.026; average of Barberton ultramafic rocks, n=48; from Schneider et al. (2019).

Figure 10. Trace element characteristics of low-Ca granitoids of the GMS suite. Symbols and colours as in Fig. 4. On each diagram, the overall evolution is related to partial melting (PM) and fractional crystallization (FC), as discussed in the text and indicated by grey arrows.

Figure 11. Discussion on the syenitic component is based on the two diagrams of Laurent et al. (2014a). (a) A ternary diagram Al_2O_3/(FeOt+MgO) – 3 CaO – 5 K_2O/Na_2O offers a good discrimination between melts generated from different (crustal) sources.. (b) the A/CNK (= molecular Al_2O_3 / CaO + Na_2O + K_2O) – Na_2O + K_2O – 2 FSMB (= [FeOt + MgO] × [Sr + Ba]) ternary diagram efficiently isolates the “sanukitoid-like” component, pointing towards the FSMB apex, from other types of granitoids.

Figure 12. Summary of the petrogenetic processes leading to petrological diversity but isotopic homogeneity.

Figure 13. Age vs K_2O. In addition to ages reported in Table 3, this figure also includes (unpublished) ages by Murphy (2015), depicted as smaller symbols (with the same colour code). Symbols as in Figure 4. This evidences the possible presence of long-lived pre-3110 Ma magmatism (high K_2O, low Ca granitoids) that we attribute to low degrees of melting (± fractionation) of the Grey Gneisses, contrasting with the short pulse of very diverse magmas of the GMS event proper at ca. 3.1 Ga, witnessing higher degree of melting of a range of sources. Inset: distribution of published ages in the BGGT (top) and AGC (bottom). Both feature the same, ca. 3230 Ma peak. However, in the deeper structural levels (the ACG) , note the occurrence of 3150—3200 Ma ages that attest to the persistence of hot (melting?) conditions in the lower/middle crust during this period. The ca. 3.1 Ga peak in the upper crust (BGGT) reflects the extraction and emplacement of all melts in the GMS suite.

Table 1. Summary of the chemical types of GMS rocks. The types and sub-types (first two columns) are those defined in this work, see text and Figure 4. The matching facies in each batholith are indicated (Figure 2). The chemical description from the last columns is given on the basis of the key features identified by Bonin et al. (2020). calc-alk: calc-alkalic; alk-calc: alkali-calcic; alk: alkali, terminology after Frost et al. (2001).

Table 2. Normalizing factors and order used in the diagrams of Figures 5 and 6.

Table 3. Summary of U-Pb ages obtained in this study on the Heerenveen and Mpuluzi batholiths, and on meta-volcanic rocks of the Lower Onverwacht Group, compared with published data (shaded rows). Long. and Lat.: longitude and latitude, given as decimal degrees.

Table 4. Summary of Hf isotopic results obtained in this study.

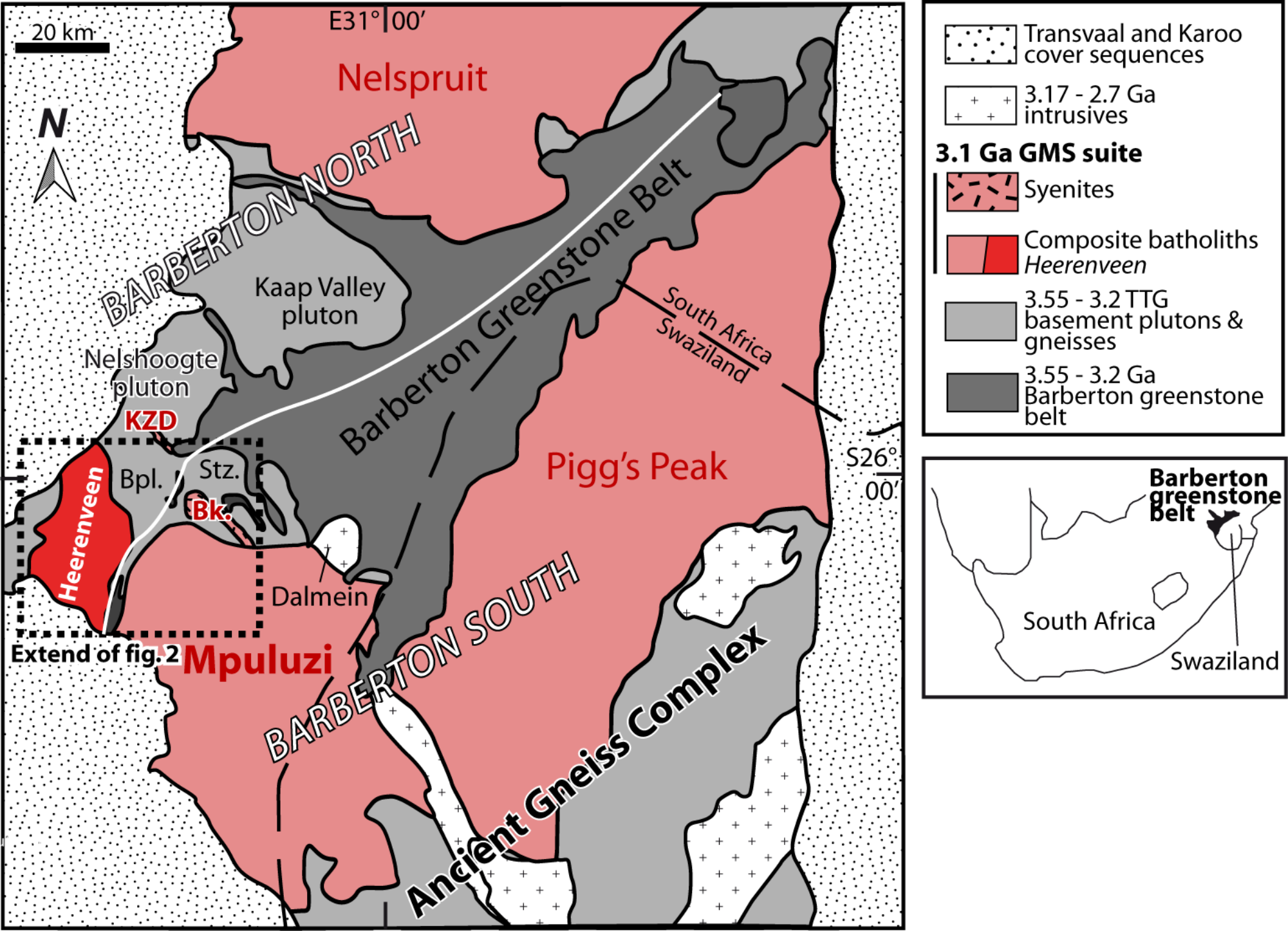
20 km
N
E31° 00′
S26° 00′
Nelspruit
BARBERTON NORTH
Barberton Greenstone Belt
Kaap Valley pluton
Nelshoogte pluton
KZD
South Africa
Swaziland
Heerenveen
Bpl.
Stz.
Bk.
Pigg's Peak
Dalmein
Extend of fig. 2
Mpuluzi
BARBERTON SOUTH
Ancient Gneiss Complex
Transvaal and Karoo cover sequences
3.17 - 2.7 Ga intrusives
3.1 Ga GMS suite
Syenites
Composite batholiths Heerenveen
3.55 - 3.2 TTG basement plutons & gneisses
3.55 - 3.2 Ga Barberton greenstone belt
Barberton greenstone belt
South Africa
Swaziland

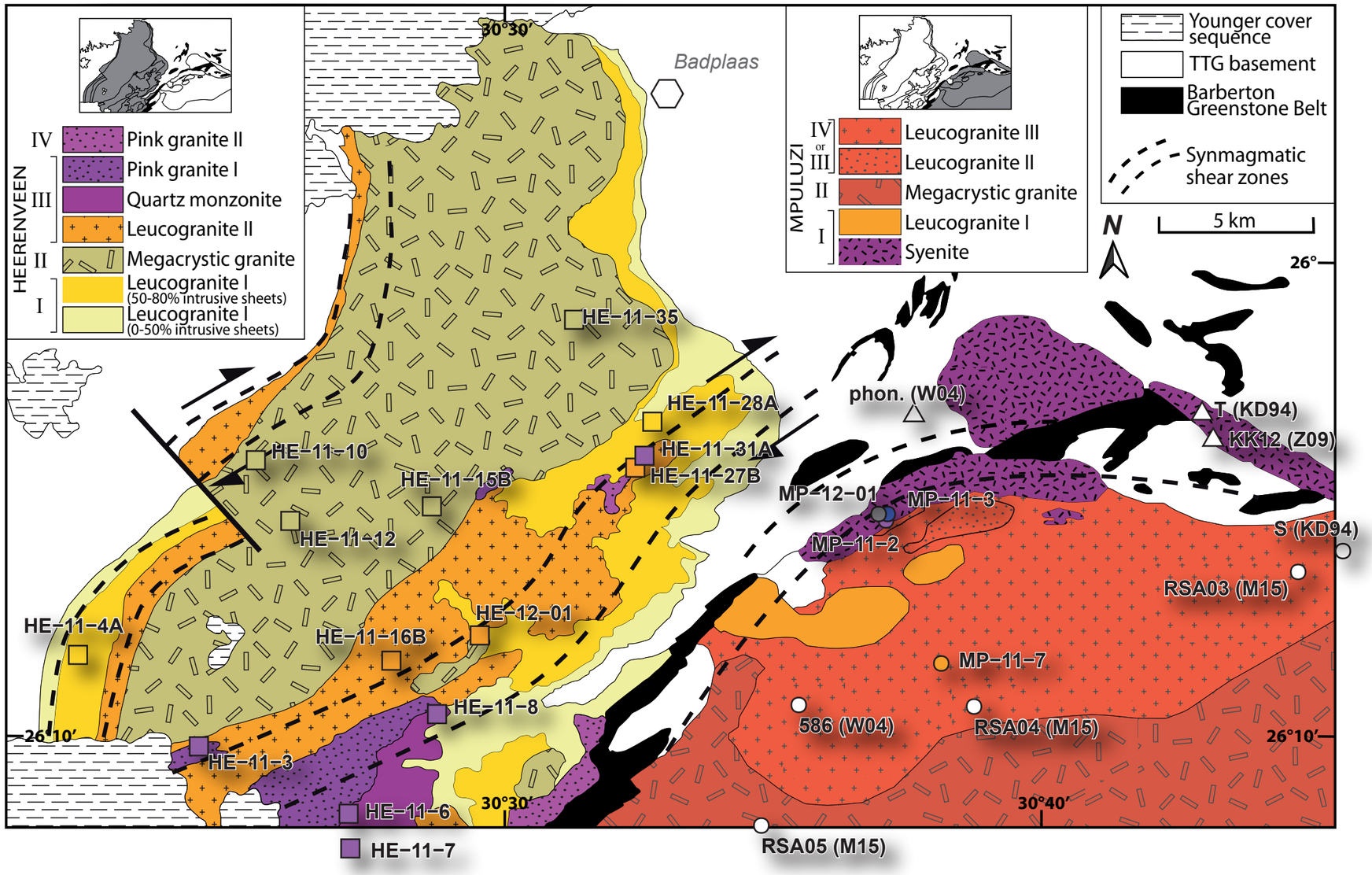
HEERENVEEN
IV
Pink granite II
Pink granite I
III
Quartz monzonite
Leucogranite II
II
Megacrystic granite
I
Leucogranite I
(50-80% intrusive sheets)
Leucogranite I
(0-50% intrusive sheets)
MPULUZI
IV or III
Leucogranite III
Leucogranite II
II
Megacrystic granite
I
Leucogranite I
Syenite
Younger cover sequence
TTG basement
Barberton Greenstone Belt
Synmagmatic shear zones
N
5 km
26°
26°10′
30°30′
30°40′
Badplaas
HE−11−35
HE−11−28A
HE−11−31A
HE−11−27B
HE−11−10
HE−11−15B
HE−11−12
HE−11−4A
HE−11−16B
HE−12−01
HE−11−8
HE−11−3
HE−11−6
HE−11−7
phon. (W04)
T (KD94)
KK12 (Z09)
MP−12−01
MP−11−3
MP−11−2
S (KD94)
RSA03 (M15)
MP−11−7
586 (W04)
RSA04 (M15)
RSA05 (M15)

HEERENVEEN

MPULUZI

BOESMANSKOP

a.

b.

c.

d.

e.

f.

g.

SG

SG

Peg

Aug

Aug

SG

SG

h.

i.

j.

k.

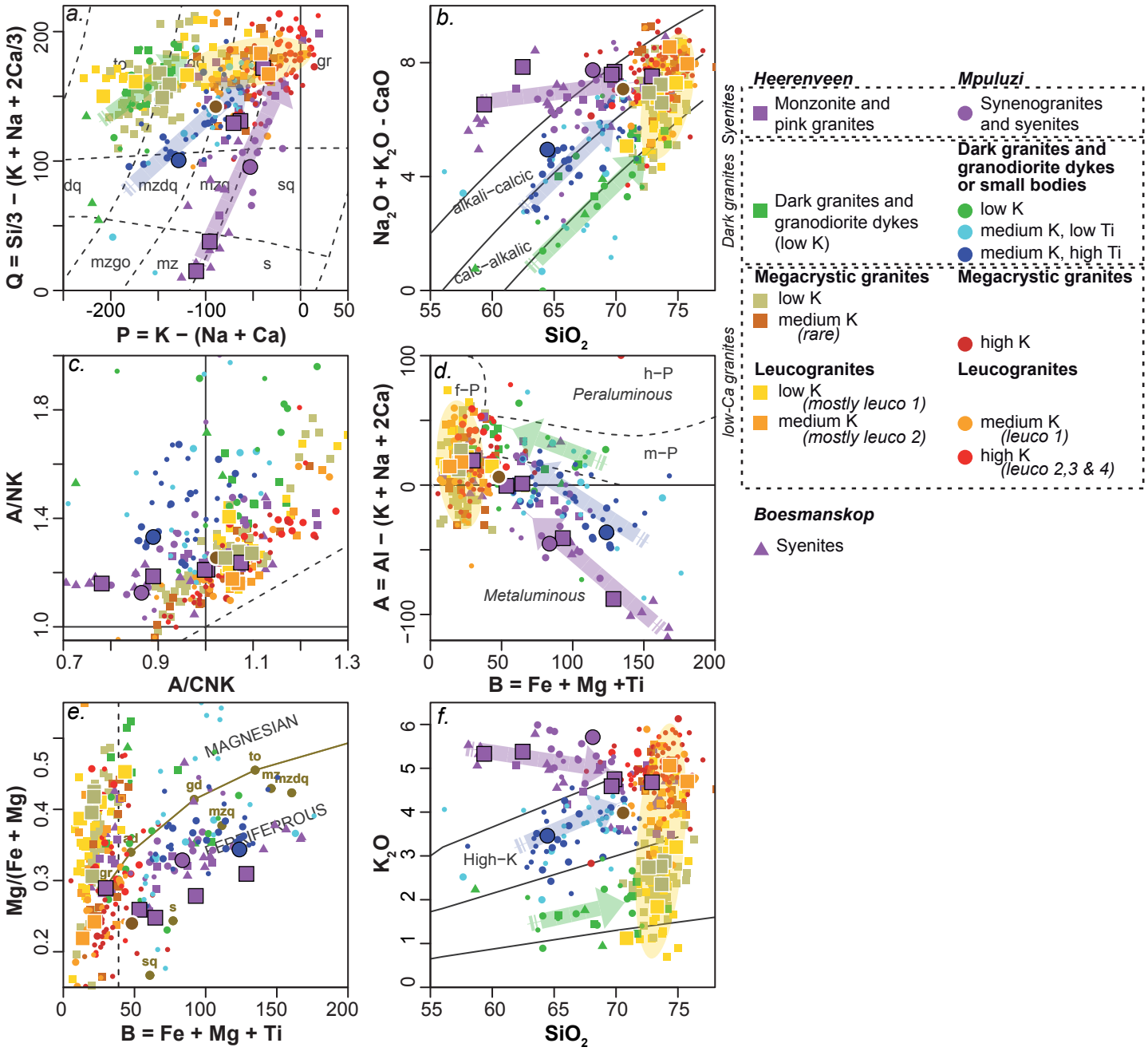
a.
Q = Si/3 − (K + Na + 2Ca/3)
P = K − (Na + Ca)
to
gd
gr
dq
mzdq
mzq
sq
mzgo
mz
s
b.
Na2O + K2O - CaO
SiO2
alkali−calcic
calc−alkalic
c.
A/NK
A/CNK
d.
A = Al − (K + Na + 2Ca)
B = Fe + Mg +Ti
h−P
f−P
m−P
Peraluminous
Metaluminous
e.
Mg/(Fe + Mg)
B = Fe + Mg + Ti
MAGNESIAN
FERRIFERROUS
f.
K2O
SiO2
High−K
Syenites
Heerenveen
Monzonite and pink granites
Mpuluzi
Synenogranites and syenites
Dark granites and granodiorite dykes (low K)
Dark granites and granodiorite dykes or small bodies
low K
medium K, low Ti
medium K, high Ti
Megacrystic granites
low K
medium K
(rare)
Megacrystic granites
high K
Leucogranites
low K
(mostly leuco 1)
medium K
(mostly leuco 2)
Leucogranites
medium K
(leuco 1)
high K
(leuco 2,3 & 4)
Boesmanskop
Syenites
Syenites
Dark granites
low-Ca granites

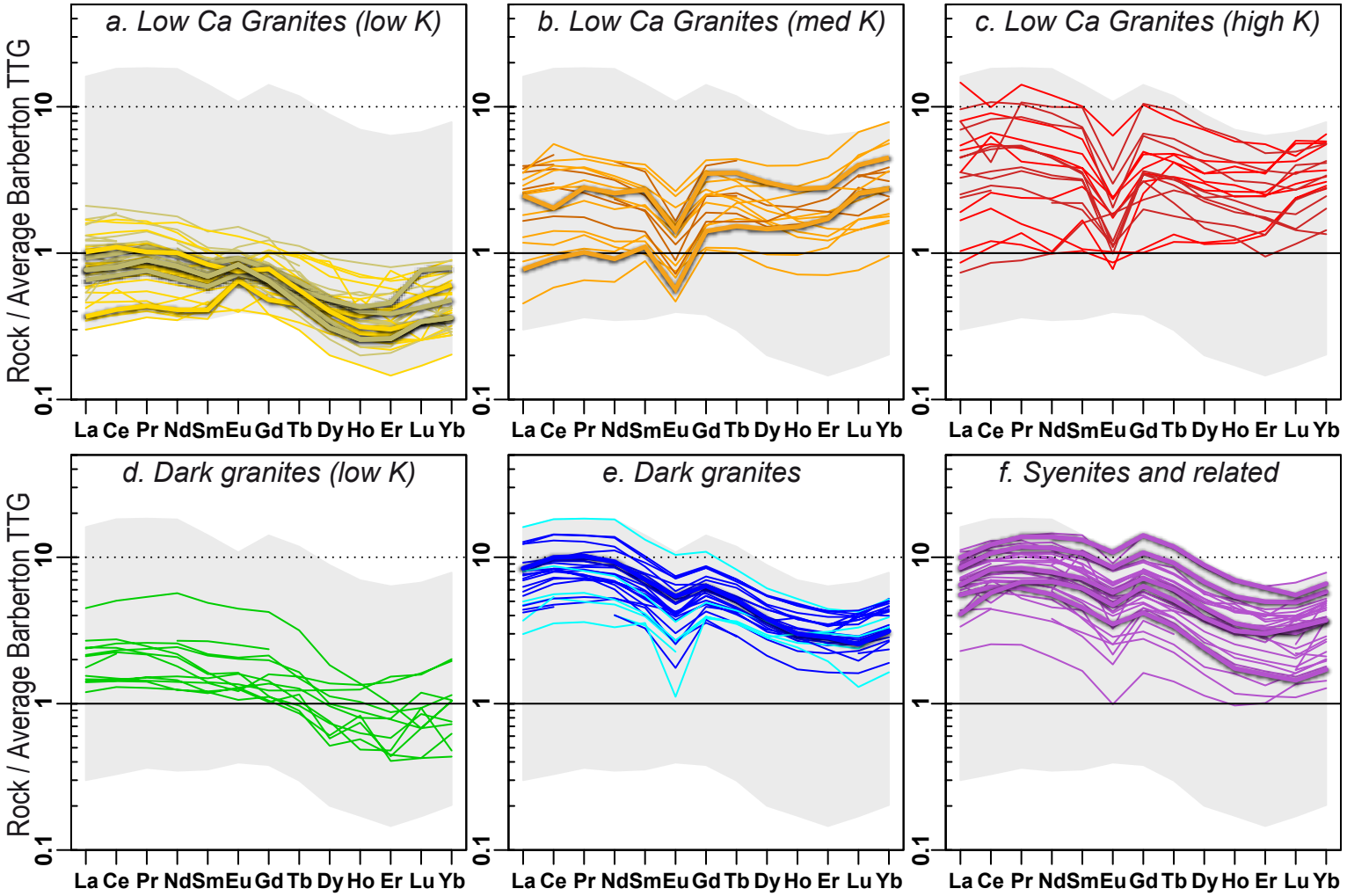
a. Low Ca Granites (low K)
b. Low Ca Granites (med K)
c. Low Ca Granites (high K)
d. Dark granites (low K)
e. Dark granites
f. Syenites and related
Rock / Average Barberton TTG
10
1
0.1
La Ce Pr Nd Sm Eu Gd Tb Dy Ho Er Lu Yb

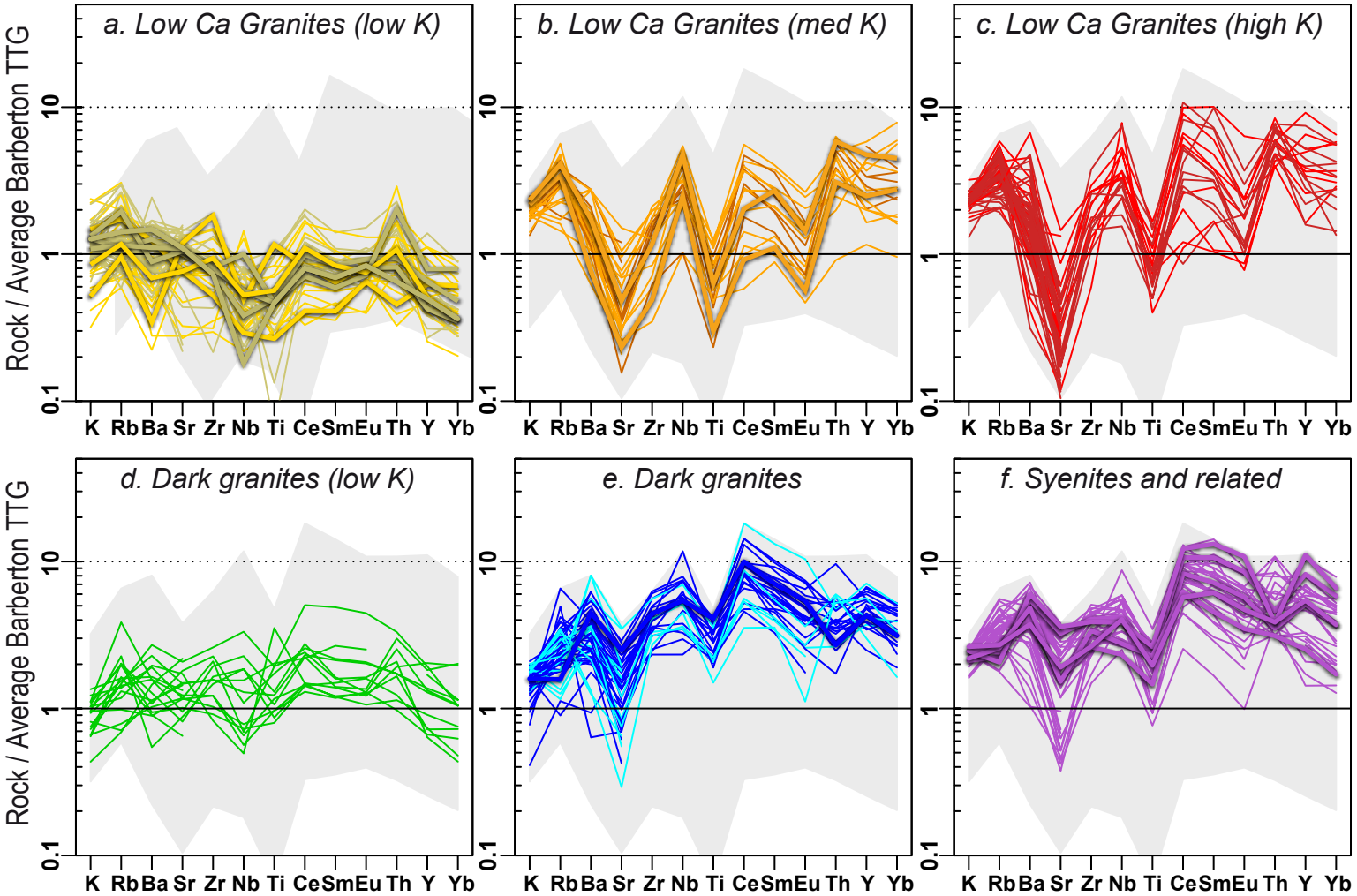
a. Low Ca Granites (low K)
b. Low Ca Granites (med K)
c. Low Ca Granites (high K)
d. Dark granites (low K)
e. Dark granites
f. Syenites and related
Rock / Average Barberton TTG
10
1
0.1
K Rb Ba Sr Zr Nb Ti Ce Sm Eu Th Y Yb

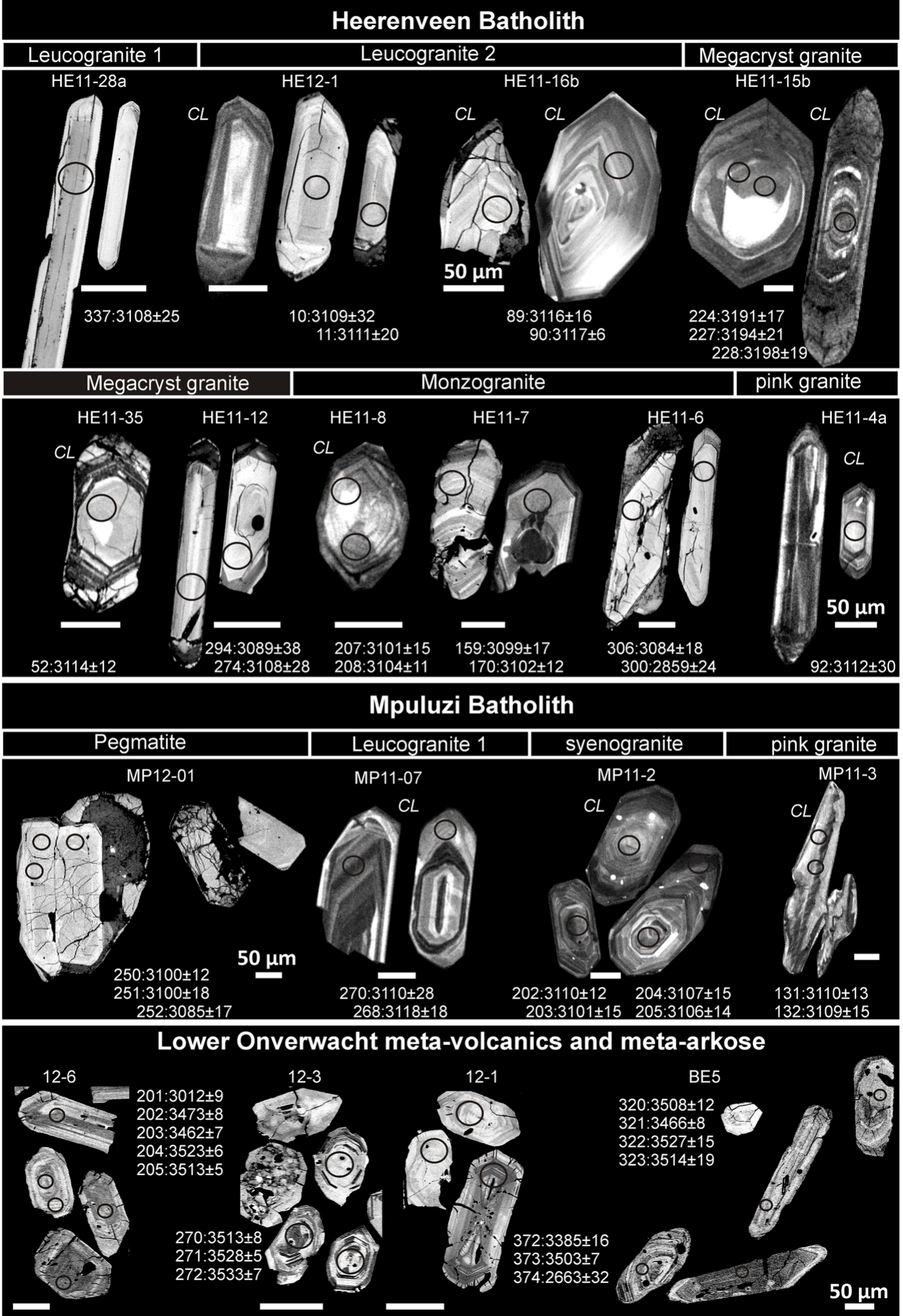
Heerenveen Batholith
Leucogranite 1
Leucogranite 2
Megacryst granite
HE11-28a
HE12-1
HE11-16b
HE11-15b
CL
CL
CL
CL
CL
50 µm
337:3108±25
10:3109±32
11:3111±20
89:3116±16
90:3117±6
224:3191±17
227:3194±21
228:3198±19
Megacryst granite
Monzogranite
pink granite
HE11-35
HE11-12
HE11-8
HE11-7
HE11-6
HE11-4a
CL
CL
CL
50 µm
52:3114±12
294:3089±38
274:3108±28
207:3101±15
208:3104±11
159:3099±17
170:3102±12
306:3084±18
300:2859±24
92:3112±30
Mpuluzi Batholith
Pegmatite
Leucogranite 1
syenogranite
pink granite
MP12-01
MP11-07
MP11-2
MP11-3
CL
CL
CL
50 µm
250:3100±12
251:3100±18
252:3085±17
270:3110±28
268:3118±18
202:3110±12
203:3101±15
204:3107±15
205:3106±14
131:3110±13
132:3109±15
Lower Onverwacht meta-volcanics and meta-arkose
12-6
12-3
12-1
BE5
201:3012±9
202:3473±8
203:3462±7
204:3523±6
205:3513±5
270:3513±8
271:3528±5
272:3533±7
372:3385±16
373:3503±7
374:2663±32
320:3508±12
321:3466±8
322:3527±15
323:3514±19
50 µm

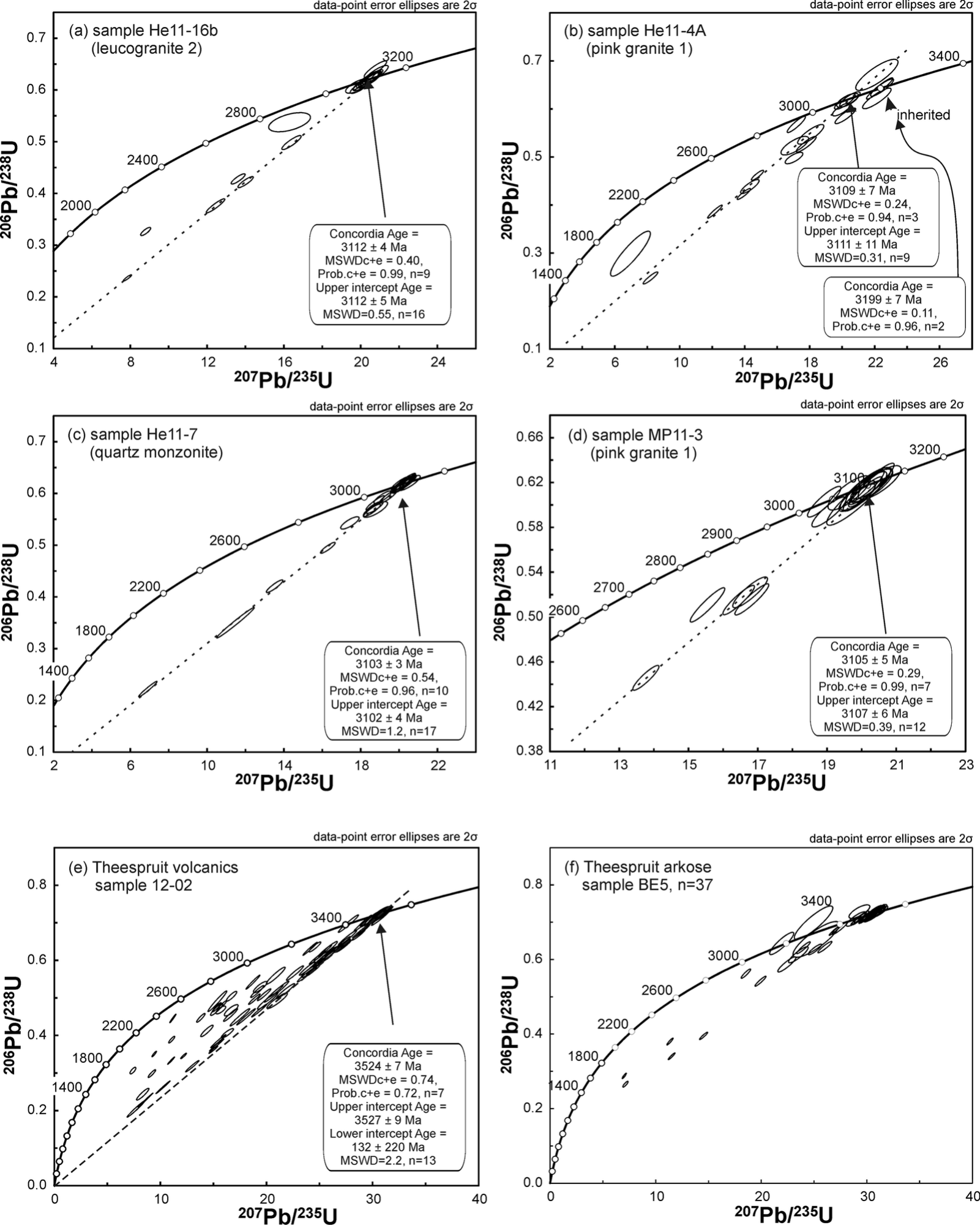
data-point error ellipses are 2σ
(a) sample He11-16b
(leucogranite 2)
Concordia Age =
3112 ± 4 Ma
MSWDc+e = 0.40,
Prob.c+e = 0.99, n=9
Upper intercept Age =
3112 ± 5 Ma
MSWD=0.55, n=16
(b) sample He11-4A
(pink granite 1)
inherited
Concordia Age =
3109 ± 7 Ma
MSWDc+e = 0.24,
Prob.c+e = 0.94, n=3
Upper intercept Age =
3111 ± 11 Ma
MSWD=0.31, n=9
Concordia Age =
3199 ± 7 Ma
MSWDc+e = 0.11,
Prob.c+e = 0.96, n=2
(c) sample He11-7
(quartz monzonite)
Concordia Age =
3103 ± 3 Ma
MSWDc+e = 0.54,
Prob.c+e = 0.96, n=10
Upper intercept Age =
3102 ± 4 Ma
MSWD=1.2, n=17
(d) sample MP11-3
(pink granite 1)
Concordia Age =
3105 ± 5 Ma
MSWDc+e = 0.29,
Prob.c+e = 0.99, n=7
Upper intercept Age =
3107 ± 6 Ma
MSWD=0.39, n=12
(e) Theespruit volcanics
sample 12-02
Concordia Age =
3524 ± 7 Ma
MSWDc+e = 0.74,
Prob.c+e = 0.72, n=7
Upper intercept Age =
3527 ± 9 Ma
Lower intercept Age =
132 ± 220 Ma
MSWD=2.2, n=13
(f) Theespruit arkose
sample BE5, n=37
206Pb/238U
207Pb/235U

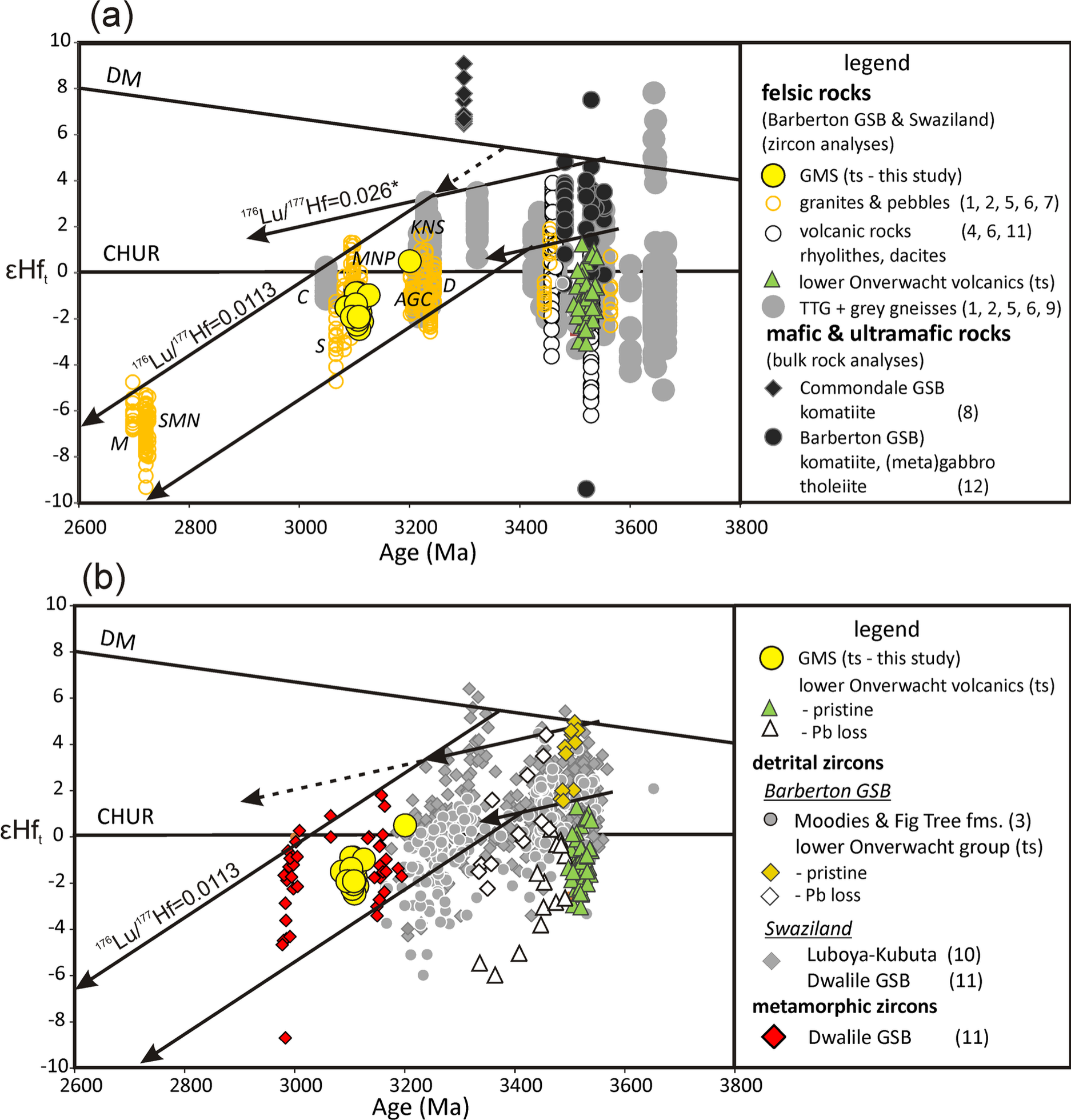
(a)
DM
CHUR
$^{176}Lu/^{177}Hf=0.026^{*}$
$^{176}Lu/^{177}Hf=0.0113$
KNS
MNP
AGC
C
D
S
M
SMN
εHf$_t$
Age (Ma)
legend
felsic rocks
(Barberton GSB & Swaziland)
(zircon analyses)
GMS (ts - this study)
granites & pebbles (1, 2, 5, 6, 7)
volcanic rocks (4, 6, 11)
rhyolithes, dacites
lower Onverwacht volcanics (ts)
TTG + grey gneisses (1, 2, 5, 6, 9)
mafic & ultramafic rocks
(bulk rock analyses)
Commondale GSB
komatiite (8)
Barberton GSB)
komatiite, (meta)gabbro
tholeiite (12)
(b)
DM
CHUR
$^{176}Lu/^{177}Hf=0.0113$
εHf$_t$
Age (Ma)
legend
GMS (ts - this study)
lower Onverwacht volcanics (ts)
- pristine
- Pb loss
detrital zircons
Barberton GSB
Moodies & Fig Tree fms. (3)
lower Onverwacht group (ts)
- pristine
- Pb loss
Swaziland
Luboya-Kubuta (10)
Dwalile GSB (11)
metamorphic zircons
Dwalile GSB (11)

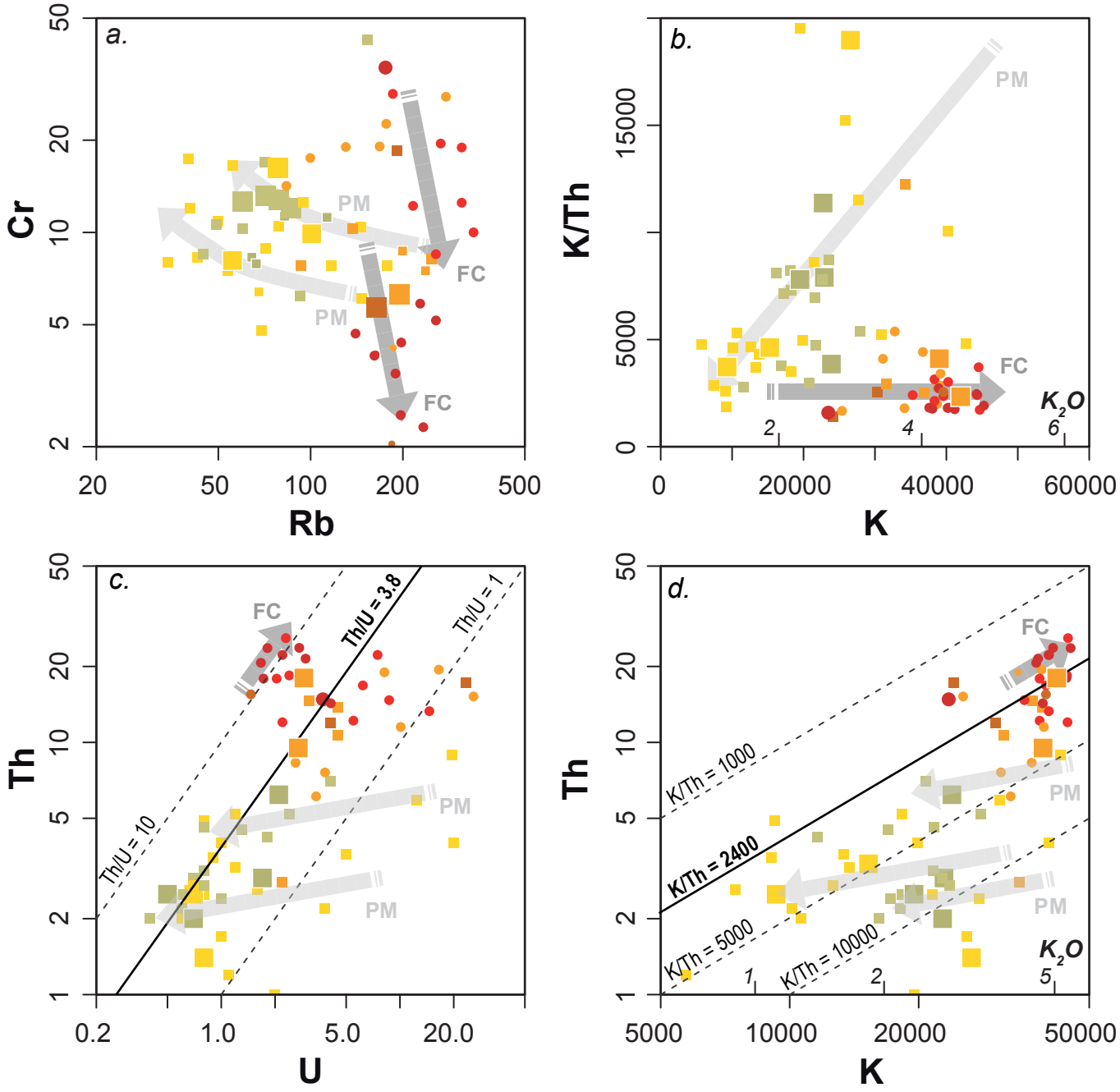
a.
Cr
Rb
PM
FC
PM
FC
b.
K/Th
K
PM
FC
K_2O
2
4
6
c.
Th
U
FC
Th/U = 3.8
Th/U = 1
Th/U = 10
PM
PM
d.
Th
K
FC
K/Th = 1000
K/Th = 2400
K/Th = 5000
K/Th = 10000
PM
PM
K_2O
1
2
5

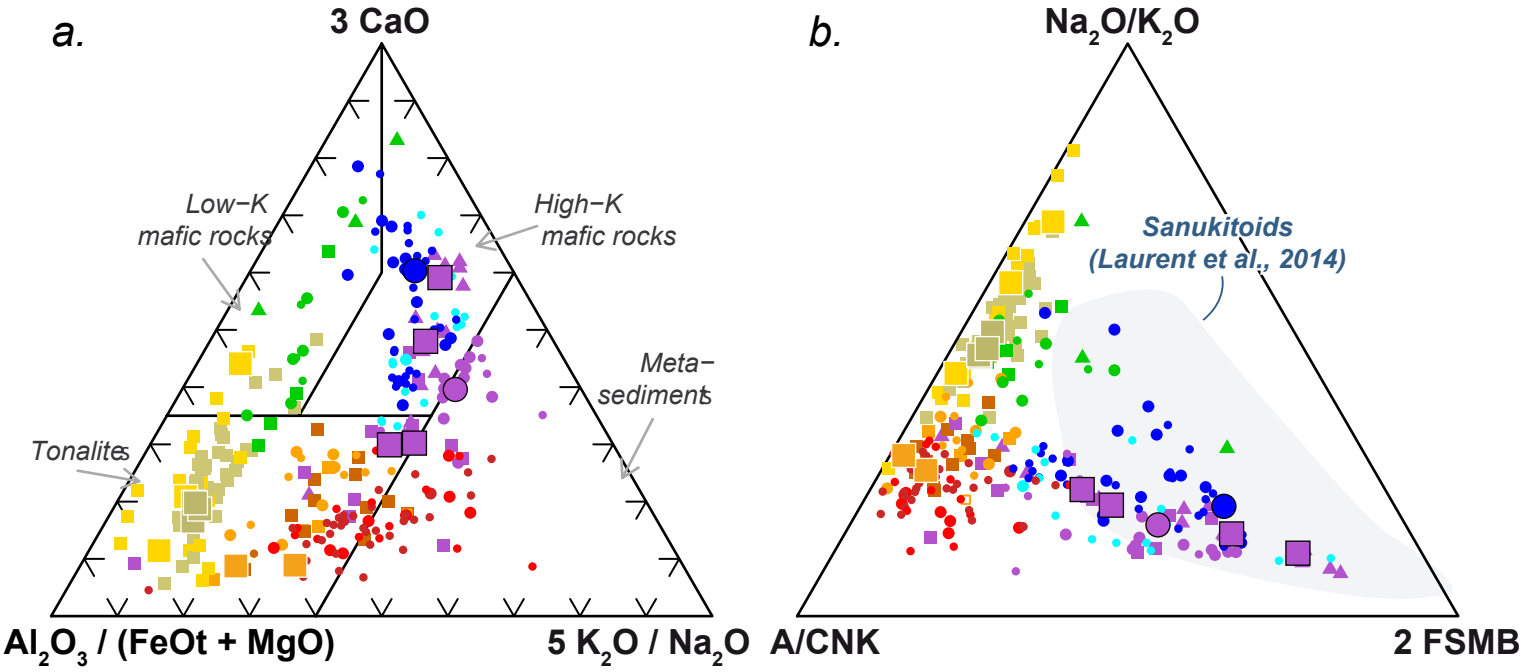
a.
3 CaO
Low−K
mafic rocks
High−K
mafic rocks
Meta−
sediments
Tonalites
Al2O3 / (FeOt + MgO)
5 K2O / Na2O
b.
Na2O/K2O
Sanukitoids
(Laurent et al., 2014)
A/CNK
2 FSMB

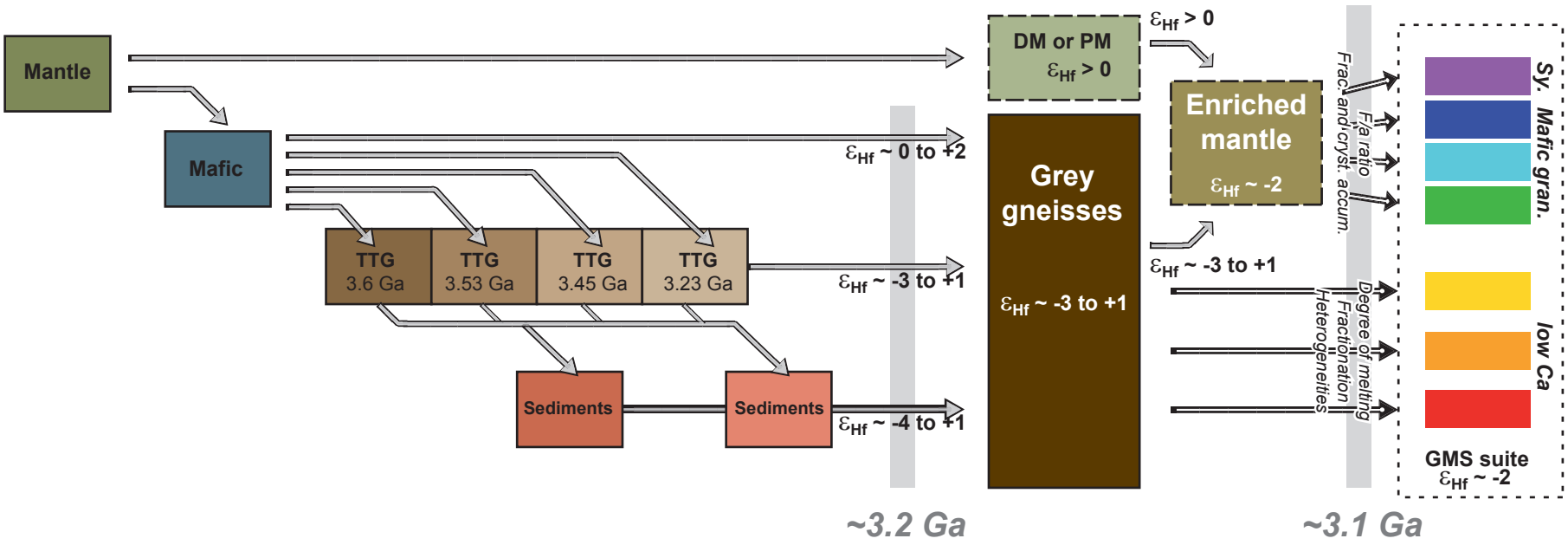
Mantle
Mafic
TTG
3.6 Ga
TTG
3.53 Ga
TTG
3.45 Ga
TTG
3.23 Ga
Sediments
Sediments
εHf ~ 0 to +2
εHf ~ -3 to +1
εHf ~ -4 to +1
~3.2 Ga
DM or PM
εHf > 0
Grey
gneisses
εHf ~ -3 to +1
εHf > 0
Enriched
mantle
εHf ~ -2
εHf ~ -3 to +1
Frac. and cryst. accum.
F/a ratio
Degree of melting
Fractionation
Heterogeneities
Sy. Mafic gran.
low Ca
GMS suite
εHf ~ -2
~3.1 Ga

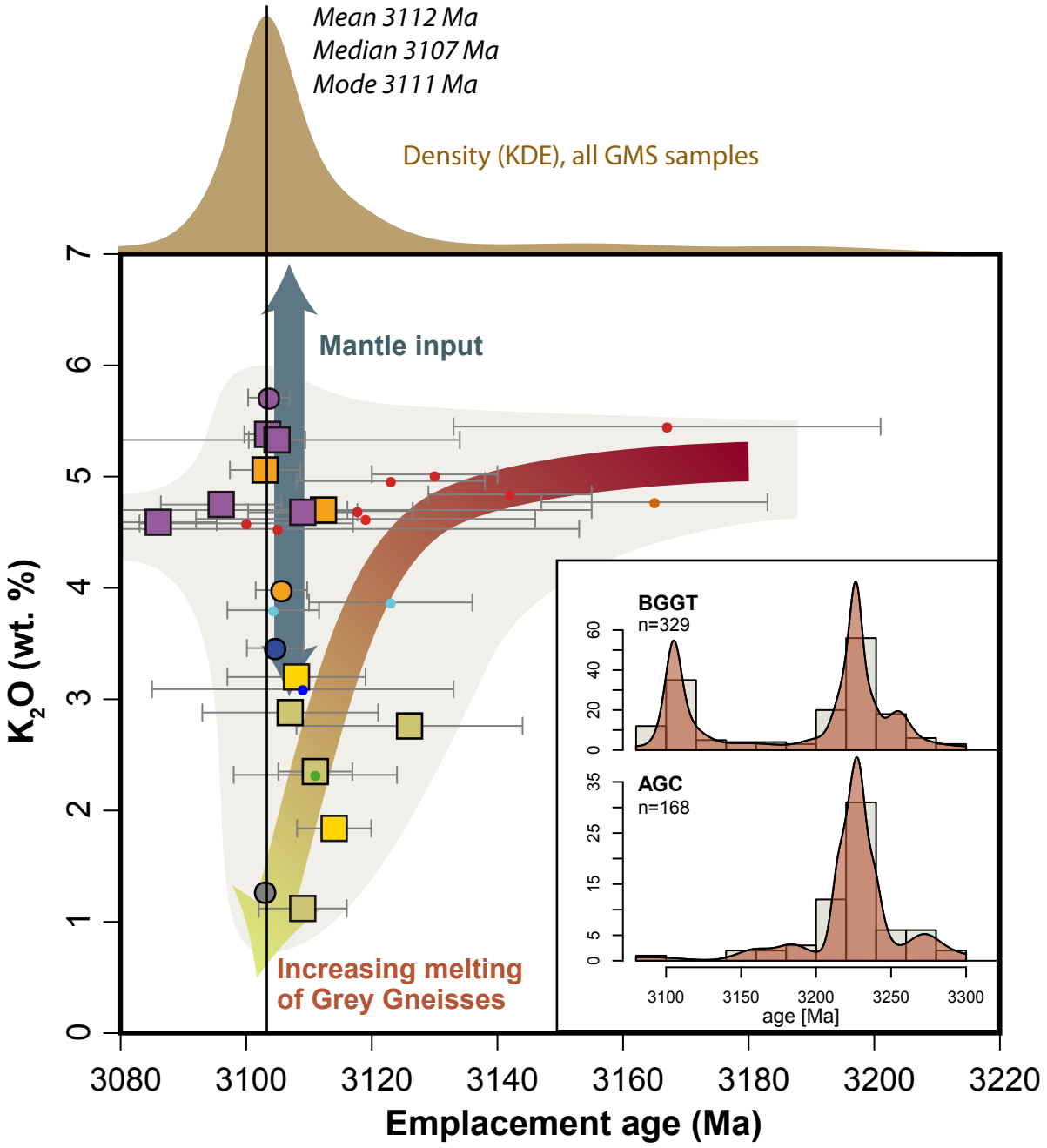
Mean 3112 Ma
Median 3107 Ma
Mode 3111 Ma
Density (KDE), all GMS samples
Mantle input
Increasing melting
of Grey Gneisses
BGGT
n=329
AGC
n=168
age [Ma]
K_2O (wt. %)
Emplacement age (Ma)

Chemical type	Sub-type	Mpuluzi	Herenveen	Boesmanskop	Mg/Fe balance	Alkalinity	Aluminosity	Na/K balance
low-Ca granitoids	low K_2O	leucogranite I	Main megacrystic facies leucogranite I		Magnesian	calc-alk	felsic peraluminous	mostly medium K series
	medium K_2O		leucogranite II		Magnesian or Ferroan	alk-calc to calc-alk	felsic peraluminous	high K series
	high K_2O	leucogranites II, III and IV Main megacrystic facies			Ferroan	alk-calc	felsic peraluminous	high K to shoshonitic series
syenites and related		Syenite / Syenogranite	Monzonite Pink granite	Syenite	Ferroan	alk-calc to alk	strongly metaluminous	mostly shoshonitic series
dark granites	low K_2O	Some grey dykes; portions of main megacrystic facies (from literature - undescribed) Eagle High "Augen granodiorite"	Grey granite & granodiorite dykes	Some "mafic" dykes	Magnesian	calc-alk	weakly peraluminous	medium K series
	medium K_2O / low TiO_2				Magnesian or Ferroan	alk-calc to calc-alk	weakly peraluminous	high K series
	medium K2O / high TiO_2				Ferroan	alk-calc to calc-alk	metaluminous	high K series

Order and values for REE spidergrams

La	Ce	Pr	Nd	Sm	Eu	Gd	Tb	Dy	Ho	Er	Lu	Yb
17.60	29.84	3.19	12.24	2.37	0.71	1.71	0.27	1.75	0.35	0.96	0.12	0.69

Order and values for multi-elements diagrams

K	Rb	Ba	Sr	Zr	Nb	Ti	Ce	Sm	Eu	Th	Y	Yb
17993.96	58.00	344.53	526.93	120.28	5.50	1802.24	29.84	2.37	0.71	3.08	7.07	0.69

Table 3: Summary of U-Pb dating results

sample	Facies	Chemical type	Lat.	Long.	all n	Discordia AGE u.i.(Ma)	Discordia ±2σ (Ma)[a]	Discordia AGE l.i.(Ma)	Discordia ±2σ (Ma)	Discordia MSWD	Discordia Prob.	Discordia n	Concordia (99-101%) AGE conc.(Ma)	Concordia ±2σ (Ma)[a]	Concordia MSWD c+e[b]	Concordia Prob. c+e[b]	Concordia n	comment / ref
Heerenveen																		
HE-11-28A	*Leucogranite*	*lowK Leucogr*	*-26.0580*	*30.5619*	11	3068	60	482	200	81*		11	3108	23		0.97	1	
HE-12-1	*Leucogranite*	*lowK Leucogr*	*-26.1329*	*30.4990*	20	3118	11	29	29	0.97	0.47	13	3114	12	0.54	0.80	4	
HE-11-27A	*Leucogranite*	*mediumK Leu*	*-26.0721*	*30.5574*	7								3103	11	0.23	1.00	6	
HE-11-16b	*Leucogranite*	*mediumK Leu*	*-26.1431*	*30.4721*	20	3112	9	-26	28	0.55	0.9	16	3112	8	0.40	0.99	9	
HE-11-15B	*Megacryst gra*	*lowK megacr.*	*-26.0869*	*30.4859*	17	3199	10	3	35	0.31	0.93	8	3201	9	0.22	0.99	5	(all zircons inherited)
HE-11-35	*Megacryst gra*	*lowK megacr.*	*-26.0264*	*30.5353*	19								3111	12	0.23	0.88	2	rited grains at 3.2 Ga
HE-11-12	*Megacryst gra*	*lowK megacr.*	*-26.0938*	*30.4380*	18	3124	15	58	41	0.53	0.75	7	3107	27		0.93	1	rited grains at 3.2 Ga
HE-11-10	*Megacryst gra*	*lowK megacr.*	*-26.0722*	*30.4236*	5								3126	37	0.06	0.81	1	
HE-11-8	*Quartz monzo*	*Sy, Mz, pink (	*-26.1586*	*30.4836*	24	3102	9	2	60	1.60	0.11	12	3105	9	0.13	1.00	4	
HE-11-7	*Quartz monzo*	*Sy, Mz, pink (	*-26.1993*	*30.4545*	21	3102	8	-31	70	1.20	0.24	17	3103	7	0.54	0.95	10	
HE-11-6	*Quartz monzo*	*Sy, Mz, pink (	*-26.1948*	*30.4542*	18	3079	24	207	68	7.1*		17	3086	19	0.28	0.60	1	
HE-11-3	*Pink granite 1*	*Sy, Mz, pink (	*-26.1674*	*30.4094*	16	3109	11	2.9	4	0.14	0.94	5						
HE-11-4A	*Pink granite 1*	*Sy, Mz, pink (	*-26.1277*	*30.3746*	20	3111	13	-13	62	0.31	0.95	9	3109	14	0.24	0.94	3	
						3199	13	265	270	0.19	0.83	4	3199	13	0.11	0.95	2	rited grains at 3.2 Ga
HE-11-31A	*Pink granite 2*	*Sy, Mz, pink (	*-26.0706*	*30.5588*	4								3096	19	0.92	0.47	3	
Mpuluzi																		
MP-12-01	*Pegmatite*		*-26.0957*	*30.6297*	12	3104	9	-584	170	0.57	0.78	9	3103	9	0.32	0.97	5	verse concordant
MP-11-7	*Leucogranite*	*mediumK Leu*	*-26.1458*	*30.6468*	23	3109	9	-80	360	0.84	0.63	16	3106	8	0.28	1.00	8	
MP-11-3	*Pink granite 1*	*Sy, Mz, pink (	*-26.0965*	*30.6312*	19	3107	10	133	230	0.39	0.95	12	3105	9	0.29	0.99	7	
MP-11-2	*Syenogranite*	*Sy, Mz, pink (	*-26.0963*	*30.6309*	21								3104	7	0.48	0.99	16	
S	*Leucogranite*	*probably high*	*-26.1465*	*30.7743*[x]									3107.0	4.0				Kamo and Davies 1994, TIMS
586	*Leucogranite*	*probably high*	*-26.1563*	*30.6065*									3105.6	2.4				Westraat et al. 2004, TIMS
Boesmanskop																		
unnamed	*Phonolite*	*Sy, Mz, pink (	*-26.0570*	*30.6571*									3096.0	4.0				Westraat et al. 2004, TIMS
T	*Syenite, Bk."t*	*Sy, Mz, pink (	*-26.0663*	*30.7324*[x]									3107.0	2.0				Kamo and Davies 1994, TIMS
Theespruit volcanics																		
.12-1	*Felsic schist*		*-26.0029*	*30.7893*	115	3521	10	-3	110	8.0*		13	3530	8	0.99	0.43	4	
.12-2	*Agglomerate*		*-26.0029*	*30.7893*	87	3527	9	132	220	2.2*		13	3524	7	0.74	0.72	7	
.12-3	*Conglomerate*		*-25.9960*	*30.7867*	52	3527	9	-6	30	3.2*		12	3527	8	0.22	0.88	2	
.12-6	*Felsic schist*		*-26.0144*	*30.7835*	66	3531	9	132	60	3.9*		23	3531	7	1.30	0.13	12	

u.i.-upper intercept, l.i.-lower intercept, Prob.-Probability

[x] approximate location, read from published map

[a] error without (and with) decay constant error

c+e[b]-MSWD and Probability of concordance and equivalence

*MSWD of discordia (reference) line

Table X: Results of Lu-Yb-Hf-isotope LA-ICP-(MC)MS analyses (unknowns and standards)

	$^{176}Yb/^{177}Hf$ (a)	±2σ	$^{176}Lu/^{177}Hf$ (a)	±2σ	$^{178}Hf/^{177}Hf$	$^{180}Hf/^{177}Hf$	Sig_{Hf} (b) (V)	$^{176}Hf/^{177}Hf$	±2σ (c)	$^{176}Hf/^{177}Hf_{(t)}$ (d)	$\varepsilon Hf_{(t)}$ (d)	±2σ (c)	T_{DM2} (e) (Ga)	age (e) (Ma)	±2σ
HE-12-1															
a6	0.0144	23	0.00048	8	1.46715	1.88690	10	0.280724	38	0.280696	-2.8	1.3	3.59	3114	12
a8	0.0116	5	0.00039	2	1.46715	1.88676	7	0.280728	35	0.280704	-0.4	1.3	3.53	3200	12
a9	0.0238	5	0.00071	1	1.46714	1.88678	9	0.280756	32	0.280713	-2.1	1.1	3.56	3114	12
a10	0.0284	12	0.00095	5	1.46713	1.88710	6	0.280749	66	0.280692	-2.9	2.4	3.60	3114	12
a11	0.0137	8	0.00043	2	1.46722	1.88693	7	0.280719	37	0.280694	-2.9	1.3	3.60	3114	12
a12	0.0315	44	0.00087	13	1.46714	1.88691	9	0.280774	35	0.280722	-1.9	1.3	3.54	3114	12
a13	0.0179	14	0.00054	3	1.46720	1.88670	12	0.280751	36	0.280719	-1.9	1.3	3.55	3114	12
a14	0.0162	6	0.00048	1	1.46718	1.88666	9	0.280768	36	0.280739	-1.2	1.3	3.51	3114	12
a17	0.0121	16	0.00039	5	1.46717	1.88692	10	0.280730	31	0.280707	-2.4	1.1	3.57	3114	12
a18	0.0221	8	0.00066	3	1.46720	1.88673	9	0.280760	40	0.280720	-1.9	1.4	3.55	3114	12
a19	0.0165	9	0.00055	3	1.46709	1.88686	7	0.280733	38	0.280700	-2.6	1.4	3.58	3114	12
a21	0.0155	9	0.00044	2	1.46716	1.88669	10	0.280778	35	0.280751	1.2	1.2	3.44	3200	12
a22	0.0183	10	0.00058	3	1.46724	1.88674	10	0.280775	38	0.280741	-1.2	1.4	3.51	3114	12
a23	0.0289	16	0.00083	4	1.46719	1.88658	9	0.280764	46	0.280714	-2.1	1.6	3.56	3114	12
a24	0.0103	8	0.00029	2	1.46712	1.88654	9	0.280741	49	0.280723	-1.8	1.7	3.54	3114	12
HE-11-3															
a28	0.1437	104	0.00386	27	1.46716	1.88668	7	0.280913	40	0.280682	-3.4	1.4	3.62	3109	11
a29	0.1132	97	0.00332	19	1.46713	1.88689	9	0.280897	43	0.280699	-2.8	1.5	3.59	3109	11
a31	0.1690	134	0.00454	30	1.46711	1.88688	10	0.280972	40	0.280701	-2.7	1.4	3.59	3109	11
a38	0.1099	95	0.00304	27	1.46719	1.88666	9	0.280916	36	0.280735	-1.5	1.3	3.52	3109	11
a39	0.1160	48	0.00316	12	1.46720	1.88676	8	0.280921	32	0.280732	-1.6	1.2	3.52	3109	11
a43	0.1466	54	0.00391	13	1.46713	1.88671	8	0.280964	39	0.280730	-1.7	1.4	3.53	3109	11
a45	0.1859	58	0.00496	18	1.46719	1.88678	10	0.280974	41	0.280677	-3.5	1.4	3.63	3109	11
HE-11-35															
a48	0.0265	10	0.00090	3	1.46723	1.88675	7	0.280790	36	0.280736	-1.4	1.3	3.52	3111	12
a49	0.0063	12	0.00020	3	1.46716	1.88660	9	0.280764	31	0.280752	-0.8	1.1	3.48	3111	12
a51	0.0247	10	0.00083	3	1.46726	1.88682	9	0.280767	38	0.280717	-2.1	1.3	3.55	3111	12
a52	0.0201	20	0.00075	8	1.46717	1.88678	8	0.280770	37	0.280725	-1.8	1.3	3.54	3111	12
a53	0.0361	63	0.00111	20	1.46722	1.88660	10	0.280796	39	0.280730	-1.6	1.4	3.53	3111	12
a54	0.0410	16	0.00145	4	1.46722	1.88672	8	0.280795	36	0.280708	-2.4	1.3	3.57	3111	12
a56	0.0431	28	0.00116	10	1.46714	1.88675	10	0.280807	35	0.280738	-1.3	1.3	3.51	3111	12
a57	0.0423	20	0.00168	8	1.46716	1.88672	11	0.280841	30	0.280741	-1.2	1.1	3.51	3111	12
a58	0.0367	15	0.00135	7	1.46717	1.88683	12	0.280715	28	0.280634	-5.0	1.0	3.72	3111	12
a59	0.0157	6	0.00058	1	1.46708	1.88672	10	0.280743	30	0.280708	-0.3	1.1	3.52	3200	12
a60	0.0156	8	0.00056	5	1.46715	1.88675	9	0.280789	34	0.280754	1.3	1.2	3.43	3200	12
a61	0.0367	10	0.00125	3	1.46719	1.88678	10	0.280803	34	0.280728	-1.7	1.2	3.53	3111	12
a62	0.0392	12	0.00111	3	1.46708	1.88696	10	0.280754	41	0.280688	-3.1	1.5	3.61	3111	12
HE-11-16B															
a72	0.0413	48	0.00131	13	1.46716	1.88692	6	0.280787	39	0.280708	-2.4	1.4	3.57	3112	8
a73	0.0336	19	0.00127	7	1.46719	1.88663	5	0.280835	41	0.280759	-0.6	1.5	3.47	3112	8
a74	0.0422	17	0.00148	7	1.46720	1.88658	8	0.280814	40	0.280725	-1.8	1.4	3.54	3112	8
a75	0.0272	14	0.00097	4	1.46710	1.88669	6	0.280793	41	0.280735	-1.4	1.4	3.52	3112	8
a76	0.0804	82	0.00256	27	1.46724	1.88654	8	0.280913	38	0.280760	-0.5	1.4	3.47	3112	8
a78	0.0345	27	0.00121	9	1.46715	1.88671	7	0.280812	34	0.280739	-1.3	1.2	3.51	3112	8
a79	0.0312	22	0.00101	6	1.46724	1.88665	7	0.280826	31	0.280766	-0.3	1.1	3.46	3112	8
a80	0.0372	43	0.00117	11	1.46719	1.88681	7	0.280780	33	0.280710	-2.3	1.2	3.57	3112	8
a84	0.0431	87	0.00132	25	1.46712	1.88680	8	0.280801	40	0.280722	-1.9	1.4	3.54	3112	8
a85	0.0293	9	0.00100	3	1.46714	1.88665	8	0.280806	36	0.280746	-1.0	1.3	3.50	3112	8
a86	0.0854	114	0.00250	33	1.46715	1.88683	7	0.280879	43	0.280730	-1.6	1.5	3.53	3112	8
a87	0.0173	10	0.00059	3	1.46719	1.88666	7	0.280803	30	0.280768	-0.3	1.1	3.45	3112	8
a88	0.0277	11	0.00096	5	1.46715	1.88660	7	0.280773	37	0.280716	-2.1	1.3	3.56	3112	8
a89	0.0215	4	0.00080	2	1.46713	1.88665	6	0.280807	36	0.280759	-0.6	1.3	3.47	3112	8
a90	0.0756	81	0.00231	23	1.46715	1.88683	10	0.280884	38	0.280745	-1.1	1.4	3.50	3112	8
a91	0.0194	10	0.00068	3	1.46723	1.88672	8	0.280776	33	0.280735	-1.4	1.2	3.52	3112	8
HE-11-4A															
a92	0.0209	9	0.00064	3	1.46720	1.88674	9	0.280749	35	0.280711	-2.4	1.2	3.57	3109	14
a93	0.0176	12	0.00056	4	1.46714	1.88681	8	0.280760	46	0.280727	-1.8	1.6	3.54	3109	14
a94	0.0226	12	0.00069	3	1.46718	1.88681	10	0.280776	43	0.280734	-1.5	1.5	3.52	3109	14
a95	0.0196	15	0.00058	4	1.46717	1.88684	9	0.280759	41	0.280724	-1.9	1.5	3.54	3109	14
a97	0.0114	14	0.00036	5	1.46724	1.88675	7	0.280774	41	0.280753	-0.9	1.4	3.48	3109	14
a99	0.0234	25	0.00072	8	1.46714	1.88693	8	0.280748	31	0.280705	-2.6	1.1	3.58	3109	14
a100	0.0257	4	0.00088	1	1.46717	1.88677	7	0.280780	32	0.280725	0.3	1.1	3.49	3200	14
a101	0.0142	12	0.00045	3	1.46716	1.88679	7	0.280747	36	0.280720	-2.0	1.3	3.55	3109	14
a107	0.0184	21	0.00068	7	1.46716	1.88686	11	0.280691	28	0.280650	-4.5	1.0	3.69	3109	14
a108	0.0135	5	0.00049	2	1.46715	1.88680	7	0.280768	37	0.280738	0.8	1.3	3.46	3200	14
a109	0.0124	10	0.00040	3	1.46718	1.88658	7	0.280793	39	0.280769	1.9	1.4	3.41	3200	14
a110	0.0364	31	0.00115	10	1.46717	1.88675	11	0.280784	35	0.280716	-2.2	1.2	3.56	3109	14
a111	0.0155	8	0.00051	2	1.46717	1.88667	7	0.280745	37	0.280715	-2.2	1.3	3.56	3109	14
a113	0.0133	9	0.00045	3	1.46713	1.88677	6	0.280747	35	0.280719	0.1	1.3	3.50	3200	14
a114	0.0174	12	0.00057	4	1.46717	1.88674	7	0.280794	36	0.280758	1.5	1.3	3.43	3200	14
HE-11-8															
a117	0.1144	158	0.00382	54	1.46718	1.88680	6	0.280951	47	0.280724	-2.0	1.7	3.54	3105	9
a118	0.0378	29	0.00135	11	1.46709	1.88663	5	0.280847	41	0.280766	-0.5	1.5	3.46	3105	9
a120	0.0439	59	0.00160	21	1.46711	1.88674	7	0.280813	47	0.280718	-2.2	1.7	3.56	3105	9
a123	0.0657	36	0.00220	8	1.46719	1.88682	5	0.280862	33	0.280731	-1.7	1.2	3.53	3105	9
a125	0.0350	18	0.00123	7	1.46718	1.88689	5	0.280834	38	0.280761	-0.7	1.4	3.47	3105	9
a126	0.0391	7	0.00140	3	1.46718	1.88674	5	0.280826	35	0.280742	-1.3	1.2	3.51	3105	9
a127	0.0332	31	0.00114	10	1.46715	1.88680	6	0.280803	32	0.280734	-1.6	1.2	3.52	3105	1
a207	0.0653	48	0.00228	15	1.46719	1.88687	7	0.280905	39	0.280769	-0.4	1.4	3.46	3105	9
a208	0.0623	37	0.00209	13	1.46720	1.88659	8	0.280888	29	0.280763	-0.6	1.0	3.47	3105	9
a209	0.0365	12	0.00112	3	1.46718	1.88657	9	0.280829	32	0.280762	-0.6	1.1	3.47	3105	9
a210	0.0676	54	0.00221	13	1.46714	1.88663	8	0.280894	39	0.280762	-0.6	1.4	3.47	3105	9
a211	0.0554	11	0.00187	2	1.46715	1.88662	8	0.280865	33	0.280754	-0.9	1.2	3.48	3105	9
a212	0.0543	8	0.00185	5	1.46726	1.88667	8	0.280870	33	0.280760	-0.7	1.2	3.47	3105	9
a213	0.0300	37	0.00095	11	1.46718	1.88654	13	0.280822	30	0.280765	-0.5	1.1	3.46	3105	9
a215	0.0350	13	0.00120	6	1.46716	1.88669	8	0.280804	33	0.280732	-1.7	1.2	3.53	3105	9
a216	0.0550	42	0.00179	12	1.46711	1.88671	12	0.280834	34	0.280727	-1.9	1.2	3.54	3105	9
a217	0.0222	9	0.00074	4	1.46720	1.88666	8	0.280793	29	0.280749	-1.1	1.0	3.49	3105	9
a218	0.0426	27	0.00131	6	1.46713	1.88657	10	0.280832	43	0.280754	-0.9	1.5	3.48	3105	9
a219	0.0482	32	0.00155	10	1.46716	1.88664	11	0.280843	46	0.280750	-1.1	1.6	3.49	3105	9
MP-11-3															
a129	0.0102	7	0.00032	2	1.46716	1.88679	6	0.280724	30	0.280705	-2.7	1.1	3.58	3105	9
a130	0.0173	31	0.00061	10	1.46721	1.88678	8	0.280746	49	0.280710	-2.5	1.7	3.57	3105	9
a131	0.0191	35	0.00069	12	1.46714	1.88659	8	0.280721	33	0.280680	-3.5	1.2	3.63	3105	9
a132	0.0199	33	0.00068	11	1.46718	1.88668	9	0.280774	42	0.280733	-1.6	1.5	3.52	3105	9
a135	0.0169	14	0.00058	5	1.46713	1.88693	10	0.280748	49	0.280714	-2.3	1.7	3.56	3105	9
a143	0.0157	27	0.00055	9	1.46712	1.88671	7	0.280763	38	0.280730	-1.8	1.4	3.53	3105	9
a144	0.0231	21	0.00080	7	1.46714	1.88673	6	0.280780	35	0.280732	-1.7	1.3	3.53	3105	9
a145	0.0462	28	0.00152	9	1.46713	1.88676	5	0.280816	38	0.280725	-2.0	1.3	3.54	3105	9
HE-11-7															
a152	0.0326	18	0.00116	7	1.46720	1.88680	6	0.280799	37	0.280730	-1.8	1.3	3.53	3103	7
a153	0.0274	57	0.00096	19	1.46724	1.88671	6	0.280805	31	0.280747	-1.2	1.1	3.50	3103	7
a154	0.0451	20	0.00156	6	1.46710	1.88674	5	0.280828	32	0.280734	-1.7	1.1	3.52	3103	7
a155	0.0286	19	0.00104	7	1.46718	1.88661	5	0.280818	37	0.280756	-0.9	1.3	3.48	3103	7
a156	0.0374	21	0.00132	7	1.46719	1.88677	5	0.280791	36	0.280712	-2.4	1.3	3.57	3103	7
a159	0.0454	124	0.00159	39	1.46714	1.88681	6	0.280802	40	0.280707	-2.6	1.4	3.58	3103	7
a160	0.0379	22	0.00143	7	1.46718	1.88680	5	0.280837	39	0.280752	-1.0	1.4	3.49	3103	7
a161	0.0508	13	0.00177	5	1.46722	1.88677	6	0.280869	32	0.280763	-0.6	1.1	3.47	3103	7
a162	0.0319	13	0.00117	5	1.46715	1.88671	5	0.280803	37	0.280733	-1.7	1.3	3.53	3103	7
a163	0.0522	51	0.00180	16	1.46711	1.88671	5	0.280839	44	0.280732	-1.7	1.6	3.53	3103	7
a164	0.0314	8	0.00109	3	1.46715	1.88679	5	0.280808	34	0.280743	-1.3	1.2	3.51	3103	7
a166	0.0288	2	0.00113	1	1.46724	1.88679	5	0.280815	34	0.280747	-1.2	1.2	3.50	3103	7
a172	0.0370	20	0.00134	5	1.46717	1.88677	6	0.280797	33	0.280717	-2.3	1.2	3.56	3103	7
a168	0.0489	32	0.00169	11	1.46718	1.88661	5	0.280841	37	0.280741	-1.4	1.3	3.51	3103	7
a169	0.0274	4	0.00095	2	1.46717	1.88668	6	0.280773	39	0.280716	-2.3	1.4	3.56	3103	7
a170	0.0256	7	0.00100	2	1.46719	1.88672	5	0.280823	32	0.280763	-0.6	1.2	3.47	3103	7
a171	0.0525	141	0.00181	46	1.46713	1.88688	5	0.280862	45	0.280754	-1.0	1.6	3.49	3103	7
HE-11-15B															
a173	0.0215	22	0.00078	7	1.46716	1.88680	7	0.280770	33	0.280722	0.2	1.2	3.50	3201	9
a174	0.0371	15	0.00103	6	1.46711	1.88669	16	0.280788	30	0.280725	0.3	1.1	3.49	3201	9
a175	0.0131	30	0.00039	8	1.46718	1.88672	11	0.280748	34	0.280724	0.3	1.2	3.49	3201	9
a176	0.0236	4	0.00078	1	1.46723	1.88671	7	0.280776	34	0.280728	0.4	1.2	3.48	3201	9
a177	0.0290	21	0.00096	8	1.46719	1.88663	8	0.280771	34	0.280712	-0.1	1.2	3.52	3201	9
a180	0.0218	5	0.00069	2	1.46717	1.88666	9	0.280774	29	0.280731	0.5	1.0	3.48	3201	9
a220	0.0301	14	0.00102	5	1.46716	1.88652	8	0.280792	33	0.280729	0.5	1.2	3.48	3201	9
a221	0.0312	9	0.00107	3	1.46718	1.88671	8	0.280806	37	0.280740	0.9	1.3	3.46	3201	9
a222	0.0214	1	0.00068	2	1.46716	1.88661	9	0.280767	31	0.280725	0.3	1.1	3.49	3201	9
a224	0.0071	3	0.00026	0	1.46721	1.88665	10	0.280757	33	0.280741	0.9	1.2	3.46	3201	9
a226	0.0064	1	0.00025	0	1.46721	1.88664	10	0.280759	34	0.280743	1.0	1.2	3.46	3201	9
a227	0.0056	4	0.00020	1	1.46722	1.88659	10	0.280752	31	0.280740	0.9	1.1	3.46	3201	9
a228	0.0244	9	0.00086	3	1.46720	1.88654	11	0.280779	34	0.280726	0.4	1.2	3.49	3201	9
MP-11-2															
a181	0.0160	9	0.00057	3	1.46718	1.88672	6	0.280775	37	0.280741	-1.4	1.3	3.51	3104	7
a182	0.0128	14	0.00047	4	1.46718	1.88667	6	0.280754	30	0.280726	-1.9	1.1	3.54	3104	7
a183	0.0213	9	0.00070	3	1.46719	1.88649	9	0.280785	31	0.280743	-1.3	1.1	3.51	3104	7
a184	0.0107	2	0.00037	0	1.46722	1.88667	9	0.280751	30	0.280728	-1.9	1.1	3.54	3104	7
a185	0.0138	4	0.00046	1	1.46716	1.88661	9	0.280757	31	0.280730	-1.8	1.1	3.53	3104	7
a186	0.0119	1	0.00040	1	1.46719	1.88661	10	0.280769	30	0.280746	-1.2	1.1	3.50	3104	7
a187	0.0128	2	0.00044	1	1.46720	1.88662	9	0.280774	29	0.280748	-1.1	1.0	3.50	3104	7
a188	0.0164	7	0.00056	2	1.46714	1.88678	11	0.280765	31	0.280732	-1.7	1.1	3.53	3104	7
a190	0.0130	5	0.00046	2	1.46719	1.88670	10	0.280764	32	0.280736	-1.6	1.1	3.52	3104	7
a191	0.0121	2	0.00043	1	1.46720	1.88671	9	0.280747	32	0.280722	-2.1	1.1	3.55	3104	7
a192	0.0116	4	0.00041	1	1.46717	1.88669	9	0.280773	29	0.280748	-1.1	1.0	3.50	3104	7
a193	0.0191	8	0.00065	2	1.46722	1.88652	9	0.280779	31	0.280740	-1.4	1.1	3.51	3104	7
a200	0.0116	11	0.00040	3	1.46720	1.88656	10	0.280759	32	0.280736	-1.6	1.1	3.52	3104	7
a201	0.0134	6	0.00044	2	1.46716	1.88654	9	0.280769	31	0.280743	-1.3	1.1	3.51	3104	7
a203	0.0126	4	0.00043	2	1.46720	1.88674	10	0.280761	32	0.280735	-1.6	1.2	3.52	3104	7
a204	0.0151	9	0.00050	3	1.46717	1.88656	7	0.280771	38	0.280741	-1.4	1.3	3.51	3104	7
a205	0.0128	2	0.00044	0	1.46720	1.88663	8	0.280779	32	0.280753	-1.0	1.2	3.49	3104	7
MP11-7															
a229	0.0149	5	0.00058	1	1.46717	1.88662	14	0.280795	36	0.280761	-0.7	1.3	3.47	3106	8
a230	0.0250	19	0.00085	4	1.46726	1.88654	11	0.280818	30	0.280768	-0.4	1.1	3.46	3106	8
a231	0.0336	19	0.00105	6	1.46724	1.88671	11	0.280817	32	0.280754	-0.9	1.1	3.48	3106	8
a232	0.0448	39	0.00137	11	1.46722	1.88662	12	0.280822	33	0.280740	-1.4	1.2	3.51	3106	8
a233	0.0376	14	0.00129	3	1.46720	1.88662	12	0.280819	31	0.280742	-1.3	1.1	3.51	3106	8
a234	0.0399	4	0.00141	1	1.46719	1.88646	12	0.280846	30	0.280762	-0.6	1.1	3.47	3106	8
a254	0.0307	29	0.00109	10	1.46720	1.88694	5	0.280796	35	0.280731	-1.7	1.3	3.53	3106	8
a255	0.0567	79	0.00168	19	1.46727	1.88674	6	0.280861	38	0.280761	-0.7	1.4	3.47	3106	8
a257	0.0255	10	0.00087	3	1.46717	1.88669	6	0.280801	34	0.280749	-1.1	1.2	3.49	3106	8
a258	0.0339	18	0.00109	6	1.46718	1.88665	6	0.280832	42	0.280768	-0.4	1.5	3.46	3106	8
a260	0.0383	36	0.00125	9	1.46716	1.88644	6	0.280829	38	0.280754	-0.9	1.4	3.48	3106	8
a262	0.0326	32	0.00106	10	1.46715	1.88672	6	0.280817	36	0.280754	-0.9	1.3	3.48	3106	8
a263	0.0408	30	0.00132	7	1.46724	1.88659	6	0.280842	37	0.280763	-0.6	1.3	3.47	3106	8
a265	0.0434	32	0.00138	10	1.46726	1.88691	6	0.280851	36	0.280768	-0.4	1.3	3.46	3106	8
a268	0.0200	41	0.00059	9	1.46719	1.88676	8	0.280792	35	0.280756	-0.9	1.3	3.48	3103	1
a270	0.0137	15	0.00050	5	1.46724	1.88676	9	0.280764	33	0.280735	-1.6	1.2	3.52	3105	1
MP-12-01															
a235	0.0151	23	0.00056	12	1.46723	1.88653	10	0.280791	34	0.280757	-0.9	1.2	3.48	3103	9
a236	0.0166	4	0.00056	1	1.46722	1.88667	11	0.280802	30	0.280768	-0.4	1.1	3.46	3103	9
a237	0.0166	4	0.00056	2	1.46722	1.88662	10	0.280786	30	0.280753	-1.0	1.1	3.49	3103	9
a243	0.0169	7	0.00054	1	1.46721	1.88659	10	0.280798	31	0.280765	-0.6	1.1	3.46	3103	9
a244	0.0229	18	0.00077	6	1.46723	1.88671	11	0.280794	29	0.280748	-1.2	1.0	3.50	3103	9
a245	0.0198	10	0.00063	3	1.46717	1.88663	12	0.280780	30	0.280743	-1.4	1.1	3.51	3103	9
a246	0.0576	18	0.00208	16	1.46722	1.88667	13	0.280888	35	0.280764	-0.6	1.3	3.47	3103	9
a247	0.0193	11	0.00070	6	1.46720	1.88646	8	0.280792	32	0.280751	-1.1	1.1	3.49	3103	9
a248	0.0152	6	0.00050	1	1.46726	1.88668	10	0.280784	32	0.280754	-1.0	1.1	3.49	3103	9
a249	0.0196	9	0.00068	4	1.46722	1.88661	11	0.280792	30	0.280752	-1.0	1.1	3.49	3103	9
a250	0.0111	2	0.00038	1	1.46719	1.88667	10	0.280762	29	0.280739	-1.5	1.0	3.51	3103	9
a252	0.0122	3	0.00043	1	1.46719	1.88654	10	0.280786	30	0.280760	-0.7	1.1	3.47	3103	9
a253	0.0134	3	0.00045	0	1.46722	1.88655	10	0.280795	31	0.280768	-0.5	1.1	3.46	3103	9
HE-11-12															
a273	0.0577	18	0.00172	5	1.46717	1.88664	9	0.280824	32	0.280721	-2.0	1.1	3.55	3107	27
a274	0.0365	23	0.00123	9	1.46723	1.88674	9	0.280795	86	0.280721	-2.0	3.1	3.55	3107	27
a280	0.0255	31	0.00085	7	1.46720	1.88641	7	0.280771	38	0.280719	0.1	1.4	3.50	3200	27
a281	0.0461	29	0.00133	7	1.46720	1.88673	10	0.280801	34	0.280722	-2.0	1.2	3.55	3107	27
a282	0.0510	30	0.00170	8	1.46720	1.88681	7	0.280805	40	0.280704	-2.7	1.4	3.58	3107	27
a289	0.0496	27	0.00138	7	1.46718	1.88669	13	0.280808	38	0.280725	-1.9	1.4	3.54	3107	27
a290	0.0448	19	0.00131	5	1.46718	1.88674	16	0.280819	33	0.280741	-1.3	1.2	3.51	3107	27
a291	0.0376	22	0.00104	6	1.46712	1.88677	10	0.280774	37	0.280712	-2.4	1.3	3.57	3107	27
a292	0.0346	20	0.00108	6	1.46722	1.88670	7	0.280795	45	0.280731	-1.7	1.6	3.53	3107	27
a294	0.0220	15	0.00080	5	1.46713	1.88667	9	0.280756	31	0.280708	-2.5	1.1	3.57	3107	27
a295	0.0226	16	0.00068	6	1.46714	1.88674	10	0.280742	31	0.280700	-0.6	1.1	3.54	3200	27
HE-11-6															
a296	0.0084	11	0.00039	4	1.46720	1.88666	8	0.280778	32	0.280755	-1.3	1.1	3.49	3086	19
a297	0.0669	44	0.00214	13	1.46721	1.88655	7	0.280895	37	0.280768	-0.9	1.3	3.47	3086	19
a298	0.0756	57	0.00245	19	1.46708	1.88660	5	0.280910	38	0.280764	-1.0	1.4	3.47	3086	19
a299	0.0156	21	0.00058	5	1.46718	1.88640	9	0.280794	38	0.280760	-1.2	1.3	3.48	3086	19
a301	0.0186	20	0.00062	4	1.46729	1.88666	9	0.280791	42	0.280754	-1.4	1.5	3.49	3086	19
a302	0.0269	57	0.00091	17	1.46717	1.88685	9	0.280793	37	0.280739	-1.9	1.3	3.52	3086	19
a304	0.0252	21	0.00092	6	1.46717	1.88672	8	0.280809	42	0.280755	-1.3	1.5	3.49	3086	19
a305	0.0217	18	0.00076	6	1.46718	1.88669	7	0.280782	41	0.280736	-2.0	1.5	3.53	3086	19
a306	0.0522	13	0.00172	6	1.46714	1.88693	5	0.280845	52	0.280743	-1.8	1.9	3.52	3086	19
a307	0.0322	25	0.00103	7	1.46713	1.88683	7	0.280807	37	0.280746	-1.6	1.3	3.51	3086	19
a316	0.0280	38	0.00105	11	1.46708	1.88675	7	0.280788	38	0.280726	-2.4	1.4	3.55	3086	19
HE-11-10															
a317	0.0446	8	0.00133	2	1.46721	1.88667	8	0.280827	33	0.280748	-0.6	1.2	3.49	3126	37
a318	0.0446	100	0.00150	35	1.46718	1.88681	8	0.280818	39	0.280728	-1.3	1.4	3.52	3126	37
HE-11-27A															
a319	0.0143	3	0.00049	1	1.46724	1.88676	5	0.280777	36	0.280748	-1.2	1.3	3.50	3103	11
a320	0.0170	8	0.00055	3	1.46722	1.88668	6	0.280768	38	0.280735	-1.6	1.4	3.52	3103	11
a321	0.0158	3	0.00051	1	1.46716	1.88673	5	0.280768	38	0.280738	-1.5	1.4	3.52	3103	11
a322	0.0183	14	0.00059	3	1.46716	1.88658	5	0.280783	37	0.280747	-1.2	1.3	3.50	3103	11
HE-11-31A															
a326	0.0271	11	0.00097	4	1.46715	1.88676	5	0.280801	37	0.280744	-1.5	1.3	3.51	3096	19
a327	0.0148	3	0.00053	1	1.46711	1.88659	6	0.280773	35	0.280741	-1.6	1.2	3.51	3096	19
a333	0.0130	2	0.00045	0	1.46722	1.88686	5	0.280752	33	0.280726	-2.1	1.2	3.54	3096	19
a334	0.0309	13	0.00104	4	1.46718	1.88677	9	0.280777	32	0.280715	-2.5	1.1	3.56	3096	19
HE-11-28A															
a336	0.0450	19	0.00157	7	1.46718	1.88677	7	0.280804	41	0.280710	-2.4	1.5	3.57	3108	28
a337	0.1481	45	0.00439	12	1.46703	1.88701	7	0.280976	51	0.280714	-2.3	1.8	3.56	3108	28
a338	0.0582	50	0.00198	17	1.46715	1.88680	6	0.280838	52	0.280719	-2.1	1.9	3.55	3108	28
a341	0.0467	59	0.00151	13	1.46713	1.88686	7	0.280805	34	0.280715	-2.2	1.2	3.56	3108	28
a345	0.0988	146	0.00318	45	1.46721	1.88677	9	0.280931	50	0.280741	-1.3	1.8	3.51	3108	28
a346	0.1112	55	0.00326	18	1.46717	1.88654	8	0.280937	42	0.280742	-1.3	1.5	3.51	3108	28

(a) $^{176}Yb/^{177}Hf = (^{176}Yb/^{173}Yb)_{true} \times (^{173}Yb/^{177}Hf)_{meas} \times (M_{173(Yb)}/M_{177(Hf)})^{\beta(Hf)}$, $\beta(Hf) = \ln(^{179}Hf/^{177}Hf_{true} / ^{179}Hf/^{177}Hf_{measured}) / \ln(M_{179(Hf)}/M_{177(Hf)})$,

M=mass of respective isotope. The $^{176}Lu/^{177}Hf$ were calculated in a similar way by using the $^{175}Lu/^{177}Hf$ and β(Yb).

Quoted uncertainties (absolute) relate to the last quoted figure. The effect of the inter-element fractionation on the Lu/Hf was estimated to be about 6 % or less based on analyses of the GJ-1 and Plesovice zircons.

(b) Mean Hf signal in volt.

(c) Uncertainties are quadratic additions of the within-run precision and the daily reproducibility of the zircon GJ-1. Uncertainties for GJ-1 is 2SD (2 standard deviation).

(d) Initial $^{176}Hf/^{177}Hf$ and εHf calculated using an age of 2055 Ma, and the CHUR parameters: $^{176}Lu/^{177}Hf$ = 0.0336, and $^{176}Hf/^{177}Hf$ = 0.282785 (Bouvier et al., 2008).

(e) two stage model age in billion years using the measured $^{176}Hf/^{177}Hf$, and $^{176}Lu/^{177}Hf$ and the intrusion age, and a $^{176}Lu/^{177}Hf$= 0.0113 for the average continental crust (second stage), and a depleted mantle $^{176}Lu/^{177}Hf$ and $^{176}Hf/^{177}Hf$ of 0.03933 and 0.283294, see Blichert-Toft & Puchtel (2010).

standard zircon GJ1															
GJ1-40-1	0.0083	0.3	0.00028	0.0	1.46725	1.88650	13	0.282017	28	0.282013	-13.8	1.0	2.23	606	1
GJ1-40-2	0.0081	0.4	0.00027	0.1	1.46724	1.88649	12	0.282005	30	0.282002	-14.2	1.1	2.25	606	1
GJ1-40-3	0.0078	0.7	0.00028	0.1	1.46721	1.88662	10	0.281989	32	0.281986	-14.8	1.1	2.28	606	1
GJ1-40-4	0.0073	1.2	0.00026	0.1	1.46720	1.88671	10	0.282002	31	0.281999	-14.3	1.1	2.26	606	1
GJ1-40-5	0.0074	0.9	0.00026	0.1	1.46722	1.88677	10	0.281999	31	0.281996	-14.4	1.1	2.26	606	1
GJ1-40-6	0.0077	1.0	0.00027	0.1	1.46720	1.88667	11	0.281994	31	0.281991	-14.6	1.1	2.27	606	1
GJ1-40-7	0.0070	0.6	0.00027	0.1	1.46719	1.88671	8	0.282006	32	0.282003	-14.2	1.1	2.25	606	1
GJ1-40-8	0.0074	0.8	0.00027	0.1	1.46721	1.88667	9	0.281999	32	0.281996	-14.4	1.1	2.26	606	1
GJ1-40-9	0.0075	1.0	0.00027	0.1	1.46713	1.88668	9	0.281985	31	0.281982	-14.9	1.1	2.29	606	1
GJ1-40-10	0.0067	0.5	0.00025	0.1	1.46723	1.88655	8	0.282027	32	0.282024	-13.4	1.1	2.21	606	1
GJ1-40-11	0.0070	0.5	0.00025	0.1	1.46718	1.88665	9	0.282008	30	0.282005	-14.1	1.1	2.24	606	1
mean (n=9)	**0.0075**		**0.00027**		**1.46720**	**1.88664**		**0.282003**			**-14.3**				
2σS.D.	**0.0010**		**0.00002**		**0.00007**	**0.00018**		**0.000024**			**0.8**				
standard zircon Plesoviče															
Pleso-1	0.0051	1.0	0.00013	0.1	1.46718	1.88642	14	0.282460	29	0.282459	-4.0	1.0	1.48	337	1
Pleso-2	0.0029	1.2	0.00007	0.2	1.46722	1.88658	16	0.282461	30	0.282460	-4.0	1.1	1.48	337	1
Pleso-3	0.0053	0.6	0.00013	0.1	1.46725	1.88660	15	0.282460	32	0.282459	-4.0	1.1	1.48	337	1
Pleso-4	0.0059	0.9	0.00014	0.0	1.46727	1.88662	15	0.282478	30	0.282477	-3.4	1.1	1.45	337	1
Pleso-6	0.0037	0.5	0.00009	0.0	1.46722	1.88668	13	0.282468	32	0.282467	-3.7	1.1	1.47	337	1
Pleso-7	0.0049	0.7	0.00012	0.0	1.46723	1.88658	14	0.282478	27	0.282477	-3.4	1.0	1.45	337	1
Pleso-8	0.0050	0.4	0.00012	0.0	1.46720	1.88662	14	0.282454	29	0.282453	-4.2	1.0	1.50	337	1
mean (n=7)	**0.0047**		**0.00011**		**1.46722**	**1.88659**		**0.282465**			**-3.8**				
2σS.D.	**0.0020**		**0.00005**		**0.00006**	**0.00016**		**0.000019**			**0.7**				
standard zircon 91500															
91500-1	0.0083	1.8	0.00031	0.7	1.46728	1.88655	8	0.282274	30	0.282268	5.6	1.1	1.53	1065	1
91500-2	0.0085	1.3	0.00032	0.4	1.46718	1.88659	8	0.282282	32	0.282275	5.9	1.1	1.52	1065	1
91500-3	0.0090	1.1	0.00033	0.2	1.46721	1.88673	8	0.282282	29	0.282275	5.9	1.0	1.52	1065	1
91500-4	0.0088	1.6	0.00032	0.3	1.46722	1.88663	8	0.282284	27	0.282278	5.9	1.0	1.51	1065	1
91500-5	0.0090	1.2	0.00034	0.6	1.46723	1.88662	6	0.282295	33	0.282289	6.3	1.2	1.49	1065	1
91500-6	0.0094	0.9	0.00034	0.4	1.46730	1.88663	6	0.282295	34	0.282288	6.3	1.2	1.49	1065	1
91500-7	0.0098	1.2	0.00034	0.5	1.46727	1.88650	7	0.282293	30	0.282287	6.3	1.1	1.49	1065	1
91500-8	0.0100	0.4	0.00037	0.5	1.46722	1.88660	7	0.282312	32	0.282305	6.9	1.1	1.46	1065	1
91500-9	0.0104	0.4	0.00037	0.4	1.46717	1.88663	7	0.282293	37	0.282285	6.2	1.3	1.50	1065	1
mean (n=9)	**0.0092**		**0.00034**		**1.46723**	**1.88661**		**0.282290**			**6.1**				
2σS.D.	**0.0014**		**0.00004**		**0.00009**	**0.00013**		**0.000022**			**0.8**				

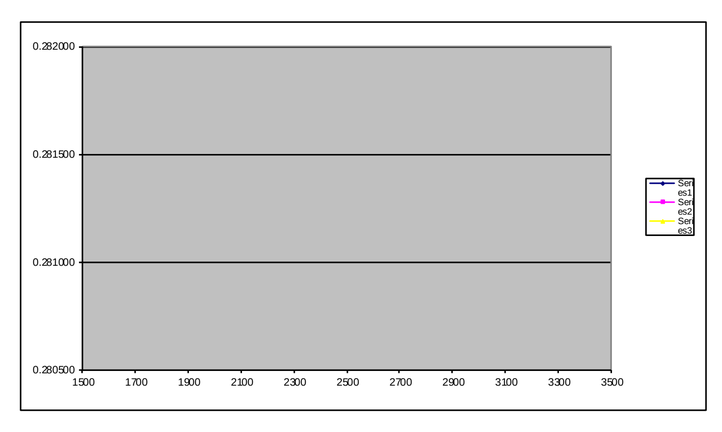

Table X: Summary of Lu-Hf isotope analyses

sample	Facies	$^{176}Hf/^{177}Hf_t$	±2σ (mean)	εHf_t	±2σ (mean)	T_{DM} (Ga)	±2σ (mean)	n	age (Ma)	comment
Heerenveen										
HE-11-28A	*Leucogranite 1*	0.28072	0.00003	-1.9	1.0	3.54	0.03	6	3108	
HE-12-1	*Leucogranite 2*	0.28071	0.00003	-2.1	1.1	3.56	0.03	13	3114	
HE-11-27A	*Leucogranite 2*	0.28074	0.00001	-1.4	0.5	3.51	0.01	4	3103	
HE-11-16b	*Leucogranite 2*	0.28074	0.00004	-1.3	1.4	3.51	0.04	16	3112	
HE-11-15B	*Megacryst granite*	0.28073	0.00002	0.5	0.6	3.48	0.02	13	3201	
HE-11-35	*Megacryst granite*	0.28073	0.00004	-1.8	1.3	3.54	0.04	10	3111	1 ol, (i.n.c.)
HE-11-12	*Megacryst granite*	0.28072	0.00002	-2.1	0.8	3.55	0.02	9	3107	(i.n.c.)
HE-11-10	*Megacryst granite*	0.28074	0.00003	-1.0	1.0	3.50	0.03	2	3126	
HE-11-8	*Quartz monzonite*	0.28075	0.00003	-1.1	1.2	3.50	0.03	19	3105	
HE-11-7	*Quartz monzonite*	0.28074	0.00003	-1.5	1.2	3.52	0.03	17	3103	
HE-11-6	*Quartz monzonite*	0.28075	0.00003	-1.5	0.9	3.50	0.03	11	3086	
HE-11-3	*Pink granite 1*	0.28071	0.00005	-2.5	1.7	3.57	0.05	7	3109	
HE-11-4A	*Pink granite 1*	0.28072	0.00003	-1.9	1.0	3.54	0.03	9	3109	1 ol, (i.n.c.)
HE-11-31A	*Pink granite 2*	0.28073	0.00003	-1.9	1.0	3.53	0.03	4	3096	
Mpuluzi										
MP-12-01	*Pegmatite*	0.28076	0.00002	-0.9	0.7	3.48	0.02	17	3103	
MP-11-7	*Leucogranite 1*	0.28075	0.00002	-0.9	0.8	3.48	0.02	16	3106	
MP-11-3	*Pink granite 1*	0.28072	0.00004	-2.3	1.3	3.56	0.04	8	3105	
MP-11-2	*Syenogranite*	0.28074	0.00002	-1.5	0.6	3.52	0.02	17	3104	
Theespruit volcanics										
.12-1	*Felsic agglomerate*	0.28046	0.00006	-1.4	2.2	3.83	0.12	7	3521	
.12-2	*Felsic agglomerate*	0.28048	0.00007	-0.6	2.4	3.80	0.13	20	3527	
.12-3	*Felsic agglomerate*	0.28047	0.00004	-1.2	1.3	3.83	0.07	3	3527	
.12-6	*Felsic agglomerate*	0.28047	0.00005	-1.0	1.9	3.82	0.10	35	3531	

ol - outlier, (i.n.c.) - inherited grains not considered

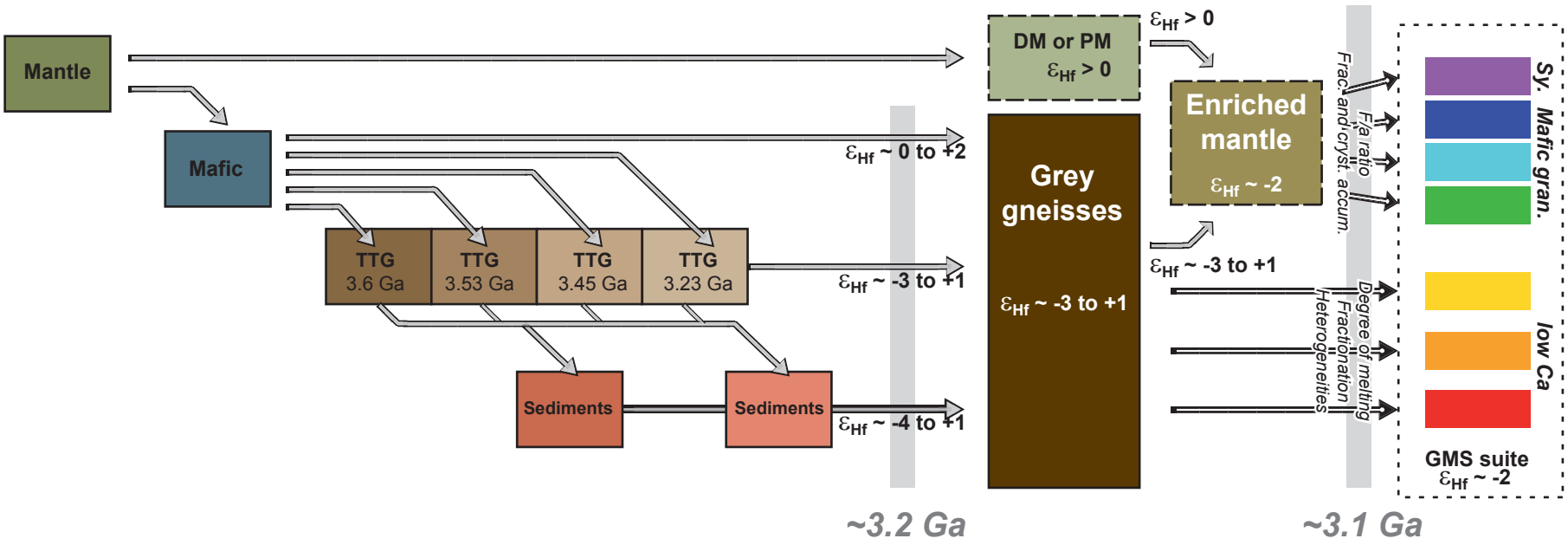
Mantle
Mafic
TTG
3.6 Ga
TTG
3.53 Ga
TTG
3.45 Ga
TTG
3.23 Ga
Sediments
Sediments
εHf ~ 0 to +2
εHf ~ -3 to +1
εHf ~ -4 to +1
~3.2 Ga
DM or PM
εHf > 0
Grey
gneisses
εHf ~ -3 to +1
εHf > 0
Enriched
mantle
εHf ~ -2
εHf ~ -3 to +1
Frac. and cryst. accum.
F/a ratio
Degree of melting
Fractionation
Heterogeneities
Sy. Mafic gran.
low Ca
GMS suite
εHf ~ -2
~3.1 Ga